Pontifícia Universidade Católica
do Rio de Janeiro

Yan Dalton Rodrigues Machado

Optical characterization and optimization of nano and 2D materials

Dissertação de Mestrado

Dissertation presented to the Programa de Pós-Graduação em Física of PUC-Rio in partial fulfillment of the requirements for the degree of Mestre em Ciências – Física.

Advisor: Prof. Isabel Cristina dos Santos Carvalho

Rio de Janeiro,
January 2025

PONTIFÍCIA UNIVERSIDADE CATÓLICA
DO RIO DE JANEIRO

Yan Dalton Rodrigues Machado

Optical characterization and optimization of nano and 2D materials

Dissertation presented to the Programa de Pós–Graduação em Física of PUC-Rio in partial fulfillment of the requirements for the degree of Mestre em Ciências – Física. Approved by the Examination Committee.

Profª Isabel Cristina dos Santos Carvalho
Advisor
Departamento de Física - PUC-Rio

Prof. André de Lima Moura
UFAL

Prof. Mauricio Almeida Caiut
USP

Rio de Janeiro, January 24th, 2025

Yan Dalton Rodrigues Machado

The author graduated in Physics from PUC-Rio in 2022 and has been conducting research in optics since 2018.

Bibliographic Data

Machado, Yan Dalton Rodrigues

Optical characterization and optimization of nano and 2D materials / Yan Dalton Rodrigues Machado; advisor: Isabel Cristina dos Santos Carvalho. – Rio de Janeiro: PUC-Rio, Departamento de Física, 2025.

v., 96 f. : il. color. ; 30 cm

Dissertação (mestrado) – Pontifícia Universidade Católica do Rio de Janeiro, Departamento de Física, 2023.

Inclui bibliografia

1. Física – Teses. 2. Física – Teses. 3. Caracterização óptica. 4. Optimização. 5. Lasers. 6. Espalhamento. 7. Nanomateriais. 8. Materiais 2D. 9. Aprendizado de máquinas. I. Cristina dos Santos Carvalho, Isabel. II. Pontifícia Universidade Católica do Rio de Janeiro. Departamento de Física.

Acknowledgments

First and foremost, I would like to express my deepest gratitude to my supervisor, prof. Isabel C. S. Carvalho, for giving me the opportunity to begin my research journey as an undergraduate almost seven years ago. From her, I learned the nuances of how to conduct research, how to build collaborations, study effectively, write my work in a way others would understand, and, most of all, how to support others around me. I also thank her for all the advice, conversations, lunches and help when I was confused and indecisive about my career path. The years we worked together and the memorable moments we shared will forever hold a special place in my heart. I could not have wished for a better mentor and friend, and I feel the luckiest student in the world looking back to how it all started.

I thank my mother, Cristina Rodrigues dos Santos Machado, for her unconditional love and support. Thank you for ensuring I never lacked anything, for your care in every moment of need, for guiding me toward the right decisions, and for standing by me with encouragement and understanding whenever I made mistakes. I thank my father, Dalton Ferreira Machado, for nurturing my curiosity from a young age with his wisdom and patience, inspiring my passion for physics and science. His example of honesty, dedication to learning, and hard work continues to guide and motivate me in every step of my journey. I feel very privileged to have you as my parents and for our family, and most of all to know that if something goes wrong, I can always head back home and take some time. I also thank my dinda Tânia, for all the support at all times, and my family.

I thank prof. Walter Margulis for all the great conversations, for patiently teaching me most of what I know about fiber optics, and for the countless hours we spent discussing and preparing experiments. For the thought-provoking questions (some that still keep me awake at night), his willingness to share his great ideas with me and for teaching me to do all sorts of things related to fibers and lasers. For all the work we have done and that is still to come.

I thank my girlfriend Fernanda Werneck Gonçalves, for all the love, support, and the countless ways she has helped me. I thank her for understanding all the time I devote to my work and for her support through every moment and decision. Thank you for standing by my side and for embracing moving to Sweden with me.

I also thank Dr. Gleice Germano, for all the good times in the lab and for

becoming a good friend and Dr. Leonardo F. Araujo, for teaching me so much when I started research and for being the best gamemaster there is. I am also grateful for working alongside Wanessa, Livio, João, Victor, Gabriela, Fredy, Mariana, Fred, Alexandre, Larissa, and everyone who brings joy to my daily routine.

I thank my friend Lucas Vivian for our company, for motivating me to work harder, and for all the projects we build and will build in the future.

I am grateful for my friends Nina Rosa, for always being by my side helping and supporting me, and Luís Gustavo, for all the conversations that led me to where I am today and for helping me make the best decisions.

I also thank all the great professors I had, both from the physics and mathematics department. Prof. Thiago Guerreiro, for all the courses, coffee breaks and for helping me think about what I actually wanted to do with my career; and prof. Carlos Tomei, for his analysis classes, which were the best classes I've had.

Dr. Edison Pecoraro, for our long-lasting collaboration and for all the help regarding chemistry and materials. I am also profoundly grateful to all the other collaborators who contributed to the development of my work over all those years, too numerous to name within a reasonable length of text.

I thank all the friends I made during my years at PUC, especially Bia Ereias for all the Vasco da Gama games we endured together; Igor Califrer, for all the courses we took and fun we had studying; Alice, for your friendship and companionship; and Marcos, for all the coffees and brigadeiros.

I would also like to thank my dearest friends Barros, Pita, Alonso, Toinho, Renan, Cota, Paulista, Mark and Serpa, for staying close to me during all these years and for all the time we spent playing games together. I extend my gratitude to all my friends from HoN for all the trips and time we spent having fun playing with Coxa. I also thank Franco, for your friendship, and all my friends from Mobilidade Urbana, for all the Speedtests and bike rides we took together.

Michael Fokine and Natalia Fijoł, thank you for the great times, both in Rio and in Stockholm, and for all the caipirinhas and great moments we shared.

Work reported in this document was funded by the Office of Naval Research Global (ONRG), Air Force Research Laboratory (AFRL), FAPERJ, CNPq, FACEPE, INCT-Photonics, OPTICA, and PUC-Rio. This study was financed in part by the Coordenação de Aperfeiçoaento de Pessoal de Nível Superior - Brasil (CAPES) - Finance Code 001.

Abstract

Machado, Yan Dalton Rodrigues, Isabel Cristina dos Santos Carvalho (Advisor) **Optical characterization and optimization of nano and 2D materials.** Rio de Janeiro, 2025. 96p. Physics Department, Pontifícia Universidade Católica do Rio de Janeiro

The optical characterization and optimization of nano- and two-dimensional (2D) materials are fundamental for advancing photonic devices and applications. This dissertation is divided into four different investigations on optics and presents an integrated approach combining experimental and computational methods to investigate and enhance the optical properties of these materials. First, light scattering phenomena was explored using random laser systems and numerical simulations to determine the scattering efficiency of different natural nanomaterials for various applications such as phototherapy devices. Second, hyper-Rayleigh scattering (HRS) technique was employed to characterize the second-harmonic generation, revealing nonlinear optical responses of nanocrystals. Additionally, the optical behavior of transition metal dichalcogenides (TMDs) under external excitations, such as varying electric fields, was systematically studied, providing a deeper understanding of their tunable properties and degradation mechanism. Finally, the optimization of nanomaterials was addressed through the application of a multi-objective genetic algorithm (MOGA), enabling the identification of geometrical configurations with enhanced optical properties for plasmonic applications.

Keywords

Optical characterization; optimization; lasers; scattering; nanomaterials; 2D materials; machine learning.

Resumo

Machado, Yan Dalton Rodrigues, Isabel Cristina dos Santos Carvalho (Orientadora) **Caracterização óptica e otimização de materiais bidimensionais e nanométricos.** Rio de Janeiro, 2025. 96p. Departamento de Física, Pontifícia Universidade Católica do Rio de Janeiro

A caracterização óptica e otimização de materiais nano e bidimensionais (2D) são fundamentais para o avanço de dispositivos e aplicações fotônicas. Esta dissertação está dividida em quatro diferentes linhas de pesquisa em óptica e apresenta uma abordagem integrada combinando métodos experimentais e computacionais para investigar e aprimorar as propriedades ópticas destes materiais. Primeiro, os fenômenos de espalhamento de luz foram explorados usando sistemas de laser aleatórios e simulações numéricas para determinar a eficiência de diferentes nanomateriais naturais. Em segundo lugar, técnicas de espalhamento hiper-Rayleigh foram empregadas para caracterizar a geração de segundo harmônico, revelando a resposta óptica não linear de nanocristais. Além disso, o comportamento óptico dos dichalcogenetos de metais de transição (TMDs) sob excitações externas, como campos elétricos variados, foi estudado sistematicamente, proporcionando uma compreensão mais profunda de suas propriedades e degradação. Por fim, a otimização de nanomateriais foi abordada através da aplicação de um algoritmo genético multiobjetivo (MOGA), possibilitando a identificação de geometrias com propriedades ópticas aprimoradas para nanomateriais metálicos.

Palavras chave

Caracterização óptica; optimização; lasers; espalhamento; nanomateriais; materiais 2D; aprendizado de máquinas.

Summary

List of figures

“So many things that I've created
But this right here might be my favorite”
Mac Miller

1
Introduction

The research hereby reported was conducted at the Optoelectronics Laboratory (LOpEL) at the Pontifical Catholic University of Rio de Janeiro (PUC-Rio). The dissertation encompasses a series of investigations spanning various domains of optics and nonlinear optics. Each chapter focuses on a specific experiment, beginning with theoretical foundations and progressing through methodology, results and different applications.

The unifying theme across all reported work is the interaction between light and materials. This interaction forms the backbone of many technological advancements, from telecommunications and phototherapy to energy harvesting and environmental sensing. The unique ability of optical materials to manipulate light—through absorption, reflection, refraction, and scattering—has allowed unprecedented possibilities for innovation.

2
Light scattering in nanomaterials & Random Lasers

This chapter describes various characterization techniques utilized to quantify the scattering efficiency of different nanomaterials. The initial section provides a brief overview of the fundamental physics of light scattering. The chapter then transitions into two sections: one dedicated to cellulose nanocrystals [1] and the other to quartzite nanoparticles [2], both of which have been extensively characterized and identified as highly efficient for light scattering purposes.

2.1. Light scattering phenomena

Light is rarely observed directly from its source [3]. Most of the light we perceive reaches our eyes indirectly. When we look at a house or a car, we see sunlight that has been diffusely reflected. When gazing at a cloud far in the sky, we see sunlight that has been scattered by atmospheric particles. Even a lamp typically does not emit light directly from its source filament; instead, we observe light that has interacted in various ways with the surrounding glass bulb. When studying light and its applications, it is inevitable that we face problems that require us to understand the phenomena of light scattering.

This phenomenon is often accompanied by absorption. A leaf from a tree looks green to the human eye because it scatters and reflects that color while absorbing the others, meaning part of the energy of the light is converted into some other form, which for most will be irrelevant for our purpose.

Scattering and absorption both contribute to the reduction of energy in a beam of light as it propagates through a medium, a phenomenon that will be referred to as extinction. The extent of this attenuation depends on the optical path length, which determines the degree of interaction between the light and the medium. For instance, sunlight appears weaker and redder at sunset compared to noon, illustrating that extinction is more pronounced for blue light over the longer atmospheric path.

Light scattering plays a crucial role in a wide range of applications across science and technology. In biomedical imaging, it is used to diagnose diseases through techniques like optical coherence tomography [4] and Raman spectroscopy [5], which rely on the interaction of light with biological tissues. Environmental monitoring benefits from light scattering in the analysis of atmospheric particles [6], aiding in the detection of pollution and the study of climate change. In material science, scattering measurements provide insights into the structural and optical properties of nanomaterials [7], enabling advancements in photonic devices and sensors. Finally, light scattering serves as the foundation for the development of random lasers, which will be the primary focus of this chapter. Random lasers not only have a wide range of applications but also provide a valuable framework for analyzing and understanding the scattering efficiency of various nanomaterials, which is one of the things I focused on during my research.

2.2. (Random) Lasers

The principle of Light Amplification by Stimulated Emission of Radiation, or LASER, (almost) describes the core mechanism behind the operation of lasers. In conventional lasers, a pump source energizes the gain medium, leading to a population inversion where electrons in the materials' atoms are elevated to higher energy states [8]. When these excited electrons return to their ground state, they emit photons coherently, resulting in optical amplification within a well-defined resonant cavity, such as mirrors or fiber loops, which ensures directional and highly monochromatic emission.

In contrast, random lasers operate without a traditional resonant cavity. Instead, their lasing relies on multiple scattering events within a disordered gain medium, which randomizes the photon paths. This unique configuration results in spatially incoherent but spectrally narrow emission. As discussed earlier, scattering usually contributes to the reduction of energy of the original beam of light. In the case of a random laser the material responsible for scattering may be, in the most conventional architecture, doped with or suspended in a fluorescent solution that will allow for optical feedback to happen after each scattering event.

The first demonstration of sustained oscillation in a pumped gain medium without the presence of mirrors or a closed cavity was reported in 1966 by R. V.

Ambartsumyan and Nobel laureate N. G. Basov [9]. They described their discovery as “a laser with non-resonant feedback.” Two years later, V. S. Letokhov published pioneering work proposing the “generation of light by a scattering medium with negative resonance absorption” [10], and in the following year presented a comprehensive review and outlook on “non-resonant feedback in lasers,” laying the groundwork for what we now refer to as random lasers. I highly recommend reading through Letokhov's early work as it is highly interesting and theoretically explores several configurations for open cavities and non-resonant feedback schemes, some of which they accomplished experimentally, and for others they were way ahead of their time.

The real breakthrough in demonstrating laser action in strongly scattering media was only realized in 1994 [11]. This was accomplished using a colloidal suspension composed of an organic fluorescent dye as the gain medium and nanometer-sized rutile (TiO_2) nanoparticles as the scatterers. The gain medium was excited by nanosecond pulses from the second harmonic of a Nd:YAG laser, while the rutile nanoparticles provided the optical feedback required for lasing.

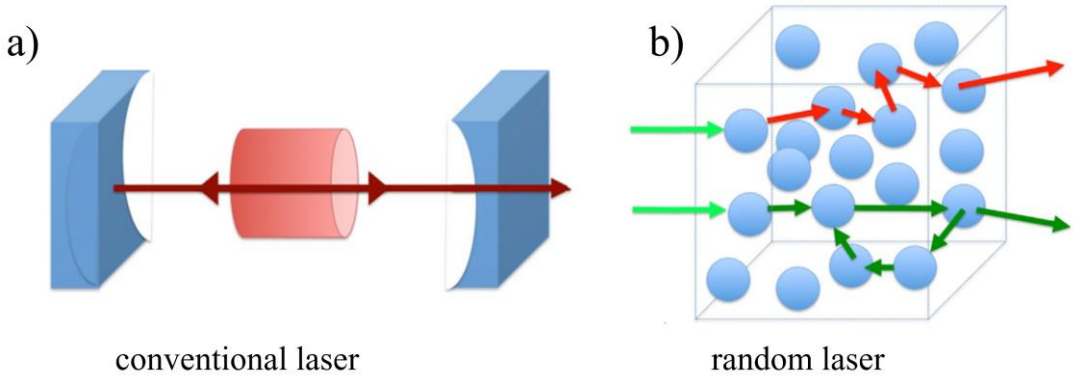

Figure 2-1: (a) conventional and (b) random laser schemes.

In our work we used a very similar system to determine the scattering efficiency of different organic materials, as will be seen in the next subchapters.

Recently, various work described the physics of RL discussing in [12,13], [14,15] and [16], the Poisson and Bose-einstein statistics for random lasers, Lévy regimes for light scattering and the glassy behavior of light, respectively. More than that, Table 1 from the recent review reported in [17] offers a great overview of breakthroughs in the field and a collection of articles and book chapters on the topic.

2.3. Identifying random laser action

Back in 2018, when I first started working with Isabel as an undergraduate research assistant, I remember making my first random laser samples and obtaining great results. That was only to find out later, when I did a test with only Rhodamine 6G and no scatterers, that the laser emission I was observing was a result of the cylindrical vial having whispering gallery modes [18]and my excitation laser being misaligned. Or due to the excitation beam being perpendicular to the cuvette faces and the internal reflections making a cavity that would sufficiently excite anything fluorescent that I put inside of it.

There are many ways to determine if a sample is *lasing*, but it may still be tricky. Sometimes the hard part is determining whether the feedback is indeed being generated by the scattering material instead of other factors as stated above.

As outlined in the previous section, the key requirements for random lasing are the presence of net optical gain and multiple scattering. Multiple scattering occurs when the sample size (L) exceeds the transport mean free path (TMFP, l_t). Considering the scattering efficiency and the wavelength of light, RLs can be divided in two main categories .

Anderson-localized random lasers occur under conditions of strong scattering ($l_t < \lambda < L$), where closed scattering paths result in strong interference. This leads to the formation of spatially localized modes and lasing peaks with linewidths typically ranging from 0.01 nm to 0.1 nm. In these systems, the mode linewidth is narrower than the mode spacing, meaning the modes do not overlap and remain uncoupled, apart from indirect coupling through the optical gain (Fig. 1e).

Delocalized random lasers, also referred to as diffusive, occur under weaker scattering conditions ($\lambda < l_t < L$). In this regime, optical modes are broad, resulting in extended optical modes that span the entire system. Typically, due to temporal and/or spatial averaging, no distinct sharp peaks are observed. Instead, an overall line narrowing is seen around a broad lasing peak, reducing the emission linewidth from ~50–100 nm (spontaneous emission) to a few nanometers under lasing conditions, as observed with typical laser dyes.

The most common experimental evidence for random lasing action is the observation of a threshold pump intensity, which is the metric mostly used in this work. This is identified by an intense increase of emitted fluorescence intensity that

increases superlinearly with pump power, exhibiting a pronounced change in its linear plot. This behavior serves as a clear indicator of fluorescence being overtaken by stimulated emission. This is accompanied by a strong reduction in the full width half maximum of the emission spectra, as spontaneous emission is surpassed by a stimulated narrow band. This characteristic spectral narrowing, often used as evidence of lasing phenomena, serves as an equivalent measure of the increase in the temporal coherence of light.

I highly recommend Nature expert recommendation written by Riccardo Sapienza [19], as it clarified to me the properties and why a random laser is actually a laser, which has been discussed in literature for some time in the early 2000s. In this work he also discusses other metrics regarding photon statistics, experimentally assessed by the second order correlation and single mode intensity statistics shift from Bose-Einstein to Poisson statistics from below to above threshold, as well as the theoretical background in coherence, mode selection and laser dynamics fluctuations.

2.4. Cellulose nanocrystals

The first material I will be addressing in this dissertation is cellulose nanocrystals. The idea of testing this material as scatterers for random laser systems comes from our collaborators Susete N. Fernandes and Maria H. Godinho from i3N/CENIMAT (Universidade Nova de Lisboa), who wanted to test bio-degradable scatterers and have vast experience in developing cellulose materials and their electrical and optical properties.

I worked both on the conventional fluorescent dye suspension random laser configuration with cellulose nanocrystals as scatterers and on a new flexible solid film made with hydroxypropyl cellulose utilizing the same scatterers, which opens to different applications as I will discuss in 2.4.6 (Phototherapy Device & Applications).

Results hereby reported are partially published in the Journal of the Optical Society of America, v. 37, n1, p24-29 [1] and were presented in CLEO Europe [98].

2.4.1. Materials & methods

The cellulose nanocrystals used were obtained from microcrystalline particles produced from cotton, as described in [20]. Cotton fiber is the purest source of cellulose found in nature as it presents a higher content of cellulose among plant cells. The nanocrystals were provided by our collaborators and used as received after undergoing a freeze-drying process (Zirbus, VaCo 2). They were supplied in the form of white flakes composed of multiple cellulose nanocrystals.

To obtain the liquid suspension for the random laser samples, different amounts of CNCs were diluted in an ethylene glycol (Reagen, 99.8%) solution of Rhodamine6G (Sigma Aldrich, powder dye-content ~95%) at 1.0 mM concentration. Tests were performed with samples containing 1.0 mg/mL, 2.0 mg/mL, 5mg/mL, 7.0mg/mL, 10 mg/mL and 15mg/mL concentrations of CNCs as scatterers. After making the suspensions, they were then sonicated until the complete dispersion of the cellulose nanocrystals in the suspensions. Suspensions with scatterer concentration under 1 mg/mL and over 15 mg/mL are not further studied since they are highly inefficient for random lasing.

To obtain the solid film suspensions, 0.22 g of HPC (Sigma Aldrich 99%, average MW=100.000) and 1.0 mg of CNC were added to 2.0 mL of distilled water and then sonicated (130 W, Sonics Vibra-Cell CV18) for three 5 min sessions for complete dissolution of HPC. Afterwards, 100 µl of a 1.0 mM EG solution of RH6G were added to the HPC ultrasound bath (Ultraclear 700, 50 kHz) for 5 min. The final suspensions were drop casted on polypropylene molds with 3.5 cm x 2.0 cm and dried in an oven at 60 °C for ~1 h, forming a film with 70µm thickness.

In all the work presented in this dissertation, Rhodamine 6G (Rh6G) suspensions at a concentration of 1 mM in ethyleneglycol (EG) were used [21,22]. This choice was made to ensure consistency and facilitate comparison with recently published studies, which commonly employ the same fluorescent dye under similar conditions.

Random laser measurements were made right after sample preparation and drying process for suspensions and films, respectively.

2.4.2. SEM characterization of CNC needles

To verify the average dimensions of the cellulose nanocrystals (CNCs), aqueous suspensions at a concentration of 0.01 wt.% were prepared, and droplets were deposited onto aluminum stubs. The samples were allowed to evaporate at room temperature and then coated with a thin carbon layer using a Q15-T ES Quorum sputter coater. Images of the CNC flakes were captured using a JEOL JSM 6701F SEM-FEG, while individual crystals were imaged using a Carl Zeiss Auriga crossbeam (SEM-FIB) workstation, operated at 2.0 kV and 5.0 kV respectively.

To measure the average dimensions of the nanomaterial, ImageJ software (version 1.45s) was used, and values of 135±48 nm and 4±1nm for length and diameter of the nanoneedles were determined. Figure 2-2 shows the images obtained through electron microscopy, showing the morphology of the CNC flakes (macro-sized agglomerates, Fig. 2-2a,b) and as individual needles (Fig. 2-2c).

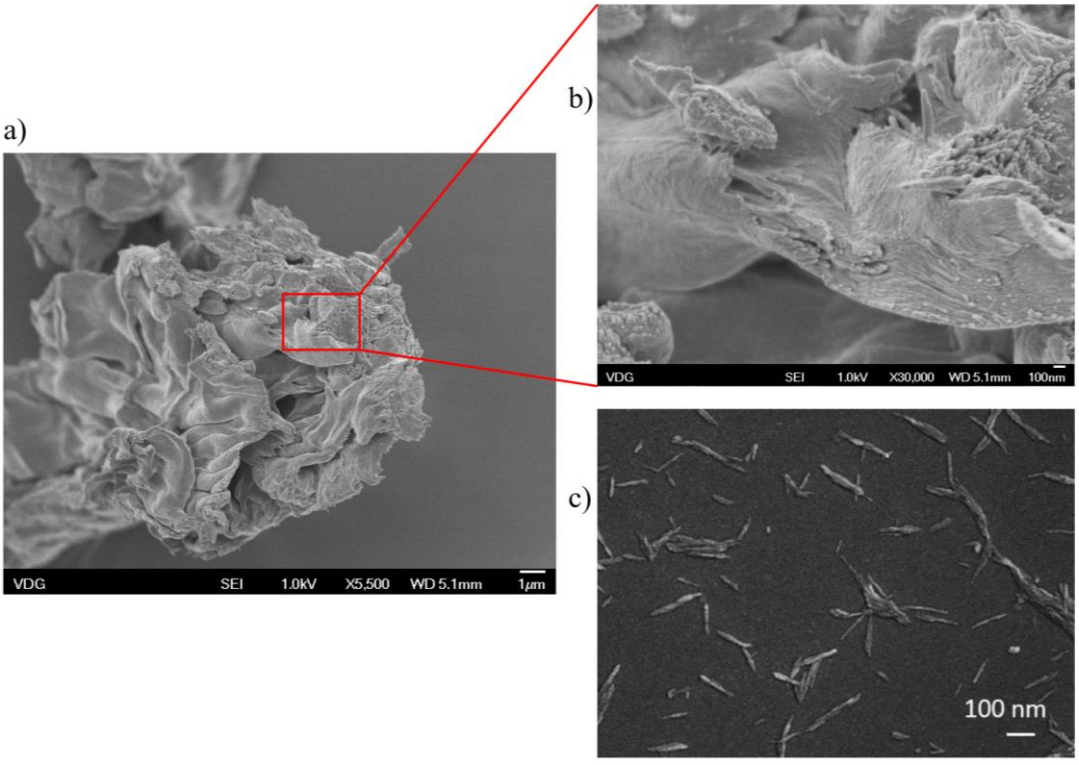

Figure 2-2: Images obtained by SEM-FEG (a) of the CNCs as in flakes (macro-sized agglomerates), (b) cross section and (c) of the individual needles after sonication.

As can be noticed, the CNC flakes are formed by nano-fibrillated cellulose [20]. In the agglomerates the needles stack up in a self-organized form perpendicular to the cross section break of the material. After the sonication

process, only needles are left in the fluorescent suspensions, and they are responsible for providing the scattering needed for the optical feedback in the random laser system.

2.4.3. SEM characterization and polarized optical microscopy of HPC+CNC solid films

The polarized optical microscopy images (Figure 2-3), obtained using a Leica DM2500 optical microscope, reveal no evidence of CNC clustering in either the HPC or HPC + CNC solid films. Such clustering, if present, could influence the RL efficiency due to a very small scattering mean free path, not allowing scattered photons to interact enough with the fluorescent material to provide feedback. In reference [20], hierarchical self-organized cholesteric are detected and noticeable through polarized light domains being present both in microscopic and macroscopic scales.

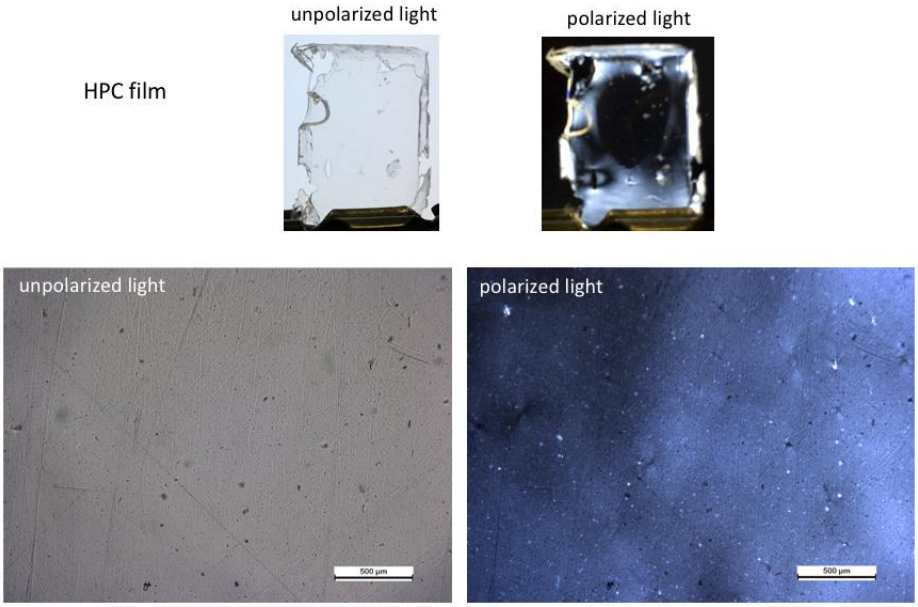

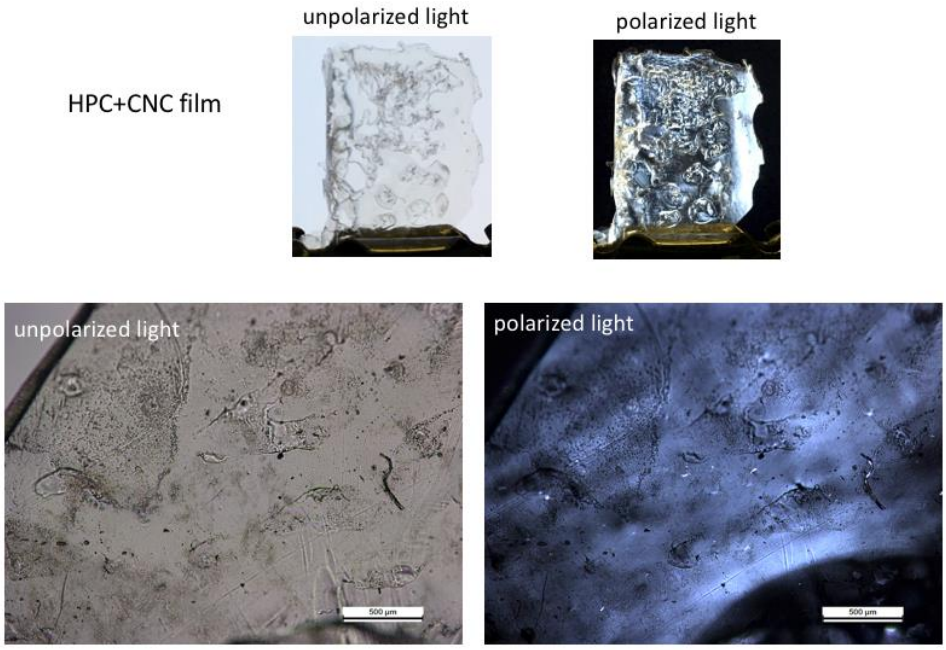

Figure 2-3: Digital photographs and light-polarized optical micrographs of HPC (above) and HPC+ CNC (below) films.

The observed light contrast in the polarized optical microscopy images for both films arise from the intrinsic birefringence of the composites. Despite their transparency to visible light, birefringence emerges due to the presence of two phases with differing refractive indices. These findings further confirm the absence of hierarchical CNC clustering in HPC films.

Nevertheless, this does not imply that the distribution of CNC needles is entirely random. Field-emission scanning electron microscopy (FEG-SEM) images of the HPC+CNC film cross-section (Fig. 2-4), acquired using a JEOL JSM 7100FT, indicate that the CNC needles are predominantly aligned in stacked layers along the film's longitudinal axis. On a macroscopic scale, this alignment suggests a long-range morphological organization.

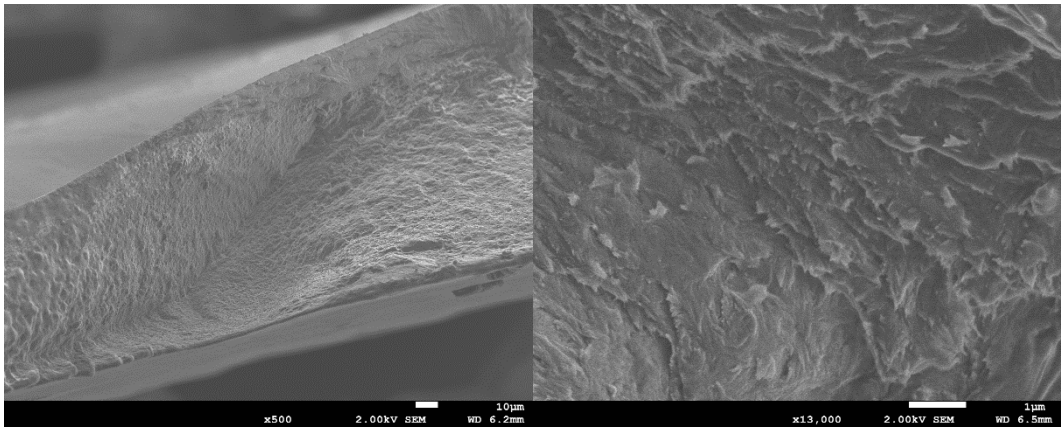

Figure 2-4: FEG-SEM images of HPC film containing 5 mg/mL of CNC.

2.4.4. Experimental details

The lasing spectra of all samples were measured upon excitation with a pulsed frequency-doubled Q-switched Nd:YAG laser (Brio-Quantel, Ultra, 6 ns) operating at 10 Hz. The excitation beam (λ = 532 nm) intensity was controlled through a half waveplate together with a polarizer, carrying a maximum of 9 mJ with a 2.1 mm beam diameter. A 75 mm convex lens was used to collect the RL emission and direct into the collector fibre plugged to the spectral analyser. The spectrometer used was an Ocean Optics USB4000-UV-VIS (1.5 nm spectral resolution in visible range). The measurements of all samples were recorded under identical experimental conditions and carried out at room temperature. Experimental setup can be seen in Figure 2-5 with all equipment and details listed.

The Nd:YAG laser has its centre emission at 1064 nm, and was used with a frequency doubling crystal that offers around 30 % energy efficiency. To remove unwanted infrared radiation from exciting and burning the samples, we used a harmonic beamsplitter or dichroic mirror (99% 1064 nm reflectance at 45 degrees) and a coloured filter.

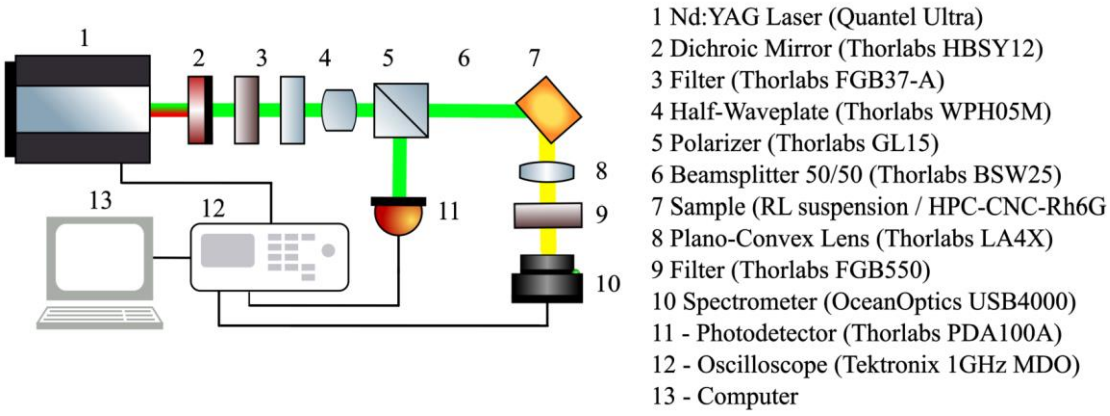

Figure 2-5: Experimental setup used for RL characterization (left) and each component in details (left).

To record the lasing spectrum excitation light is directed at the 10 x 10 mm quartz cuvette with the suspension at 45 degrees. If we don't do that, lasing may occur as in the case of a Fabry-Perot cavity due to internal reflections on the 10 x 10 mm cuvette walls [19]. It is also important to avoid using cylindrical vials, which may also evidence lasing phenomena due to the excitation pump forming stationary

waves in the form of whispering gallery modes, strongly exciting the fluorescent dye in place of the scattering events, as discussed before.

2.4.5. Random laser results

2.4.5.1. CNCs + Rh6G suspension

The lasing emission from the CNCs + Rh6G suspension is evidenced by a spectral narrowing for samples under increasing excitation energy. For samples of all concentrations, the full width half maximum (FWHM) is strongly reduced from 60 nm to ~8 nm, from below to above the lasing threshold, as can be seen in Figure 2-6.

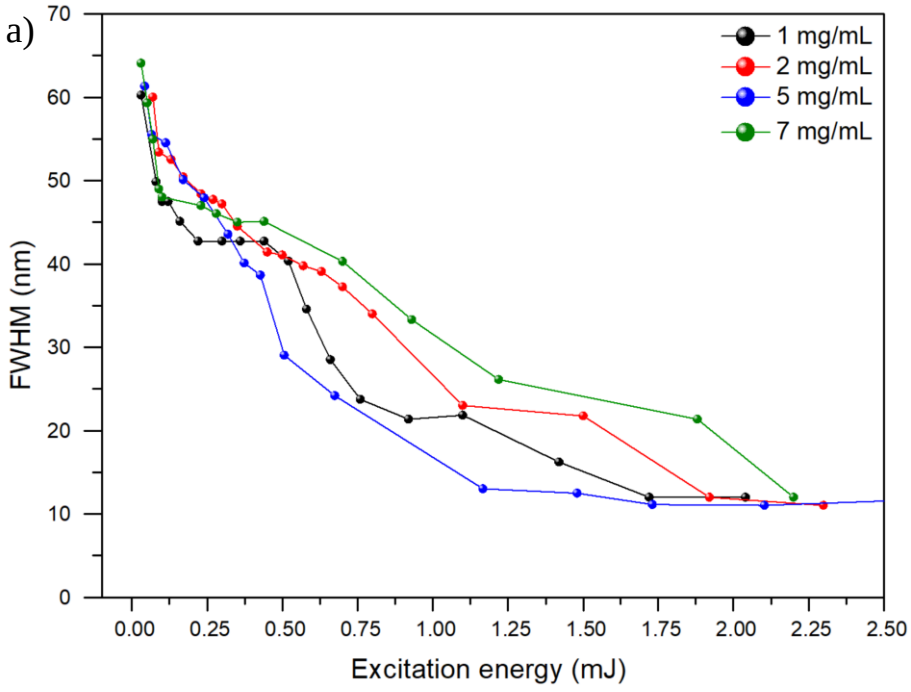

b)

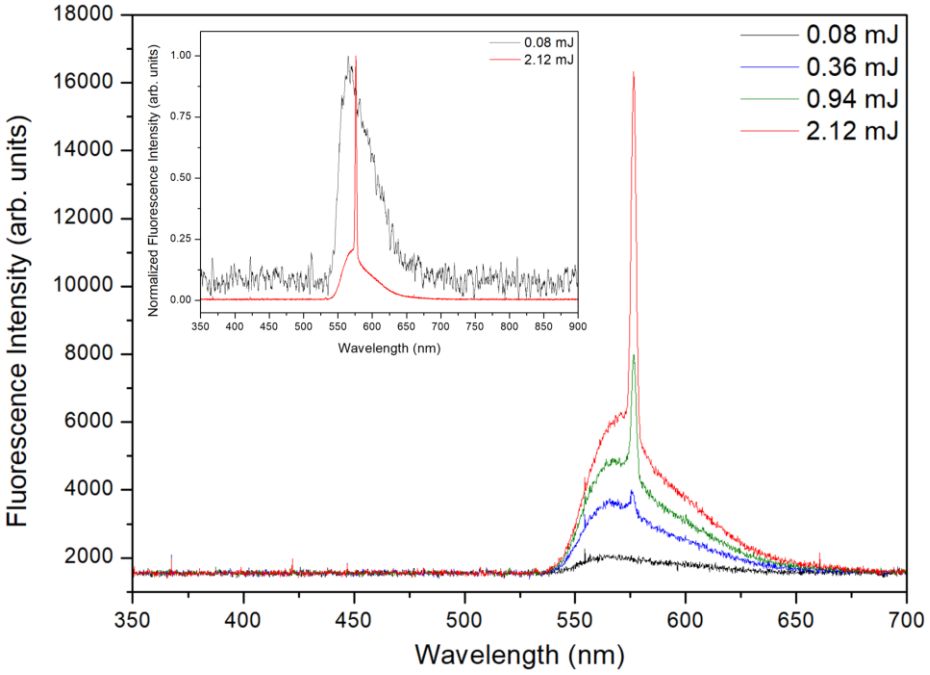

Figure 2-6: (a) Full width half maximum as a function of the excitation energy for different scatterer concentrations; (b) fluorescence intensity for increasing energies (inset shows normalized data for energy below and well above threshold).

The emitted intensity is highly affected by the incorporation of more scatterers into the laser system. Figure 2-7 shows the emission intensity in a logarithmic scale to reveal the threshold energy for different CNC concentrations. For the optimal case, in which we used 5 mg/mL scatterer concentration, the RL efficiency greatly improves with a threshold of 0.35mJ, which corresponds to 50% of the energy threshold for a sample with same dye concentration and 1 mg/mL CNCs. Above the optimal concentration we also have a decrease in efficiency, which is discussed later in the text. For scatterer concentrations above 10 mg/mL, lasing action does not occur.

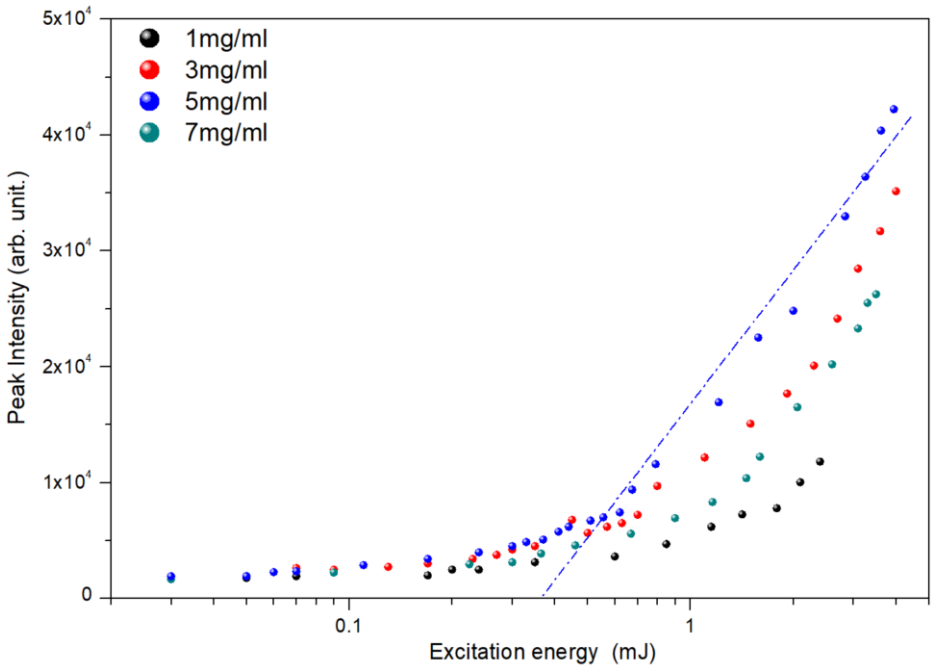

Figure 2-7: Logarithmic peak fluorescence intensity as a function of the excitation energy for different concentrations. The extrapolated line shows indicates the lasing threshold for the most efficient sample.

2.4.5.2. HPC + CNC flexible film & comparison

The self-supported, flexible HPC-CNC-Rh6G random laser (RL) was systematically characterized and its performance compared to that of the CNC-Rh6G suspension RL, as can be seen in Figure 2-8 highlighting the linewidth reduction and the emitted intensity as functions of input power. It is important to note that the film samples contain approximately 10% fewer CNC needles compared to the suspension format. Despite this difference, both formats exhibit a similar energy threshold of ~0.3 mJ. However, for the film sample, the excitation energy was limited to a maximum of 1 mJ to prevent sample degradation, which occurred at higher energy levels and will be discussed in the next subsection.

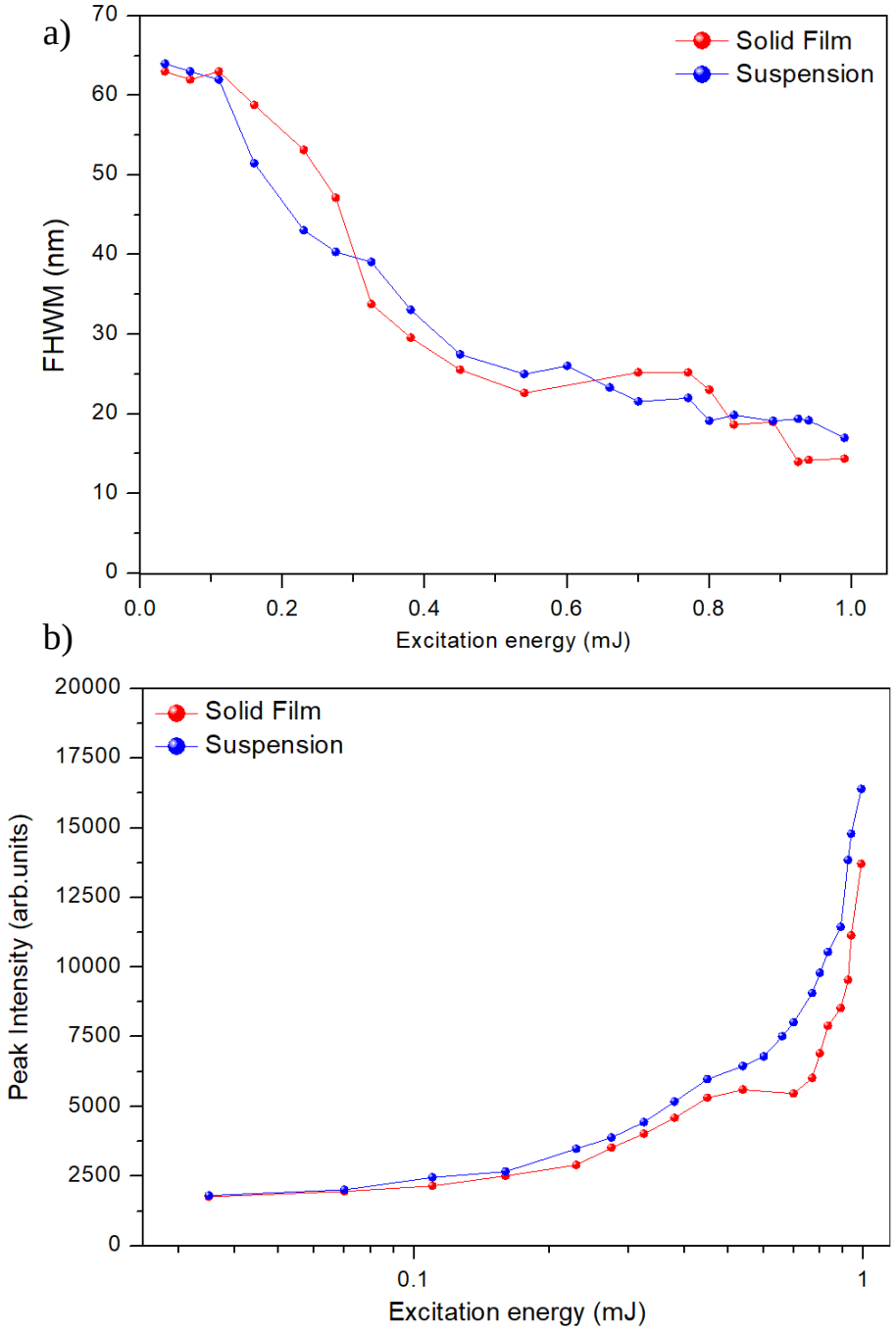

Figure 2-8: (a) FWM as a function of the excitation energy and (b) logarithmic peak fluorescence intensity as a function of the excitation energy for both samples.

It is important to highlight that the self-supported film configuration offers enhanced flexibility and allows the RL to operate without relying on feedback from a solid substrate. This unique characteristic, combined with the physicochemical properties of the starting suspension used to cast films such as viscosity and colloidal stability suggests significant potential for many applications, such as cheap compact alternatives to bulky diodes commonly used in fluorescence-based detection devices [23].

Scatterer concentration of CNC in the solid sample was 10.2 mg/cm³ and Rh6G concentration 4.92 x 10^{18} molecules/cm³; for the most efficient suspension plotted, the concentrations were 5 mg/cm³ and 5.47 x 10^{17} molecules/cm³.

In the solid-film system, both the CNC and Rh6G concentrations are higher than in suspension. However, in the thick HPC-CNC film, the laser beam traverses a considerably shorter optical path compared to the 10 x 10 mm in the cuvette. This results in a considerable reduction in the intensity of Rh6G emission. Despite this, the HPC-CNC film demonstrates excellent scattering properties, as evidenced by its threshold value being comparable to that of the liquid suspension.

Additionally, the film exhibited a distinct pink color when dry after few hours. This coloration can be attributed to a shift in the peak maximum of its absorption band relative to the monomer peak position, suggesting the formation of J-type aggregates, while in the liquid suspension the absorption indicates not only monomers but also other types of aggregates (H & J types), which may justify the reduction in the overall emission intensity.

An important limitation of organic-based random lasers (RLs) is their operating lifetime under continuous pumping. To evaluate the degradation of the random laser in the thick film configuration, the variation in FWHM and intensity as a function of the number of laser shots, above threshold (0.96 mJ), was analyzed (Fig. 2-9). The RL intensity decreased by 50% after approximately 7,500 shots at a repetition rate of 10 Hz, corresponding to ~10 minutes of operation. Concurrently, the FWHM broadened by 40% from its initial value of ~10 nm, eventually reaching 40 nm. This low operational lifetime is a well-known characteristic of colloidal cellulose based RLs. A potential solution to this limitation is to employ solid-state gain media, such as rare-earth-doped nanoparticles or semiconductor-based nano- and micron-sized structures, which offer improved stability and longevity under pumping conditions, or to excite the material through an optical fiber to provide better energy distribution from inside the material.

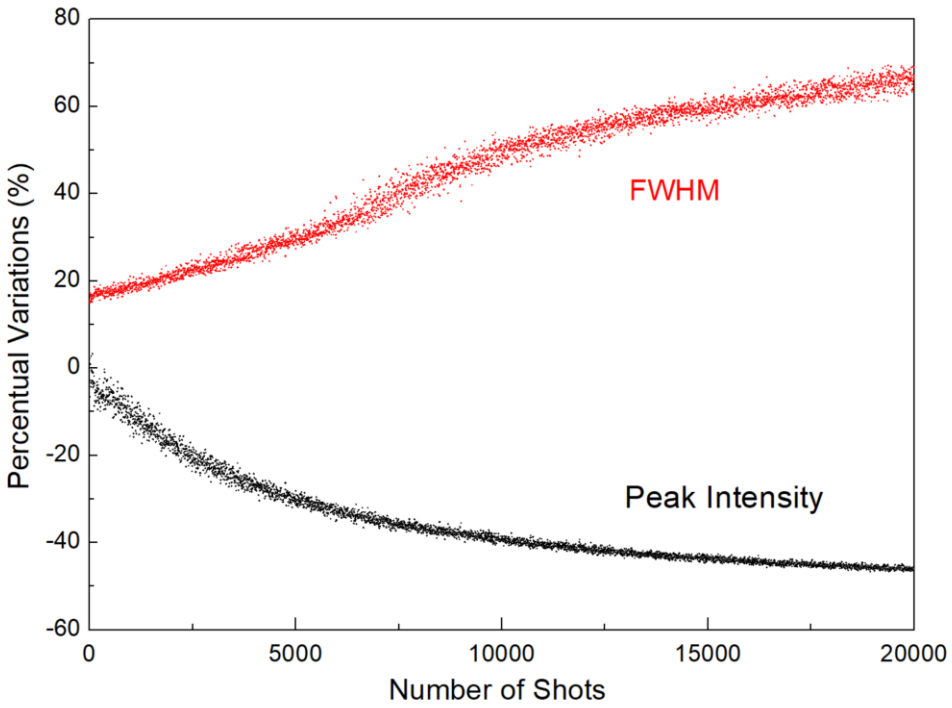

Figure 2-9: Degradation of the random laser by the variation of the FWHM and the intensity as a function of the number of shots. Degradation measurement is done at 0.96mJ and the repetition rate at 10Hz.

I also recommend checking Table 1 from our published work [1], (Survey of Cellulose-Based Random Lasers) or Appendix A.1 where we compare our results and sample efficiency with previously published work.

2.4.6. Phototherapy device & applications

Phototherapy (also known as light therapy) has revolutionized medical treatment by offering non-invasive solutions for a variety of medical conditions. The technique consists in the exposure of the skin to specific wavelengths of electromagnetic radiation, usually from ultraviolet (UV) to near infrared (NIR). Exposure to UVA1 light (λ=340-400nm) penetrates deep into the reticular layer of the dermis which can suppress components of cell-mediated immune function by acting on fibroblasts, dendritic cells and inflammatory cells (particularly T-cell lymphocytes and mast cells) [24]. UVB radiation (λ=270-350nm) works in treating skin conditions such as psoriasis by suppressing DNA synthesis, reducing inflammation, and enabling the body to produce vitamin D3 to prevent deficiency [25]. According to the American Cancer Society, UV light therapy might also be

effective in treating some types of cancer through blood irradiation therapy [26]. Moving to the visible-range, blue light (λ=420-490nm) is often used to treat neonatal jaundice, which is caused by an excessive bilirubin accumulation that can cause damage to the central nervous system (CNS) and is neutralized with this wavelength due to bilirubin peak absorption and its isomerization when exposed to blue light [27]. Acne attenuation is also a common use of light-based therapies, with narrowband red light (λ=660nm) and pulsed dye lasers (λ~585nm) presenting bactericidal effects, disrupting sebaceous gland functions and exerting anti-inflammatory action [28]. White light sources are also commercially available and said to prevent depression and seasonal affective disorder (SAD), but conclusive studies on the topic were not able to determine whether the therapy is more effective than placebo in regulating the circadian rhythm [29]. These are only a fraction of the applications of light as treatment for diseases, as the field is rapidly expanding. Light sources for phototherapy are diverse, and for now very few RL phototherapy devices have been proposed [30-32].

An important feature of the cellulose nanocrystals is their high scattering cross section across all visible range [20,33]. This fact, combined with the high efficiency of our material and flexibility in the form of a solid film, provide a great platform for phototherapy devices.

We are currently working together with Prof. Denise Zezell (Institute for Nuclear and Energetic Research, IPEN) and working in developing tuneable phototherapy device.

The synthesis procedure is the same reported in section 2.4.1 (Materials and Methods) of this document, but during the drying process a Corning SMF28 optical fibre is positioned into the cast through an incision and remains connected to the flexible film after the drying process. This fibre guides the excitation light directly into the sample increasing its efficiency and preserving its small size and non-toxicity. During tests I was able to reduce the size of the sample down to 1 x 1 mm, still guaranteeing its lasing properties, which is valuable for situations where you need to excite hard to reach areas (Figure 2-10, inset shows pictures of the fluorescent film).

This innovative phototherapy platform offers tunability in both intensity, through variation in excitation energy, but also emission wavelength, which can be adjusted by simply selecting a different fluorescent dye. Additionally, the emitted

light polarization can be controlled by varying the concentration of cellulose scatterers.

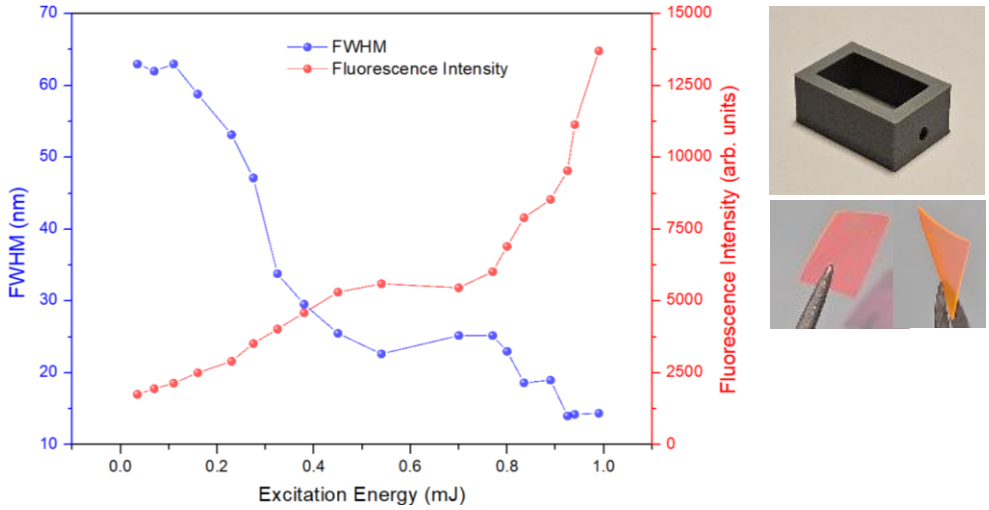

Figure 2-10: (left) FWHM and peak fluorescence intensity as a function of the excitation energy for the film sample being excited by an internal optical fibre. (right) Cast with the insertion for the optical fibre and samples.

2.5. Quartzite & silica nanoparticles

Another material I extensively investigated during my master were quartzite nanoparticles (QtzNPs). These studies provided valuable insights into how nanoparticle morphology influences the efficiency of light scattering in random lasers.

RLs with nonresonant feedback based on Rh6G with sub-micron scatterers are widely studied. The quantum efficiency of the Rh6G solution is influenced by dye concentration, whereas the emission efficiency of the RL is strongly dependent on the transport mean free path (TMFP) [19]. The TMFP is, in turn, determined by the size, composition, concentration, and morphology of the scatterers. Among these factors, the impact of scatterer morphology on lasing efficiency remains comparatively underexplored in literature.

In the attempt to find a more cost-effective and highly efficient material for light scattering applications, I explored several natural silicon-based materials, both in natural form and ground, with the support of Dr. Edison Pecoraro (São Paulo State University), a long-time collaborator and expert in materials science who provided valuable insights throughout this work. Among tested materials, I did

experiments with jeans fibres, selenite, muscovite, ulexite, agate and white marble, all proving not sufficiently efficient for lasing or showing very low efficiency leading to a high excitation energy threshold.

Quartzite, on the other hand, proved very effective, as will be discussed moving forward in this section. Comparisons were also done between this novel material and conventionally used amorphous silica nanoparticles (ASNPs), which are one of the most studied scatterers in literature, in order to determine its efficiency and the effect of morphology and the crystalline character in the laser emission. All experimental findings are also validated with finite element method (FEM) simulations.

Results hereby reported are partially published in Elsevier's Optical Materials (OM) journal, Volume 148, 114775 [2] and were presented in LAOP [99].

2.5.1. Materials & methods

Although amorphous silica nanoparticles with spherical or undefined morphologies are commercially available or can be synthesized with relative ease, nano- or micro-sized crystalline SiO_2 particles (quartz) are significantly more expensive and challenging to obtain [33]. To address this, the present work utilizes crystalline particles derived from a natural and cost-effective mineral source: quartzite. Quartzite is a hard, non-foliated metamorphic rock formed from pure quartz sandstone [34]; a sedimentary rock primarily composed of sand-sized (0.0625–2.00 mm) quartz-silicate grains. Through exposure to extreme heat and pressure, typically associated with tectonic processes such as compression in orogenic belts, sandstone is transformed into quartzite.

Quartzite consists of aggregates of micro- and nano-sized quartz particles with slab-like shapes, offering a higher refractive index (n = 1.54) compared to amorphous SiO_2 (n = 1.46) across the visible wavelength range. This makes quartzite a compelling choice for applications requiring crystalline SiO_2 particles.

QtzNPs were obtained by grinding quartzite rocks in a high-hardness agate mortar for several minutes, until minimal particle size is obtained. ASNPs were store bought (Column Chromatography silica gel QingdaoH > 99%) and undergone the same process.

Random laser samples were prepared using Rhodamine 6G (Sigma-Aldrich, 95%) dissolved in ethanol (Sigma-Aldrich, >99.9%) and methanol (Sigma-Aldrich, 99.7%). While these solvents enabled lasing, their low viscosity proved inadequate for maintaining a stable suspension of particles. Within a few minutes, particle precipitation was observed at the bottom of the container.

To address this issue, ethylene glycol (EG) (Sigma-Aldrich, >99%) was selected as an alternative solvent. Although EG exhibits slightly lower quantum efficiency compared to ethanol, which affects the lasing threshold energy [22], due to its higher refractive index (1.43) relative to methanol and ethanol (1.36). Additionally, the increased viscosity of EG effectively prevents particle precipitation, enabling the formation of permanently stable suspensions.

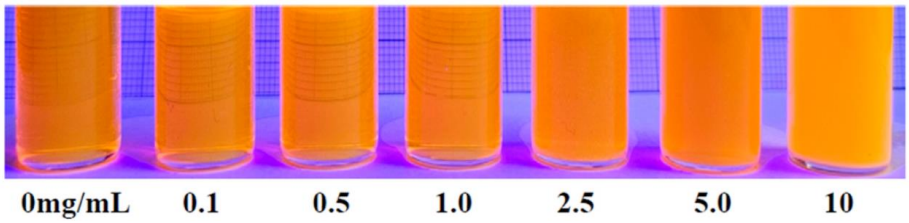

Figure 2-11: Photos of the samples with different scatterer concentration under UV illumination, showcasing change in the transmission.

Quartz aggregate-based materials exhibit a higher refractive index compared to amorphous silica particles across all visible wavelengths [34]. It is well-established that the refractive index contrast between the gain medium and the scatterers significantly influences the efficiency of RLs. The elevated refractive index of quartz nanoparticles (QtzNP) arises from their crystalline structure, which enhances surface reflectance for visible light. This characteristic further explains the superior performance of micro-sized scatterer agglomerates and particles.

2.5.2. SEM characterization of quartzite and amorphous silica

To confirm the average size and morphology of QtzNP and ASNP, random laser (RL) suspensions were deposited onto aluminum stubs, dried, and coated with a thin gold layer using a Q150T ES Quorum sputter coater. The imaging was performed using a TESCAN Clara (UHR-FEM) electron microscope, as shown in Fig. 10. Particle size analysis was conducted using ImageJ software (version 1.45s),

revealing sizes ranging from 50 nm to 500 nm, with an average size of 225 nm for QtzNP and 100 nm for ASNP.

Additionally, energy-dispersive X-ray spectroscopy (EDS) microanalysis confirmed that both ASNP and QtzNP are composed of 72.39% oxygen and 27.61% silicon, with none of the common detectable impurities such as hematite, zirconia, or titania.

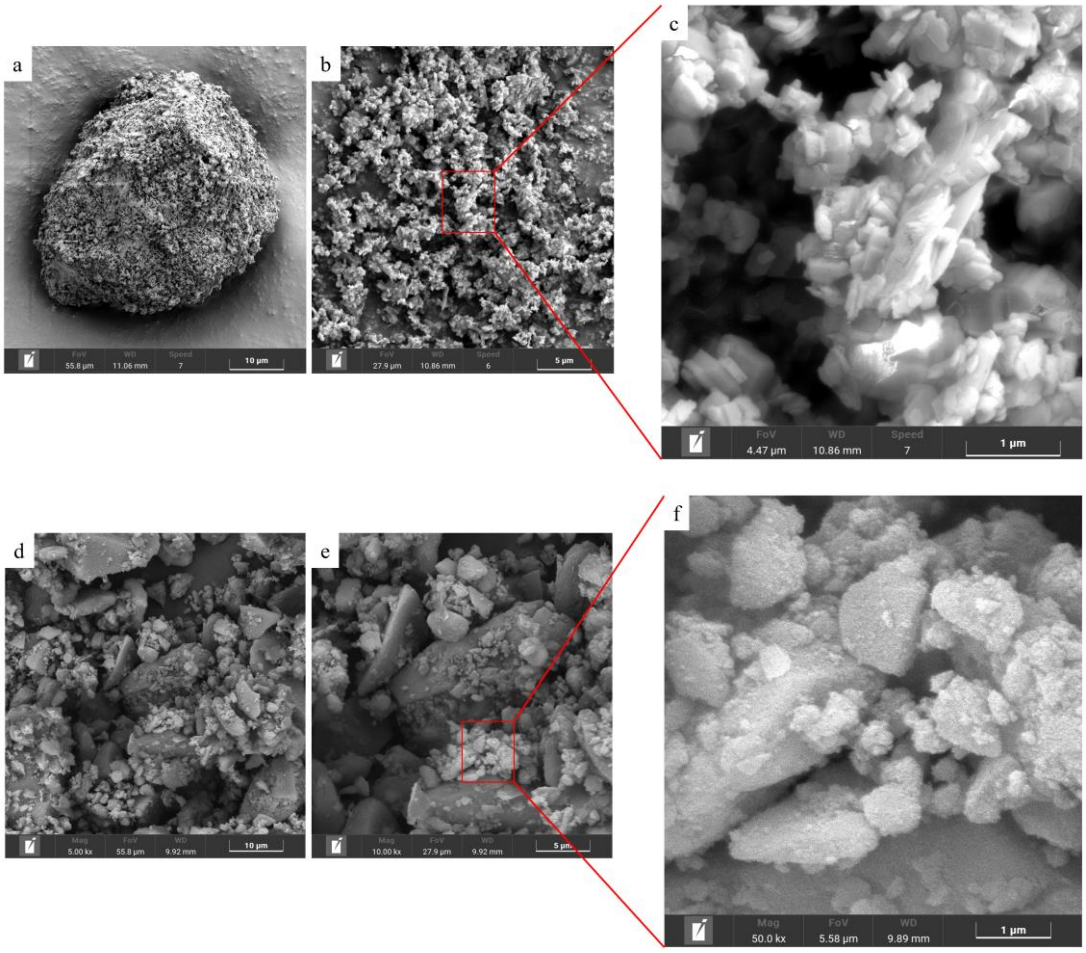

Figure 2-12: Images obtained by SEM-FEG of (a–c) quartzite as agglomerates and nanocrystals and (d–f) amorphous silica nanoparticles.

2.5.3. Random laser results & comparison

Experimental conditions, setup and details used for the analysis of this material are the same as reported in section 2.4.4.

The laser emission from the samples is evidenced by a notable spectral narrowing of approximately 30 nm under increasing excitation energy. Additionally, we can observe the exponential growth in fluorescence intensity as a function of excitation energy, culminating in a well-defined laser threshold. This

threshold marks the point at which optical gain from feedback within the fluorescent medium surpasses losses due to absorption.

The most efficient QtzNP sample exhibited a full width at half maximum reduction of approximately 85%, decreasing from 44.2 nm to 6.9 nm, as the system transitioned from below to well above the threshold excitation energy. Similarly, the most efficient ASNP sample showed a FWHM reduction of approximately 77%, from 47.32 nm to 10.8 nm, under the same conditions, as can be seen in Figure 2-13.

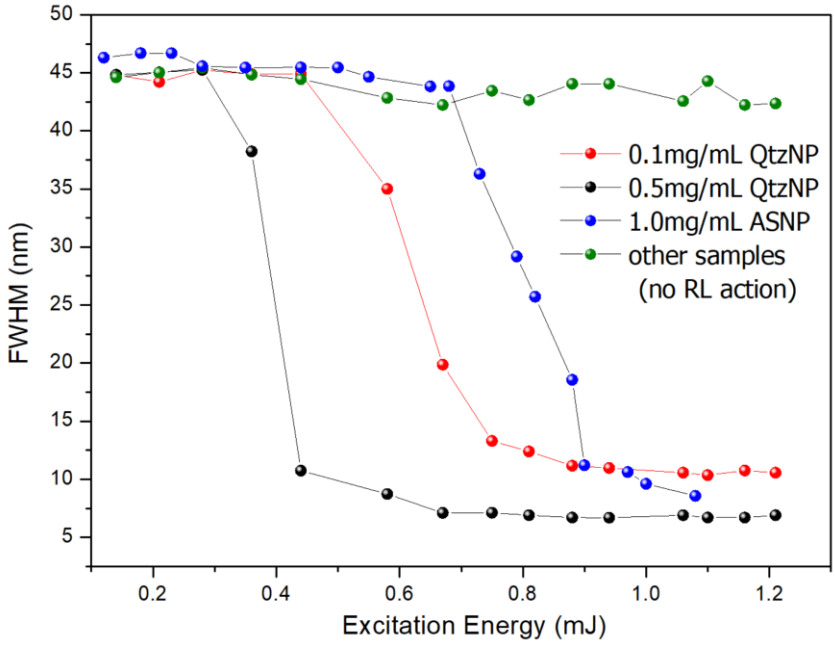

Figure 2-13: FWHM of Rh6G emission as a function of the excitation energy for different QtzNP/ASNP concentrations in the suspension.

Figure 2-14 presents the emission intensity as a logarithmic plot, enabling the analysis of the RL response for various scatterer concentrations and the determination of the RL threshold for each suspension concentration. The optimal concentration for QtzNP was identified to be 0.5 mg/mL, with a corresponding threshold energy of 0.25 mJ. For ASNP, the optimal concentration was 1.0 mg/mL, with a threshold energy of 0.55 mJ.

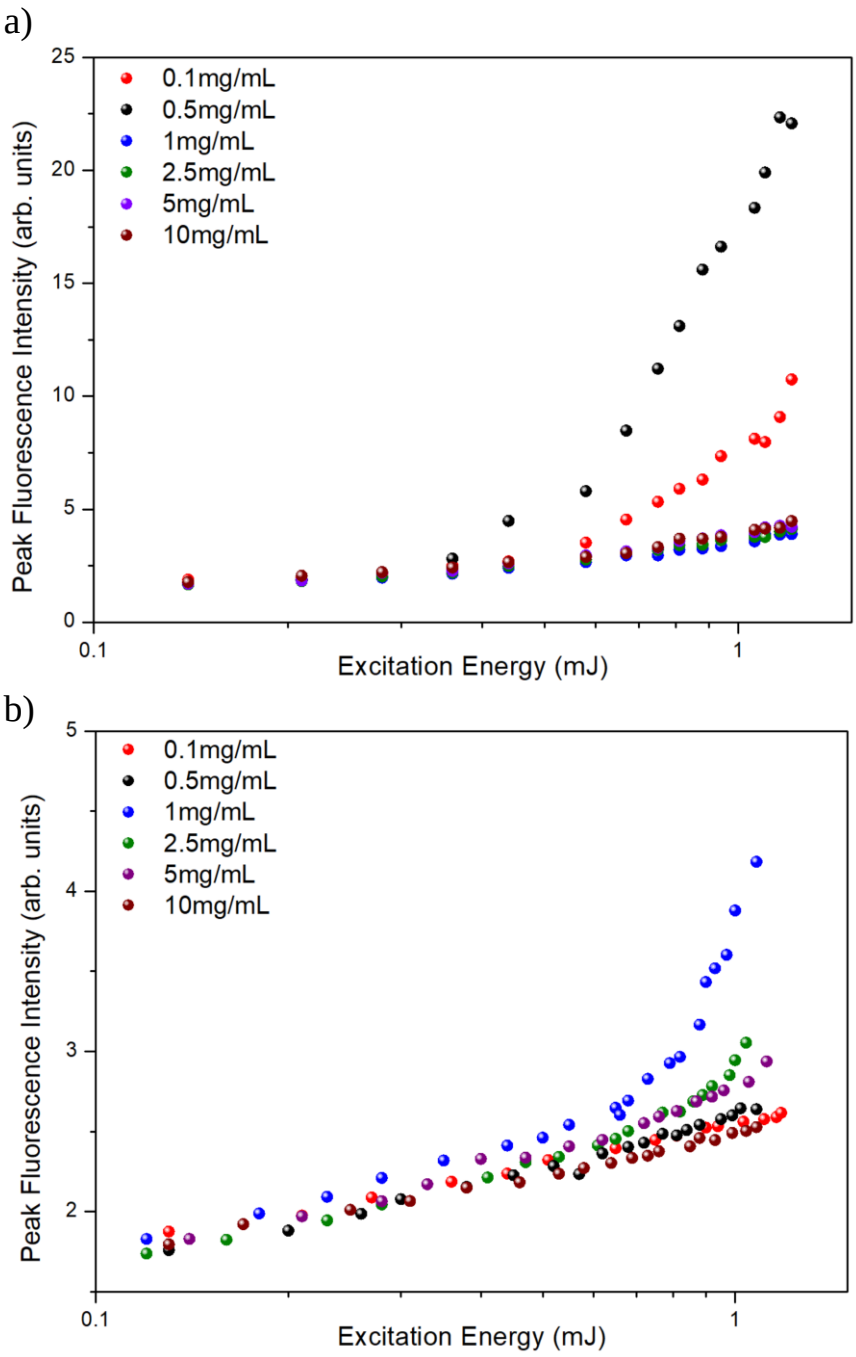

Figure 2-14: Logarithmic RL intensity as a function of the excitation energy for various (a) QtzNP and (b) ASNP concentrations, used to determine the lasing threshold.

Beyond these optimal concentrations, further increases in particle concentration resulted in a rise in the RL threshold, ultimately reducing lasing efficiency. This behavior can be attributed to a decrease in the light scattering mean free path at higher concentrations. When the mean free path becomes too short, the interaction between scattered light and fluorescent dye molecules is insufficient before new scattering events occur, leading to insufficient optical gain to overcome absorption losses.

On the other hand, tests conducted with QtzNP concentrations below 0.5 mg/mL showed reduced lasing intensity, or in some cases, no lasing even at very high excitation energies. At these lower concentrations, scattering events are too widely spaced to provide the necessary feedback for lasing. In such scenarios, absorption phenomena dominate over the optical feedback generated by light scattering, preventing efficient lasing.

Figure 2-15 compares the emission results for the most efficient samples of QtzNP and ASNP, with scatterer concentrations of 0.5 mg/mL and 1.0 mg/mL, respectively. At the same excitation energy, well above the lasing threshold, it is evident that the QtzNP sample exhibits superior efficiency. This is demonstrated by a more pronounced increase in fluorescence intensity and a greater reduction in FWHM (Fig. 2-15 inset) compared to the ASNP sample. These results highlight the superior scattering and feedback properties of the QtzNP samples in comparison to the ASNP samples.

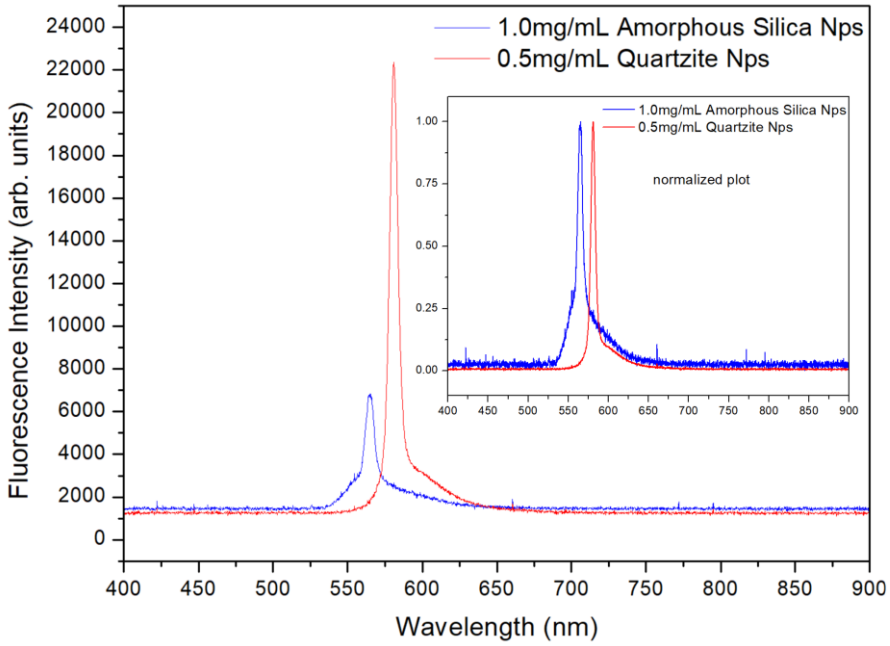

Figure 2-15: Fluorescence intensity as a function of the wavelength, showing higher intensity emission for QtzNP; (inset) normalized emissions comparing reduction in the FHWM and redshift.

To gain a deeper understanding of the emission spectra, the fluorescence peak wavelength was analyzed as a function of scatterer concentration. Figure 2-16

reveals the peak emission wavelength shifts to higher values as the concentration of scatterers increases.

At lower QtzNP concentrations, the dye molecules are more isolated, resulting in an emission wavelength closer to that of pure Rh6G in EG. In this case, the spectrum is dominated by monomer fluorescence. However, as the QtzNP concentration increases, a consistent redshift in the peak emission wavelength is observed. This behavior is consistent with a well-documented phenomenon in Rh6G solutions at high dye concentrations [35], where dimerization of dye molecules causes a spectral shift into the region dominated by aggregate emission.

We suggest that it could arise from two processes: first, an increase in the reabsorption of the fluorescence photons by the Rh6G molecules, due to the decrease in the TMFP associated with the increase in scatterers density; second, an increase in the occurrence to form dimmers on the surface of the scatterers. This assisted dimerization could be explained by the increase in the total SiO2 surface area (due to the increase of the NP concentration), on which Rh6G molecules could be trapped by intermolecular interactions with the SiO2 substrate, increasing the probability to interact by similar mechanism with others Rh6G molecules, resulting in the formation of dimmers. The shift in fluorescence peak wavelength also provides insight into the reduced efficiency of RL samples with higher QtzNP concentrations (Fig. 2-16). This reduction in efficiency could be attributed to dimerization processes, which alter the emission characteristics, or to the overlap between absorbance and emission spectra. Such overlaps diminish the reabsorption of emitted light for excitation energies below the lasing threshold.

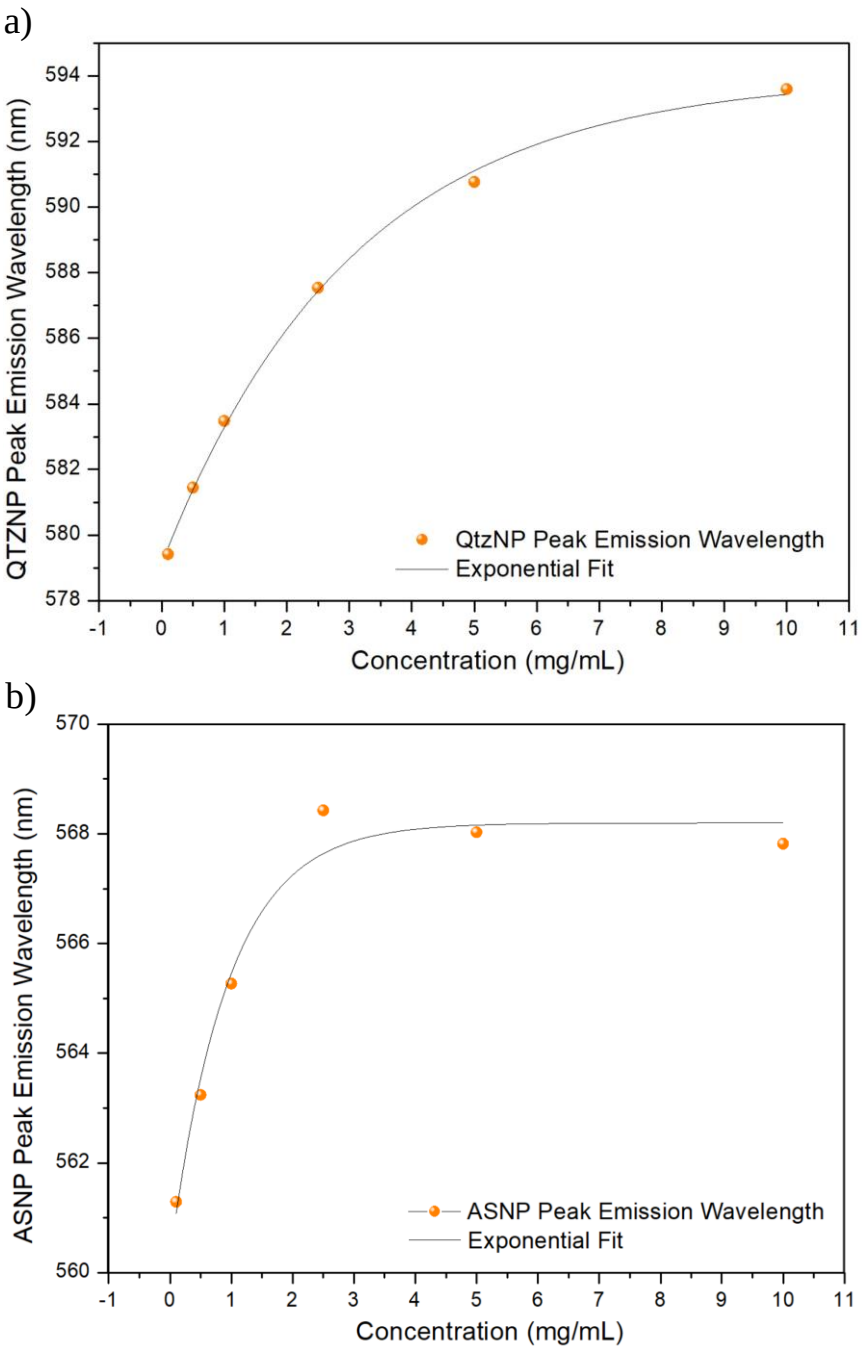

Figure 2-16: P emission wavelength as a function of concentration of (a) QtzNP and (b) ASNP scatterers.

The scattering mean free path (TMFP) for all samples was determined to be equivalent to the transport mean free path, given the isotropic nature of the RL emission. This isotropy was verified by measuring uniform output intensity in all directions, both below and above the lasing threshold. The TMFP was calculated as 500 μm for the most efficient quartzite sample (0.5 mg/mL) and 57 μm for the most efficient ASNP sample (1.0 mg/mL), based on the average particle size. The

scattering cross section was determined using finite element methods and Mie theory, with detailed simulations and discussions provided in the next section.

In the context of disordered media and multiple scattering, as already discussed in section 2.3, the lasing regime can be classified as diffusive, as it satisfies the condition $\lambda < l_t < L$ where λ is the wavelength of scattered light, l_t is the TMFP, and L is the sample size. This classification is further supported by the absence of coherence features, such as narrow spectral peaks with FWHM < 1 nm, which are characteristic of Anderson localization. Anderson localization is associated with spatially localized modes and strong interference effects, occurring when $l_t < \lambda$.

Here I once again highly recommend taking a look at the comparative Table from our published work [2] or Appendix A.2, where we compare the efficacy of our scatterers with recently published work that uses similar materials, considering the composition, phase and morphology.

2.5.4. Finite element method simulations & discussion

To investigate the role of nanoparticle morphology in the observed scattering efficiency, we performed computational simulations of electromagnetic scattering for nanometer-scale objects. These simulations were conducted using the finite element method (FEM) in the COMSOL Multiphysics software [], utilizing the Electromagnetic Waves, Frequency Domain (ewfd) interface.

Figure 2-17 illustrates the simulation results for nanoparticles with identical crystalline phases (chosen through refractive index) but differing morphologies—spherical and prismatic—with a radius of 75 nm. Scattering from perfectly spherical particles of sizes comparable to the incident light's wavelength is well-documented in the literature and can be described by Lorentz-Mie and Rayleigh solutions, depending on particle size [7,36].

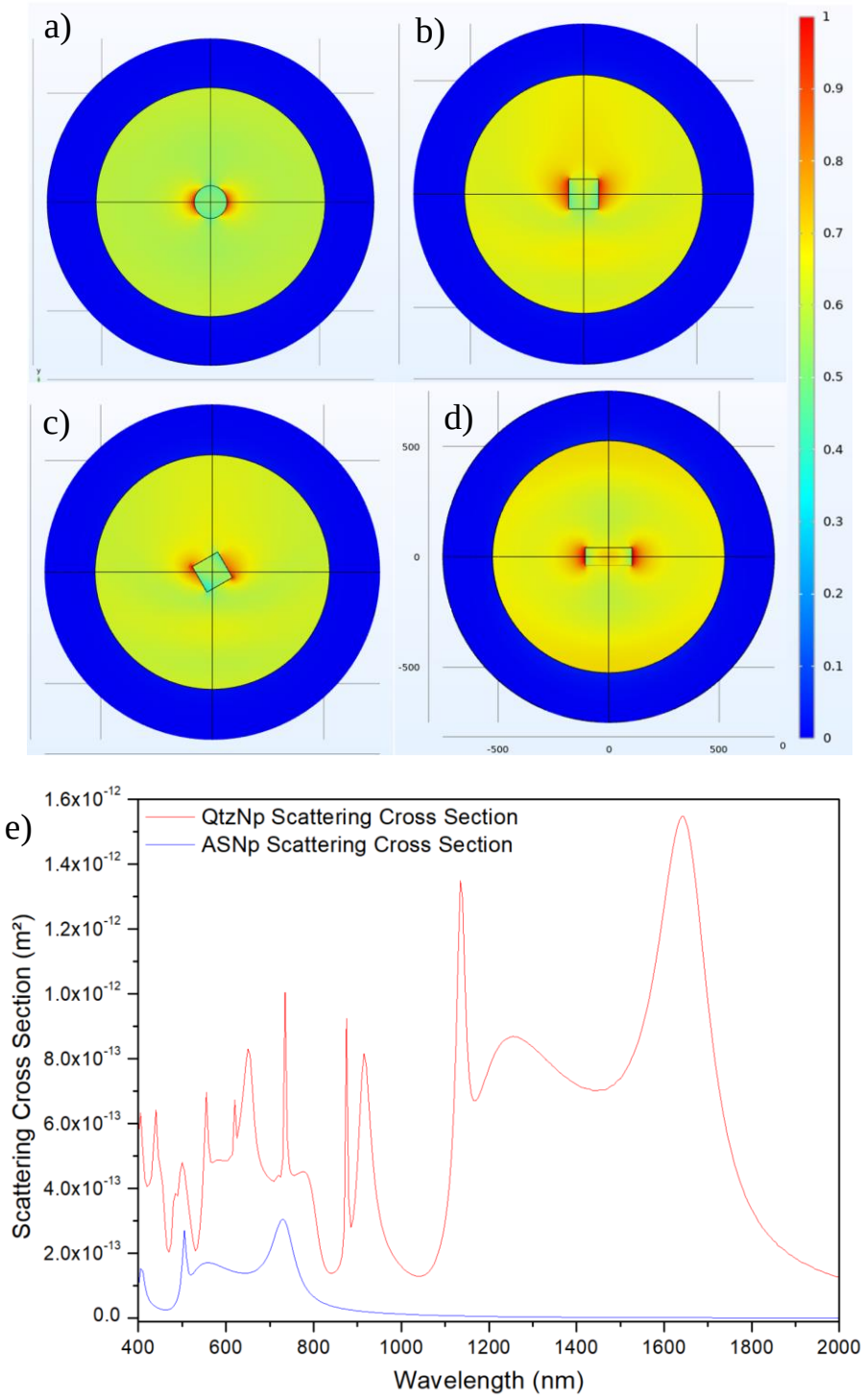

Figure 2-17: (a–d) Normalized scattering patterns of the electric field for different NP morphologies. (e) scattering cross sections of both scatterer phases considering average nanoparticle size.

To analyze the characteristics of the crystalline aggregates in the quartz nanoparticles (QtzNP), simulations were conducted using refractive indices and morphologies representative of sharp-edged, highly reflective nanocrystals (Fig. 2-17b and 2-17c). Two geometries were modeled: spheres and prisms with

dimensions based on microscopy measurements, ensuring that the scattering cross-section and aspect ratio corresponded to experimental observations.

The results demonstrate a significant concentration of the electric field on the faces of the prism perpendicular to the incident field, particularly those aligned with the polarization. These high-field regions are crucial for amplifying the gain of the fluorescent dye, overcoming absorption losses and enhancing the scattering efficiency in the random laser.

A uniform source field with a maximum amplitude of 10 V/m was used in all simulations. The prismatic morphology, characteristic of QtzNP, exhibited higher scattered field intensities and lower losses over longer distances compared to conventional spherical silica particles. This highlights the importance of sharp edges and reflective crystalline faces in increasing random laser efficiency. These features also explain the extended scattering mean free path observed experimentally, enabling lasing at lower scatterer concentrations.

By integrating the scattered power over all boundaries relative to the incident power, we determined the scattering cross-sections for both scatterer phases (Fig. 2-17d) . The molecular organization of QtzNP contributes to stronger electric and magnetic dipole and quadrupole interactions across all considered wavelengths, confirming the superior scattering properties and efficiency of quartzite compared to amorphous silica.

The higher refractive index of quartzite compared to silica nanoparticles further enhances scattering efficiency [22]. While this factor was not simulated in our study, as the background material was modeled as air rather than the fluorescent dye, it is a known contributor to the observed phenomena. Moreover, the quartzite material not only scatters light (in smaller particles) but also reflects it effectively (in micro- and nano-sized aggregates from the grinding process). This increased reflectivity promotes light localization within the gain medium, further boosting random laser efficiency [37].

3 Second harmonic generation & hyper Rayleigh scattering

In this chapter, Hyper Rayleigh Scattering (HRS) technique will be explored as a method for quantifying the efficiency and first hyperpolarizability of non-centrosymmetric crystalline nano- and micromaterials. The materials we characterized here were synthesized by Prof. Lauro J. Q. Maia and his group (Federal University of Goiás, UFG), and the idea to develop this work occurred in a discussion we had at the B-MRS meeting at Maceió, Alagoas, in the end of 2023. Results shown here are planned to be published, as the manuscript is currently under production.

3.1. Non-linear optical phenomena

Nonlinear optics (NLO) emerge when the interaction between high intensity electromagnetic fields and matter results in a non-proportional response of the material [3]. Unlike linear optical phenomena, where properties such as refractive index and absorption coefficient remain constant, nonlinear processes emerge when the induced polarization in a material, its response to the electric field of light, becomes dependent on higher-order terms of the electric field, beyond the first-order approximation.

These nonlinear interactions give rise to fascinating effects such as harmonic generation [38], self-focusing [39], and nonlinear absorption [40], which have become essential tools in modern photonics.

Though often unnoticed, nonlinear optical effects are present in our day-to-day life. For example, colors seen in laser light shows often rely on second-harmonic generation, where infrared light is converted to visible green light in a nonlinear crystal. Similarly, the ultra-short pulses of light used in LASIK (laser-assisted in situ keratomileusis, [41]) eye surgery are made possible by nonlinear processes such as self-phase modulation and chirped pulse amplification. Nonlinear optics also plays a key role in the creation of supercontinuum light sources, which

produce rainbows of colors from a single laser beam and are widely used in fiber optic communications, biomedical imaging, and spectroscopy.

These effects are possible because, under high-intensity illumination, the induced polarization of a material—its response to the electric field of light—contains terms beyond the first-order approximation [3].

Among many nonlinear optical processes, second-order effects hold a unique position due to their relevance in applications ranging from frequency doubling to the characterization of material symmetries. There are different techniques to characterize SHG, among them in this work it is described the Hyper-Rayleigh scattering (HRS) technique.

HRS is a second-order nonlinear optical process, which has become an important technique for probing the first hyperpolarizability (β) of molecules and nanostructures [42]. Unlike conventional second-harmonic generation, which requires phase-matching conditions, HRS occurs in disordered media and isotropic solutions, allowing for the direct assessment of molecular nonlinearities in complex environments.

The quest for highly efficient materials capable of second-harmonic generation lies at the heart of advancements in nonlinear optics. SHG, a parametric second-order nonlinear optical process, involves the conversion of two photons with the same frequency (ω) into a single photon with twice the frequency (2ω).

The search for high SHG efficiency requires materials with specific properties: a non-centrosymmetric crystal structure, strong nonlinear optical coefficients, and good transparency in both the fundamental and harmonic wavelength ranges. Researchers have been exploring materials for that purpose for a few decades now, from traditional inorganic crystals like lithium niobate and potassium titanyl phosphate, to novel organic compounds and emerging 2D materials, which are also central in the following chapter of this dissertation.

The drive for innovation in SHG materials is motivated not only by the need for better performance but also by the demand for more accessible, cost-effective, and environmentally friendly alternatives, which are currently the main purposes of our study in that field.

In the next sections, I provide a concise overview of the fundamental physics governing nonlinear optical phenomena, followed by an explanation of the HRS technique and the corresponding experimental results.

3.2. Nonlinear Polarization and (Centro)Symmetry

Even-order nonlinear optical phenomena, the focus of this chapter, are absent in centrosymmetric materials due to symmetry restrictions in their structural properties. There are several approaches to account for this effect, and we need to look deeper into the nature of the nonlinear polarization response of a material.

The induced polarization P of a material induced by an external electric field E can be expressed as a power series:

$$P = \varepsilon_0\left(\chi^{(1)}E + \chi^{(2)}E^2 + \chi^{(3)}E^3 + \cdots\right)$$

In the above equation, $\chi^{(1)}$ is the first order susceptibility, responsible for linear optical phenomena, such as refraction. $\chi^{(2)}$, the second order nonlinear susceptibility, is responsible for phenomena like SHG (Figure 3-1) and sum-frequency generation. $\chi^{(3)}$ accounts for third harmonic generation, self-focusing, and so on.

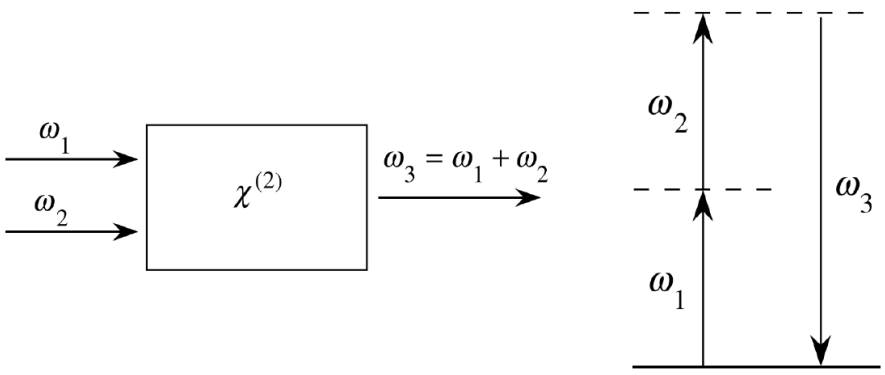

Figure 3-1: Second harmonic generation scheme.

A centrosymmetric material is one that possesses an inversion center, meaning that if you reverse the coordinates of a point (x, y, z → -x, -y, -z), the structure remains identical. Under inversion symmetry, the electric field response E = - E, and because the induced polarization P must also remain consistent under symmetry, the second order nonlinear term $\chi^{(2)}E^2$ would violate this symmetry, appearing unchanged under inversion. As a result, the second order term must be macroscopically zero in centrosymmetric materials to satisfy the inversion symmetry.

Another approach is to consider a symmetric potential and solve the Lorentz force equation. Due to anharmonic effects, the solution must be obtained using standard Rayleigh-Schrödinger perturbation theory. In this framework, it can be shown that, once again, the second-order susceptibility $\chi^{(2)}$ responsible for second harmonic generation, is zero in centrosymmetric materials.

For an in-depth understanding of the subject, I highly recommend Robert W. Boyd's *Nonlinear Optics* book [3], Scully's *Quantum Optics* book [43] and the review-tutorial presented in [44,45], which contains all steps presented here and measurement details.

3.3. Measuring second-harmonic generation

Second order nonlinear optical phenomena are related to the physical property of the material called second order susceptibility ($\chi^{(2)}$), which is dependent on electric field squared. The microscopical analogous of $\chi^{(2)}$ is β, the first hyperpolarizability, often called second order microscopic susceptibility. $\chi^{(2)}$ may be written as a function of β related to the density of the medium (N) and local field corrections in the fundamental frequency (excitation frequency, f(ω)) and the second harmonic frequency (f(2ω)):

$$\chi^2_{ijk} = f^2(\omega)\, f^2(2\omega)\, N\, \beta_{ijk}$$

Several techniques have been developed to quantify optical second-order nonlinearity. Examples include second-harmonic generation (SHG) in Langmuir-Blodgett thin films, the Kurtz powder method, electric field-induced SHG (EFISH), hyper-Rayleigh scattering (HRS), and solvatochromism. In this chapter, we focus specifically on HRS to evaluate the nonlinearity of crystalline materials.

3.4. Hyper-Rayleigh scattering

The Hyper-Rayleigh scattering technique is used to measure the nonlinear optical coefficients of a material under electric field excitation. The intensity emitted from a sample upon illumination from a high intensity electric field, which may be a solution or, in our case, suspension of nano- and microcrystals, is the sum

of the SH generated signals from a number of *i* different sources excited by an incident field of intensity I_ω:

$$I_{HRS} = G \sum_i (N_i F_i < \beta_i^2 >) I_w^2$$

where G is an experimental proportionality constant, N_i is the concentration of the excited material, F_i is a local field factor that depends on the surrounding refractive index and $< \beta_i^2 > = < \beta_{zzz,i}^2 >$ is the value of hyperpolarizability [45].

From the equation above, it is evident that the response depends quadratically on the incident intensity and increases linearly with concentration. The quantitative measurement of the hyperpolarizability β of a sample using the external reference method (ERM) relies entirely on this behavior, as we compare our material to another that properties well established in literature.

By varying the material concentration (N_i) and measuring the corresponding HRS intensity (I_{HRS}) it is possible to obtain the slope α of the I_{HRS} (N_i) curve defined as $\alpha = GF < \beta^2 > I_\omega^2$. The value of the desired hyperpolarizability β is then derived by comparison with the experimental slope measured from a reference solution made of para-nitroaniline (p-NA), a material with a well-known hyperpolarizability. This technique assumes that the parameter G, that depends on the experimental setup, remains unchanged.

In addition to the molecular hyperpolarizability, when the sample consists of a colloidal suspension of nanocrystals in a solvent, the difference in refractive indices between the solvent (denoted by subscript *s*) and the nanomaterial (denoted by subscript *nc*) must be considered. To account for this, an internal field factor T is introduced into the equation:

$$I_{HRS} = G(N_s F_s < \beta_s^2 > + N_{nc} T_{nc} < \beta_{nc}^2 >) I_\omega^2$$

And using the ERM it is possible to determine the molecular hyperpolarizability [45].

3.5. Materials & methods

The crystals investigated here were synthesized as detailed in reference [46], by our collaborators. The original material, referred to as B1 in the source article, underwent degradation over time, resulting in the formation of ammonium dihydrogen phosphate (ADP, [47]). This transformed material, with an uncharacterized crystal size in the literature, demonstrates both stability and the expected high efficiency for second-harmonic generation (SHG). Below is a summary of the synthesis process, along with the hypotheses developed by our colleagues Prof. Felipe T. Martins and Dr. Meiry E. Alvarenga (Federal University of Goiás) regarding the observed changes on the material structure over a long period of time.

The crystals were synthesized using 2-aminopyrazine as the cation, with protonation occurring at the N1 position and dihydrogen as the anion. The nonlinear optical response arises from the dipole interaction between aminopyrazine and phosphoric acid, forming a structure similar to the well-known potassium dihydrogen phosphate (KDP) crystal. This interaction allowed for the observation of SHG in powders composed of microcrystals of the material. The compounds 2-aminopyrimidine, 2-amino-5-chloropyrazine, 2-amino-6-chloropyrazine, pyrazinamide, and 2-hydroxypyrazine were purchased from Sigma-Aldrich® and dissolved at room temperature in a mixture of water (2.5 mL), ethanol (2.5 mL), and inorganic acid (HCl, HBr, or H_2SO_4) while stirring until complete dissolution. The solutions were then left to undergo slow evaporation at room temperature (25°C) for crystallization. After approximately two weeks, colorless crystals of various forms were collected at the bottom of the glass crystallizer.

The material was initially provided as a white powder composed of nano- and microcrystals. Over time, dispersive X-ray measurements revealed that it had transformed into ammonium dihydrogen phosphate (ADP), a well-known crystal recognized for its strong nonlinear optical response and efficiency in second-harmonic generation (SHG).

The hypothesis proposed suggested that the transformation process begins with the degradation of amino pyrazine from the original sample through oxidative mechanisms. This degradation may involve treatments with strong oxidants, such as peroxides or ozone, which target the bonds between nitrogen and carbon atoms

in the pyrazine ring, leading to ring cleavage. During this process, the amine groups ($-NH_2$) present in the amino pyrazine structure could be converted into ammonia (NH_3), a well-documented outcome in the degradation of nitrogen-containing compounds under oxidative or alkaline conditions. Concurrently, a source of phosphate ions, such as phosphoric acid (H_3PO_4) or another phosphate salt, would be required in the system. The released ammonia could then react with the phosphate ions, forming ammonium dihydrogen phosphate ($NH_4H_2PO_4$). This reaction between ammonia and phosphoric acid provides a plausible pathway for the formation of ammonium dihydrogen phosphate.

The transformation of the original crystal into ammonium dihydrogen phosphate (ADP) over time highlights the remarkable stability of the material. Furthermore, this process not only suggests the potential discovery of a novel synthesis route for producing ADP but also reveals a crystal size distribution that has yet to be documented in the literature.

3.5.1. SEM characterization of the Nano- and Microcrystals

To confirm the average size and morphology of the crystals, HRS suspensions were deposited onto aluminum stubs, dried, and coated with a thin gold layer using a sputter coater (Q150T ES Quorum, 40A, 60s). The resulting images, shown in, were captured using a TESCAN Clara (UHR-FEM) electron microscope. Particle size analysis was conducted using ImageJ software (version 1.45s), revealing sizes ranging from hundreds of nanometers to half a millimeter, with an average particle size of 15.94 micrometers.

The slow evaporation crystallization method employed for the sample preparation limits the control over crystal growth in the aqueous solution, leading to a wide variety of crystal sizes and distributions. highlights that some crystals are aggregates of smaller crystallites whose growth was interrupted during the process. The images also reveal significant dispersion in average particle sizes across different clusters, as confirmed by the accompanying histograms.

Energy-dispersive X-ray spectroscopy (EDS) microanalysis confirmed that the crystalline samples primarily consist of carbon, oxygen, nitrogen, and phosphorus, consistent with the expected composition.

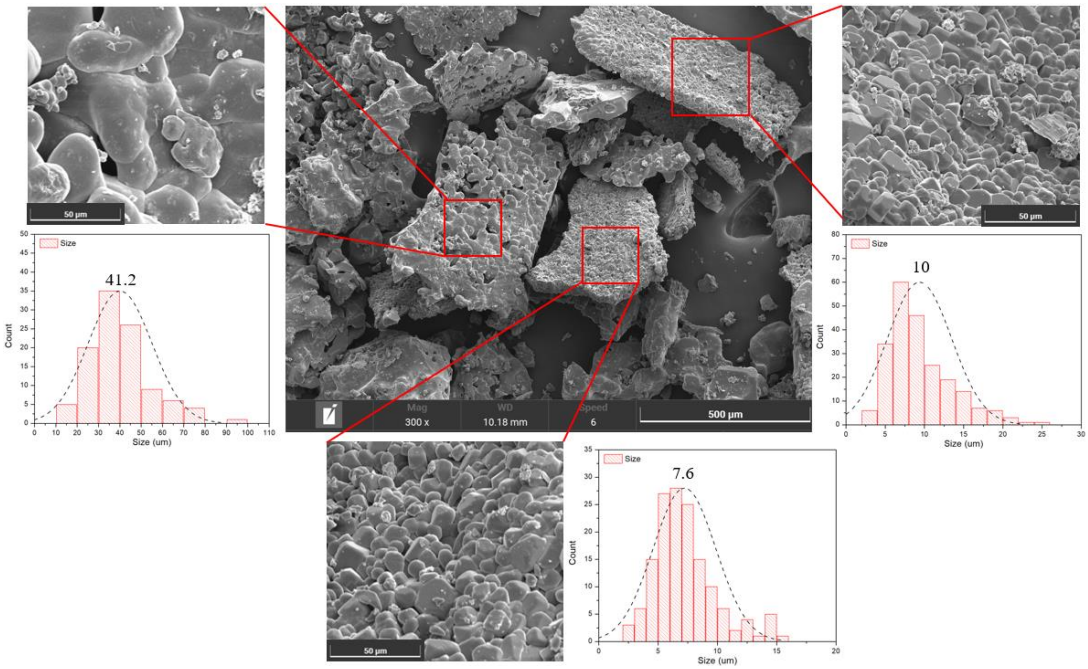

Figure 3-2: UHR-FEM images of the crystal with selected clusters and histograms displaying the average sizes present in different regions of the sample

3.6. Hyper-Rayleigh scattering experimental details

The HRS measurement procedure, as previously described, involves varying the concentration of p-nitroaniline (p-NA, used as a reference solution in methanol) and the target material in suspension under excitation. The Second-Harmonic (SH) signal emitted is recorded to determine the slope, denoted as α.

Once the linear fits for the experimental coefficients α_{pNA} and α_{nc} are obtained, the effective hyperpolarizability, β_{nc}, can be determined using the following equation:

$$\beta_{nc} = \sqrt{\frac{\alpha_{nc} F_{pNA}}{\alpha_{pNA} T_{nc}}} < \beta_{pNA} >$$

where the Lorentz-Lorentz field factor is

$$F_{pNA} = \left(\frac{n_{meth}^2 + 2}{3} \right)^6$$

and the internal field factor can be determined as

$$T_{nc} = \left(\frac{3n_s^2}{2n_s^2 + n_{nc}^2} \right)$$

considering no index dispersion n(ω) ~ n(2ω). The reference value for p-NA hyperpolarizability in methanol is $\beta_{p\text{-}NA}$ = 25.9 x 10^{-30} esu [48-50].

The experimental setup (Figure 3-3) utilizes a frequency-doubled Q-Switched Nd:YAG laser (Quantel Ultra, 6 ns pulse width, operating at 20 Hz) at 1064 nm wavelength. To eliminate unwanted 532 nm radiation from the excitation source, a combination of a dichroic mirror (R 532 nm, T 1064 nm) and an infrared-absorbing filter are employed. The laser beam is then focused through a 200 mm focal length lens into a quartz glass cuvette containing the suspension. The scattered SH signal is collected perpendicular to the excitation beam and directed into a photomultiplier tube (PMT, Hamamatsu E717-21) operating at 1.2 kV, equipped with a colour bandpass filter (Thorlabs BG37) to isolate frequency-doubled radiation. Figure 3-3 below illustrates the experimental setup, detailing each component. The grey box indicates components that are isolated inside of a black box to prevent noise and unwanted radiation from reaching the PMT).

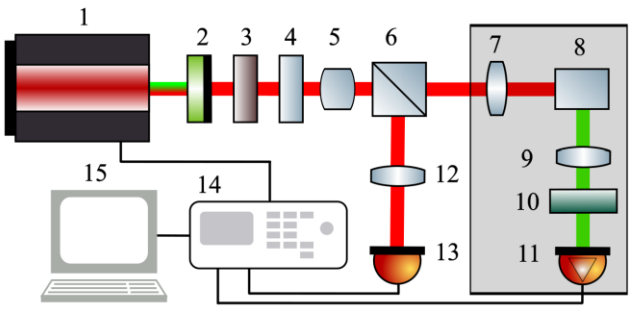

1 Nd:YAG Laser (Quantel Ultra)
2 Dichroic Mirror (Thorlabs HBSY12)
3 Filter (Thorlabs FGB67S)
4 Half-Waveplate (Thorlabs WPH05M)
5 Polarizer (Thorlabs GL15)
6 Beamsplitter
7 Plano-Convex Lens (Thorlabs LA4X)
8 Sample (AD395 / p-NA)
9 Plano-Convex Lens (Thorlabs LA4X)
10 Filter (Thorlabs FGB18)
11 PhotoMultiplier (Hamamatsu E717-21)
12 Plano-Convex Lens (Thorlabs LA4X)
13 Photodetector (Thorlabs PDA100A)
14 Oscilloscope (Tektronix 1GHz MDO)
15 Computer

Figure 3-3: Experimental Setup for the HRS experiment. On the left details of each component.

As part of the material characterization, the photon bandgap energy and diffuse reflectance spectroscopy were also measured by our collaborators at UFG. Diffuse reflectance data were recorded using a PerkinElmer Lambda WB1050 spectrometer, with barium sulphate powder serving as the reference material.

3.7. Results & Discussion

Measurements were conducted using the setup described in the experimental section. Crystalline ADP powder ($NH_4H_2PO_4$) was evenly spread on a microscope slide, excited with the laser source, and the second-harmonic generation (SHG) emission was observed for both transmitted and reflected light.

Figure 3-4 depicts the intensity profiles as a function of pulse duration for both the excitation light (black curve, QS+ML Nd:YAG pulse) and the SHG signal (red curve). As expected, the SHG light generated from the sample exhibits a narrower pulse width, with the ratio of the FWHM of the two signals corresponding to ½ (Δt_{532} = 0.147 ns, Δt_{1064} = 0.192 ns).

Additionally, Figure 3-5 confirms the quadratic dependence of the generated SHG signal on the input intensity and the emitted intensity variation under rotating polarization for the excitation light. This behavior is demonstrated by the logarithmic plot, where the slope $\alpha_{\log(2\omega)}/\alpha_{\log(\omega)}$ is approximately 1.96, consistent with the expected value of 2 for the second-order effects.

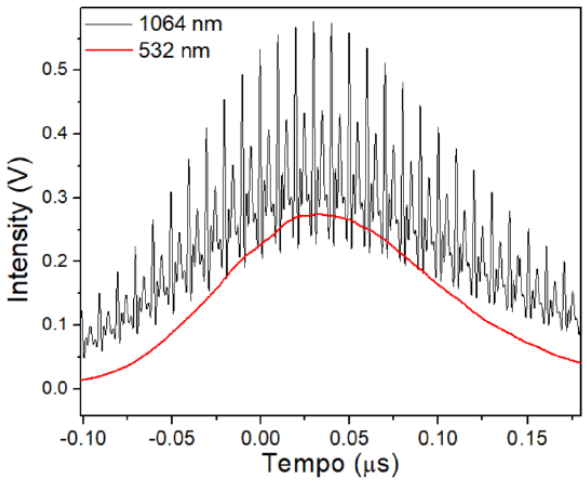

$\Delta t_{532} = 0{,}147\ \mu s$

$\Delta t_{1064} = 0{,}192\ \mu s$

Figure 3-4: Intensity as a function of pulse time for both excitation and SHG signal.

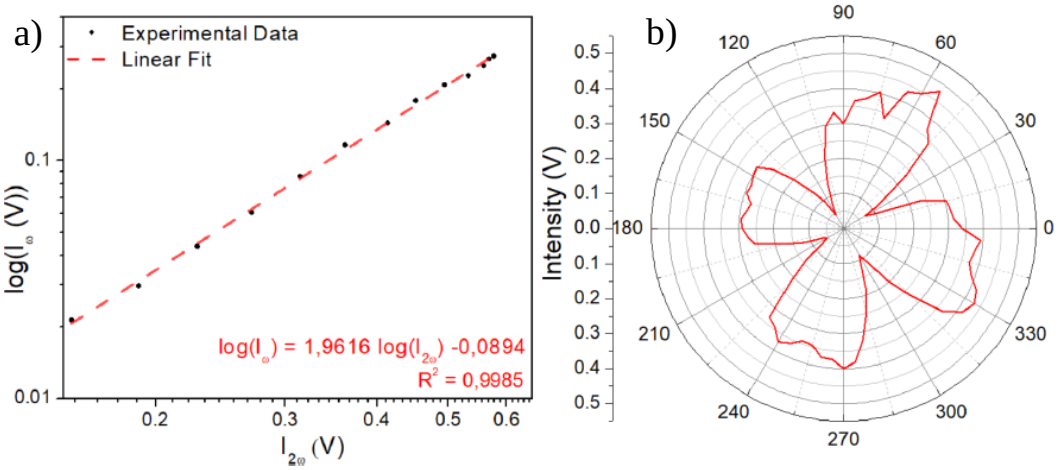

Figure 3-5: (a) Logarithmic plot of the input intensity as a function of the output, highlighting the expected quadractic behaviour and (b) excitation light polarization dependence.

Figures 3-6 illustrate the expected linear dependence of the HRS intensity on the concentration of nanocrystals and p-NA, respectively. This linear relationship confirms that the signal detected by the PMT at 532 nm arises from the Hyper-Rayleigh Scattering of individual nanocrystals in suspension, with negligible aggregation observed across all concentration values.

The slopes, α_{NC} and $\alpha_{p\text{-}NA}$, obtained by linear fitting of the HRS intensity versus concentration for the nanocrystals and the reference material, respectively, were substituted into Equation (6), incorporating the Lorentz and internal field factors [48]. From this analysis, the effective hyperpolarizability of the nanocrystals was determined to be $\langle\beta_{nc}\rangle = 3.38 \times 10^{-22}$ esu per nanocrystal

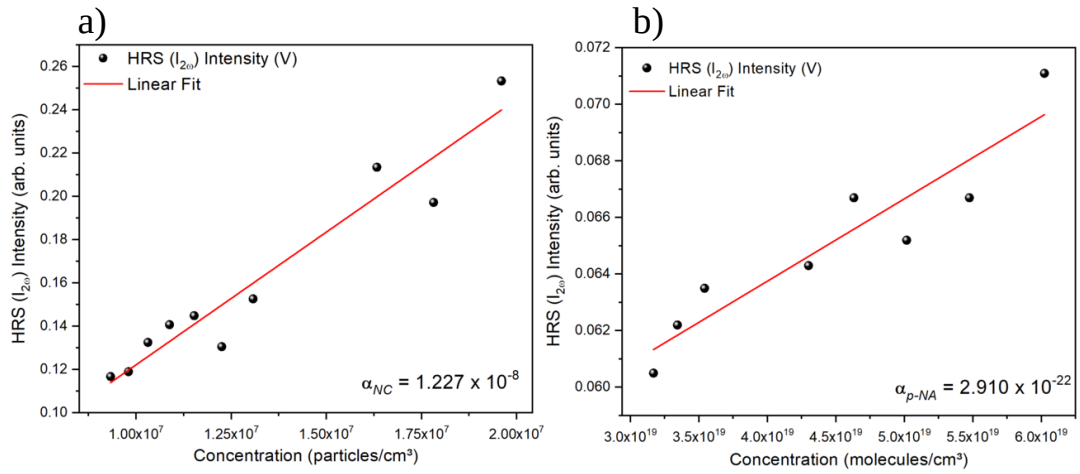

Figure 3-6: HRS intensity as a function of concentration for (a) ADP microcrystals and (b) paranitroaniline in methanol. The red line in each plot corresponds to the linear fit and the inset text shows the slope for each sample.

Absorption data from the nanocrystals in suspension were analyzed to determine their optical band gap using the Tauc relation [51,52]

$$\frac{F(R) = \left[A\left(hv - E_g\right)^m\right]}{hv}$$

where A is a proportionality constant, hv is the photon energy, E_g is the optical band gap and m = ½ or m = 2 for indirect or direct transitions, respectively, and last $F(R)$ is the Kubelka-Munk function. The optical band gap, $E_g = 3.85\ eV$, was then calculated by extrapolating the linear portion of the $[F(R)hv]^2$ versus hv plot to zero, as can be seen in figure 3-7 below together with information for SiO_2 which is used as a reference.

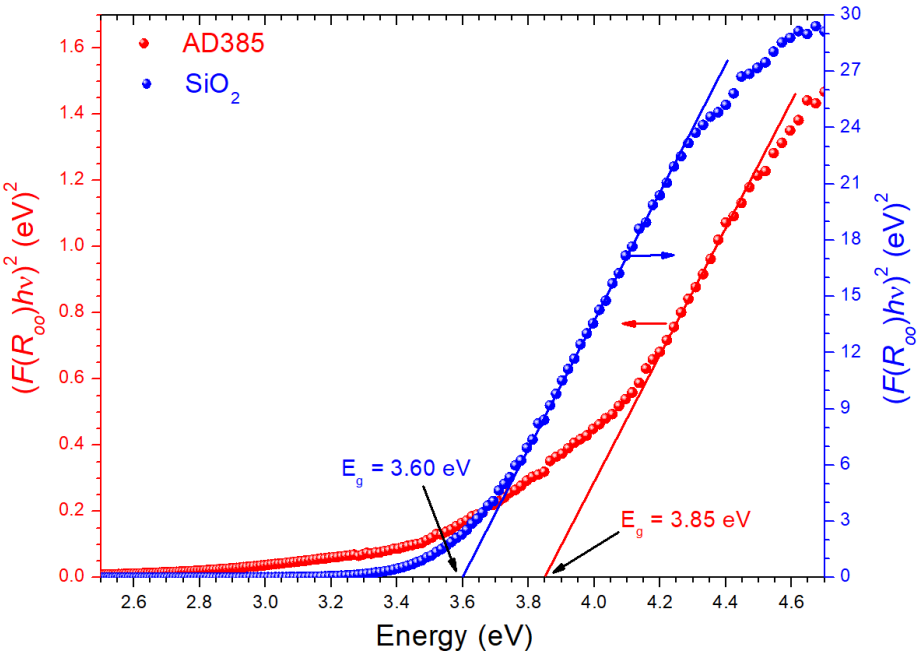

Figure 3-7: (a) Photon band gap determination through Kubelka-Munk method for our sample (red) and SiO_2 nanoparticles (blue) as a reference.

To facilitate comparison with previously studied and commercial materials, the hyperpolarizability of our crystals is presented alongside published results in Table 1. Notably, the unit cells of our crystals have larger average volumes than those reported in most prior studies, which correlates with enhanced efficiency.

Table 3: Comparison between ADP produced in our work and previously studies.

Material	**< βcrystal > (esu)**	**Diameter**
ADP	3.38×10^{-22}	15.94 µm
$NaNbO_3$	6.30×10^{-24}	109 nm
$LiNbO_3$	1.63×10^{-23}	125 nm
$KNbO_3$	1.218×10^{-23}	128 nm
KTP	3.35×10^{-23}	237 nm
$BaTiO_3$	15.16×10^{-24}	91 nm

4 Electric field influence on the stability of 2D materials

In this chapter we investigate the influence of the electric field on the stability of Layered Transition Metal Dichalcogenides (LTMDs) [53,54] produced through redox exfoliation [55,56] by our collaborators Dr Richard Vaia (Air Force Research Laboratory, AFRL) and Dr Nikolaos Chalmpes (Cornell University). The original intent of this work was to investigate the LTMDs material response to an external field for potential applications in nanodevices such as in LIDAR (light detection and ranging) technology. It is well known that 2D materials offer very fast response to external stimuli such as electric fields, and we were counting on fast refractive index response for beam steering applications. In the presence of an applied voltage, the material underwent degradation, a novel and unexpected outcome that motivated us to investigate in depth. Work reported here is published in the Journal of Physical Chemistry C, 129, 5, 2582–2589 [97].

4.1. 2D transition metal dichalcogenides

Two-dimensional transition metal dichalcogenides (TMDs or TMDCs) are a remarkable class of materials of the form MX_2, with M being a transition-metal atom (Mo, W, Nb, etc.) between two X chalcogen (S, Se or Te) layers [54]. Those materials offer unique properties that make them ideal for studying novel physical phenomena and developing advanced technologies, with applications spanning from nanoelectronics and nanophotonics to nanoscale sensing and actuation, driven by their tunable electronic, optical, and mechanical characteristics. In recent years, interest in TMDs has surged, fueled by milestones such as the development of the first transistor and the discovery of strong photoluminescence in monolayer MoS_2.

TMDs history dates back to 1923, when Linus Pauling first determined their structure [57]. By the late 1960s, over 60 TMD compounds were identified, with around 40 of them exhibiting layered structures [58]. Early advancements included the production of ultrathin MoS_2 layers in the 1960s by Robert Frindt [59] and the first monolayer MoS_2 suspensions in 1986 [60]. Parallel efforts, inspired by the rise

of carbon nanotubes and fullerenes in the 1990s [61], led to the synthesis of WS_2 and MoS_2 nanotubes and nanoparticles.

The resurgence of interest in TMDs was further accelerated by the intense growth of 2D and graphene-related research in 2004, which refined techniques for working with layered materials [62]. This progress enabled new studies on TMDs and their ultrathin films, revealing extraordinary properties that differ significantly from their bulk counterparts.

What sets TMDs apart from other layered nanomaterials is their versatility. Depending on the combination of transition metal and chalcogen atoms, these materials exhibit a wide range of electronic properties, from metallic (e.g., TaS_2) to semiconducting (e.g., MoS_2 and WS_2) to superconducting (e.g., $NbSe_2$) [54]. Additionally, their reduced dimensionality amplifies quantum confinement effects and spin-orbit coupling, enabling phenomena such as valley polarization and the spin-valley Hall effect, which are absent in bulk materials.

In this chapter, the primary focus will be on molybdenum disulfide (MoS_2), as of now the most extensively studied transition metal dichalcogenides due to its optical and electronic properties [63]. While other TMDs were also explored during the course of this research, including their responses to varying external fields, MoS_2 stood out as a model system for detailed analysis. Furthermore, the study includes an investigation into the electric field-induced degradation of these materials, which is critical for understanding their stability and reliability in practical emerging applications such as electronic and electro-optical components. The findings on MoS_2 provide a foundation for broader insights into the behavior of TMDs. This chapter thus integrates a focused examination of MoS_2 with a broader perspective on TMD degradation under the presence of external electric fields.

4.2. TMDs material synthesis

As already mentioned, the material was provided by our collaborators from the Air Force Research Laboratory, who developed the manufacturing process of redox exfoliation. Compared to other chemical methods, this approach is more energy-efficient, operates under straightforward environmental conditions,

employs eco-friendly solvents, and produces samples with a tunable defect density in large scale.

Two widely used techniques for producing 2D materials are the bottom-up approach, which involves growing thin crystals with one or a few layers, and the top-down approach, which includes methods such as redox exfoliation. The latter was employed in this study to separate bulk MoS_2 crystals into individual layers. The methodology used to prepare the samples examined here has been comprehensively detailed in earlier work by Jawaid et al. [55,56].

In this process, bulk MoS_2 powders were treated with a mild oxidant, cumene hydroperoxide, to generate solution-soluble molecular metal oxide precursors (MOPs) that established a solution-surface equilibrium with the MoS_2. Adding a reductant initiated the condensation and assembly of MOPs into highly charged polyoxometalates (POMs). These POMs strongly adsorbed onto the MoS_2 surfaces, creating significant Coulombic repulsion that facilitated the delamination of the material [64]. This delamination exposed fresh surfaces, allowing further adsorption, assembly, and exfoliation events to occur repeatedly until the MOP precursors and active POMs were exhausted. In this study, polyoxometalates (POMs) served as capping agents, facilitating the high-yield exfoliation of monolayer TMDs while effectively maintaining the separation of flakes through Coulombic repulsion.

For the suspensions, acetonitrile (ACN) was chosen as the reaction medium for its stability in redox environments, its capacity for anhydrous preparation, and its excellent solvating properties for MOPs, POMs, and the delaminated layered transition metal dichalcogenides generated throughout the exfoliation process. This method resulted in the successful preparation of MoS_2 suspensions that are composed of mono- and few layer MoS_2 separated by POMs suitable for further characterization and analysis.

All work hereby reported focuses on Group VI LTMD suspensions. When these semiconductors are reduced to monolayer thickness, their band structure transitions from an indirect to a direct bandgap. This change is accompanied by the emergence of distinct exciton peaks in the optical absorption spectra, which serve as a key identifier for the monolayer state. Notably, agglomeration of the sample disrupts its monolayer character, resulting in the suppression of these excitonic

absorption peaks. This behavior provides a straightforward method for optical identification of monolayer MoS_2 in the prepared suspensions.

4.3. Material characterization

4.3.1. Optical absorption with external electric field

The absorption properties of LTMDs were analyzed using a white light source (ThorLabs SLS201L) and a spectrometer (Ocean Optics USB4000). The samples were contained in a in-house built 1 mm path cuvette, which featured an outer conductive parallel faces made from soda-lime glass slides coated with Indium Tin Oxide (ITO), which are soldered to a high voltage wire (At/001-13, ins. Pead Ø 3,40mm ± 0,03 with PVC external coating). After a few tests, I designed a 3D printed case in which we can position the glass slides in order to guarantee the faces were parallel and enhanced reproducibility. Here I need to acknowledge my ex-colleagues Dr. Leonardo F. Araujo and Dr. Gabriela A. Prando who helped me develop the custom-built cuvette and worked hard on it with me for a long time.

This design enabled the application of an external voltage ranging from 0 to 15 kV at a frequency of 60 Hz to the sample within the cuvette. The applied voltage was continuously monitored using a multimeter (Minipa ET2042E) connected through a high-voltage probe (Fluke 80K-40) in parallel with the cuvette. To prevent electrical breakdown, the entire cuvette was immersed in transformer oil (G Hyvolt II N Naphthenic Oil). The experimental setup used for these measurements is illustrated in Figure 4-1 below.

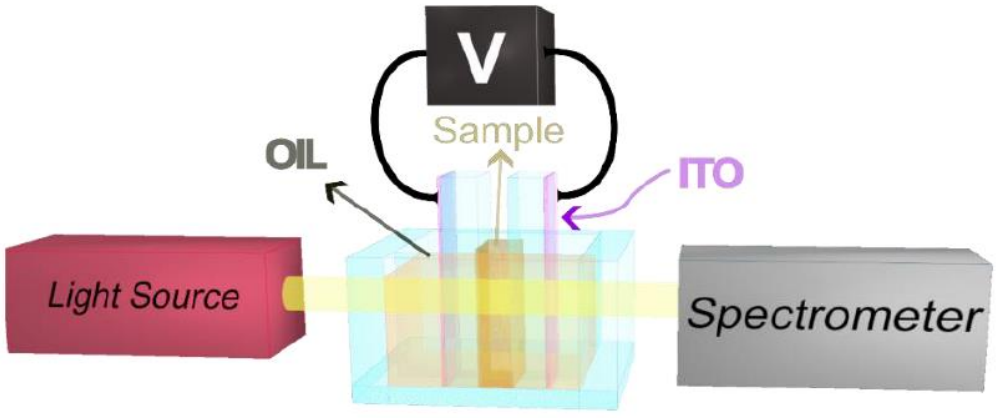

Figure 4-1: Experimental setup scheme with the homebuilt cuvette.

Finite element method two-dimensional simulations were performed to estimate the effective electric field applied to the ACN-MoS_2 suspension within the cuvette (Figure 4-2). The simulations were carried out using the electrostatics interface in COMSOL Multiphysics (es.), which solves Gauss's law by employing the scalar electric potential as the dependent variable. For an applied potential of 2 kV, the calculated electric field strength was 0.185 V/μm. The significant reduction (>10x) of the applied field strength in the presence of the ACN-MoS_2 sample is attributed to the high relative dielectric constant of the ACN solvent, which is 35.09. Figure 4-3 shows the expected linear dependence between the electric field and the voltage applied to the cuvette's electrodes and the dimensions used for the simulation, which are identical to the experimental setup where the cuvette has an optical path of 1.1mm

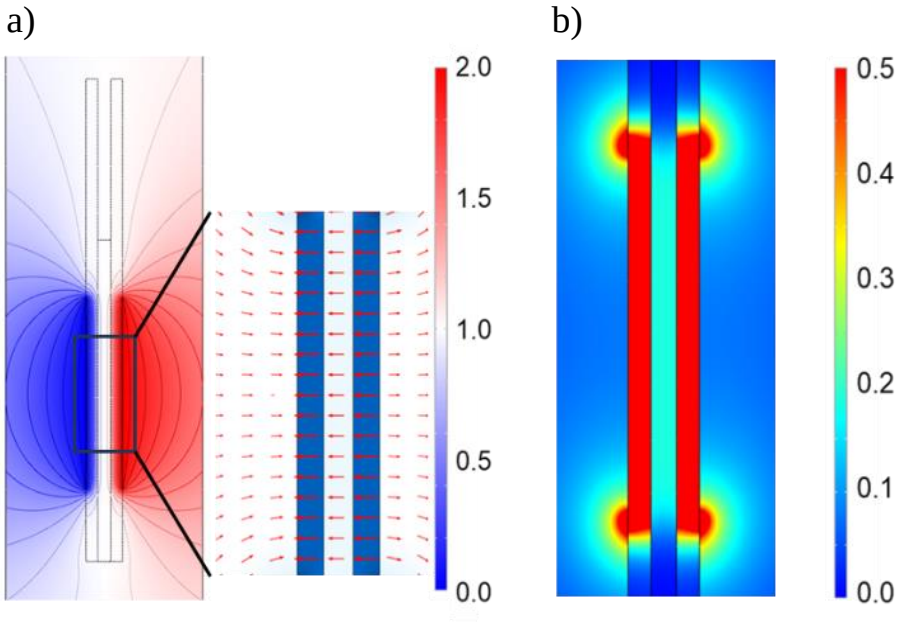

Figure 4-2: (a) Electric potential (kV) applied to the cuvette outer walls and field lines; (b) electric field norm (V/μm).

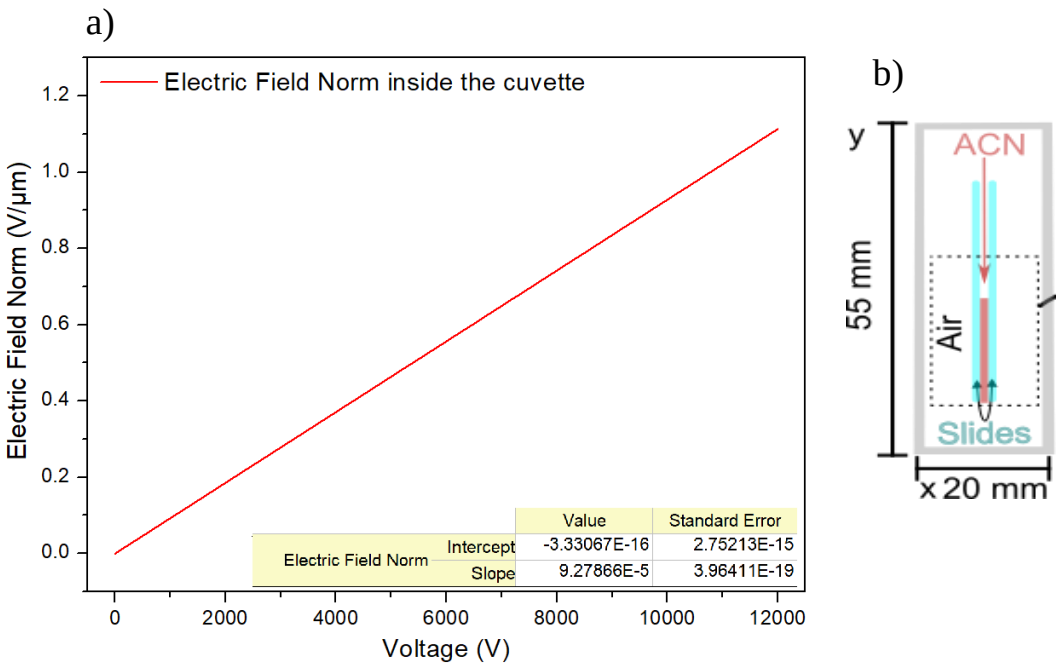

Figure 4-3: (a) Linear dependence between the electric field and the voltage applied and (b) diumensions of the cuvette.

4.3.2. Characterization techniques

Besides real time measurements with external electric field application, the optical absorption of the LTMD samples was measured both before and after the application of voltage using a PerkinElmer LAMBDA 950 UV/Vis/NIR spectrophotometer. This instrument covers an extensive wavelength range of 175–3500 nm with a resolution of 0.2 nm for the range under consideration. Reference-based measurements were conducted using synthetic Hellma Analytics high-performance quartz glass cuvettes with optical paths of 1 mm. These cuvettes provide >75% transmittance for wavelengths above 180 nm, with transmission peaking at 90% in the 190–3500 nm range.

Raman spectroscopy was performed on a dry drop-cast sample prepared on a microscope slide substrate, both before and after voltage application. Data acquisition was carried out using an XploRA PLUS Horiba Jobin-Yvon micro-Raman spectrometer, equipped with a 532 nm laser for excitation. The measurements were taken with a 2400-grade grating, a 100× objective lens, a 200 µm slit, and a laser intensity of 1.25 mW.

Cyclic voltammetry measurements were performed using a Multi Auto-Lab/M101 potentiostat/galvanostat, controlled via NOVA 2.0 software. A three-

electrode cell configuration was employed, consisting of graphite as the working electrode, platinum as the counter electrode, and Ag/AgCl (KCl saturated) as the reference electrode. All measurements were conducted in an acetonitrile solution containing tetrabutylammonium chloride (0.1 mol/L) as the electrolyte. The cyclic voltammetry scans covered a potential range of 0.6 to -0.6 V, in both cathodic and anodic directions, with scan rates varying from 20 to 150 mV/s.

4.4. Results & Discussion

The absorption spectra of an acetonitrile suspension containing layered MoS_2 (ACN-MoS_2) are presented in Fig. 4-4. The sample demonstrated stability over several months, with no observable changes in its absorption spectra, suggesting the absence of precipitation or destabilization of the POM species prior to voltage application. As shown in Fig. 4-4b, the absorption spectrum exhibits peaks corresponding to excitons A and B at 680 nm and 620 nm, respectively, indicating a significant concentration of monolayer (ML) sheets [65] in suspension. The absorbance in the lower spectral region is attributed to the POM species, which can be identified as a mixed-valence system of Mo^{4+} and Mo^{5+} [66]

The stability of the material is ensured by the anionic POMs generated during the liquid exfoliation process. These POMs adsorb onto the TMD surface and create a separation layer through Coulombic repulsion due to their capacity to accommodate significant charge. Transition metals, including molybdenum, are known to form anionic POMs that exhibit strong absorption in the UV region [55]. As shown in the UV-Vis spectra of the ACN-MoS_2 suspension in Fig. 4-4a, the absorption bands below 250 nm are characteristic of anionic Mo-POMs. Additionally, the absorption associated with the bandgap of MoS_2 is observed above 500 nm, while the distinct A and B exciton peaks appear in the 600–700 nm range.

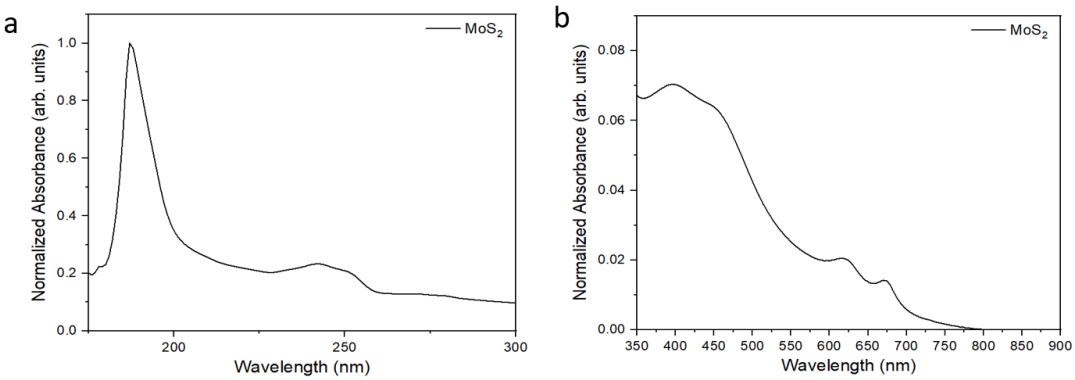

Figure 4-4: Absorption spectra of ACN-MoS_2 sample in the (a) UV and (b) visible region of the spectra.

The absorption spectrum of the LTMDs received is exactly the same as previously published work from our colleagues, which further demonstrates the stability of the sample. To study the stability of the material under increasing electric fields, the cuvette with conductive external faces was used, as described in the previous section.

The normalized absorption spectra of ACN-MoS_2 suspensions were measured after applying an electric field of 0.185 V/µm (Fig. 4-5) for 20 minutes. The spectra were recorded both immediately following field application and after several hours of incubation, with no significant differences observed. A notable increase in an absorption peak at 199 nm was detected in all field-exposed samples, along with a reduction of the lower UV peak (Fig. 4-5a). Prolonged exposure to the electric field further reduced absorption at 190 nm while enhancing the peak at 199 nm, a redshift behavior consistent with thermal degradation patterns reported for Mo-based materials [66]. This was accompanied by the bleaching of a peak at 235 nm, the emergence of a new absorption peak at 225 nm, and a pronounced decrease in exciton peaks at approximately 620 and 675 nm in the visible spectrum (Fig. 4-5b).

The disappearance of exciton peaks is attributed to the agglomeration of the 2D material at the bottom of the cuvette. As the MoS_2 clumps settled out of the optical path, they caused a sharp decline in measurable absorbance. This hypothesis is supported by the visual transformation of the sample: initially a uniform light brown suspension, it became a much clearer liquid with visible clumps of TMDs, as shown in Fig. 4-4d. This change significantly affected light transmission, as the incident light passed through the clearer solvent with minimal interaction with the agglomerated TMDs.

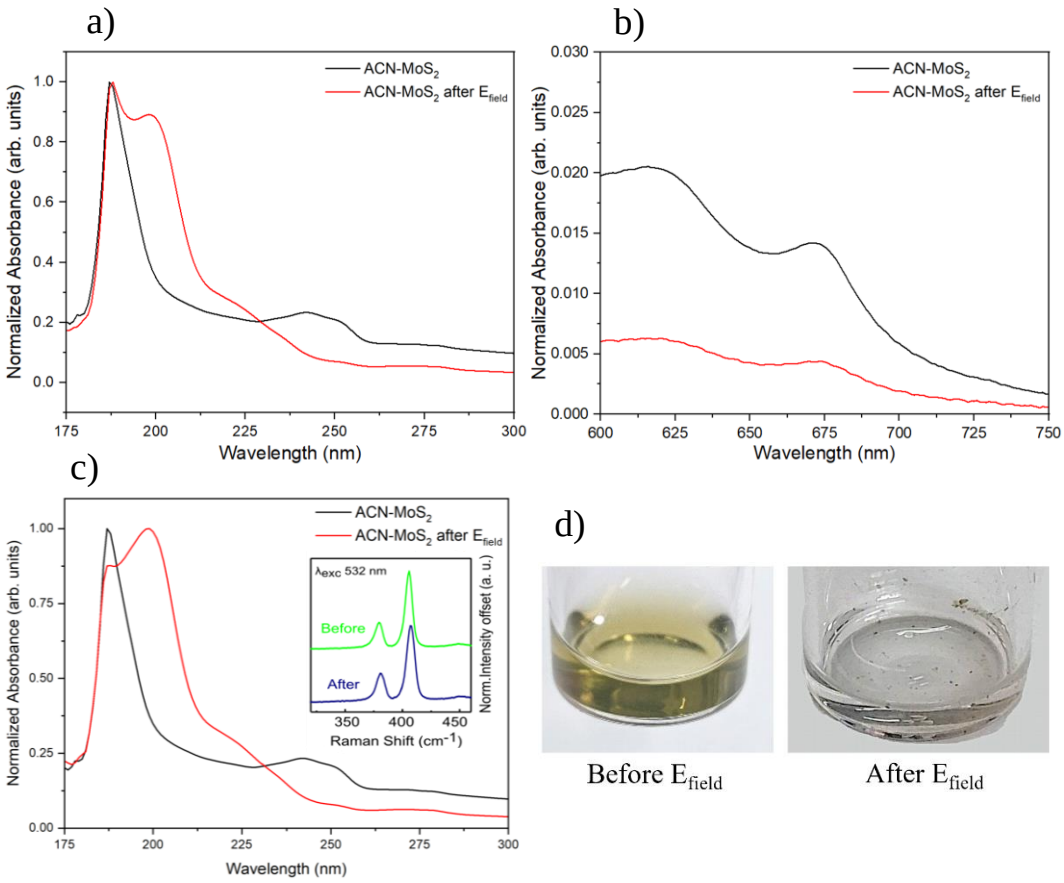

Figure 4-5: Absorption spectra of ACN-MoS_2 sample before and after EField application in the (a,c) UV and (b) visible region of the spectra; the inset in (c) presents Raman spectroscopy results of the black spots for both samples; (d) photograph of the suspension showing aggregation of the monolayers.

The working hypothesis is that the changes in the UV portion of the spectrum are linked to alterations in the oxidation state of the POMs, triggered by a redox process under the applied field. This redox activity compromised the stability of the suspension, leading to the agglomeration of MoS_2 into dense, dark clumps. To confirm that these clumps were composed of MoS_2, Raman spectroscopy was performed (inset Fig. 4-5c inset) on the agglomerates and compared to a dried drop of the uniform suspension prior to field application. Both samples exhibited the characteristic MoS_2 phonon modes at ~380 cm^{-1} and ~410 cm^{-1}, corroborating the identity of the clumps as agglomerated MoS_2 [67]. Figure 4-6 below shows the optical microscopy images of the samples before and after applied field, further confirming the agglomeration of the MoS_2 sheets.

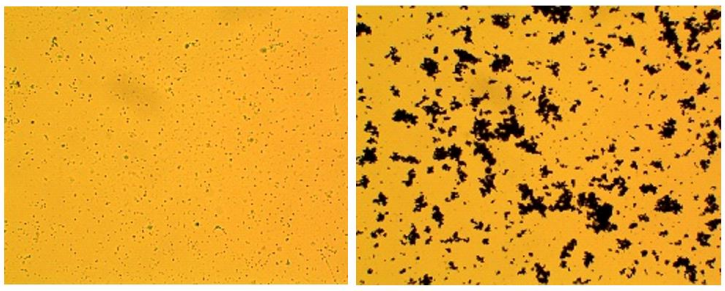

Figure 4-6: optical microscopy images of the suspension showing aggregation of the monolayers after destabilization of the POM due to Efield application.

The application of high voltage to the ITO-coated outer walls of the cuvette charges the capacitor formed by the electrodes, thereby also charging the inner walls. It is plausible that the surface charge in contact with the POM layer alters its charge state via oxidation/reduction of the Mo cations. This interaction impacts the UV absorption peaks and diminishes the POM's ability to stabilize the TMD layers through Coulombic repulsion, leading to agglomeration.

The destabilization of ACN-MoS_2 suspensions under the applied field was observed using the cuvette setup already described. Additionally, destabilization occurred even in the absence of an applied field with other lower stability suspensions when deposited on untreated borosilicate microscope slides. Upon depositing a few drops of the suspension onto pristine borosilicate glass, the hydrophilic nature of the glass caused the drops to spread due to a small contact angle (~20°). Within seconds, the suspension broke into clumps with a black, wrinkled texture, as shown in Fig. 4-5a. UV absorption measurements of this sample revealed significant depletion of the lowest UV peak and the emergence of a peak around 200 nm (Fig. 4-5b), consistent with previous observations for samples exposed to strong electric fields (Fig. 4-5a-c). However, the smaller peaks exhibited a behavior distinct from that observed under field exposure, suggesting an effect not yet fully understood.

It was hypothesized that surface charges on the borosilicate glass could induce oxidation-state changes in the POMs, similar to those caused by an applied electric field. After investigation and multiple tries to mitigate this effect, the glass slides were treated to render their surfaces highly hydrophobic by spray-coating them with tetrafluoropropane (TFP, Zeiss Anti-Fog). This treatment increased the contact angle, preventing the suspension from spreading and preserving its stability

over time, as shown in Fig. 5a-d. Unlike untreated glass, samples on TFP-treated surfaces showed no noticeable transformation over time and evaporated without agglomeration. UV absorption spectra of samples on hydrophobic glass surfaces revealed no depletion of the 189 nm absorption peak or increase at 199 nm, suggesting that when surface charges are neutralized or minimized, the POM valence state remains unchanged.

To further test this hypothesis, higher stability samples of ACN-MoS_2 suspensions were placed in two cuvettes with TFP-treated internal surfaces and subjected to the same experimental conditions, including an external field of up to 6 MV/m. In these cases, no material degradation or agglomeration was observed, mirroring the behavior of the treated glass slides (Fig. 4.5). While these experimental results are not conclusive, they suggest that TFP molecules on the treated glass surface prevent MoS_2 adsorption, likely due to their hydrophobic nature. This may reduce electron transfer rates, preserving the POM's stability and prevent degradation, even under high applied fields.

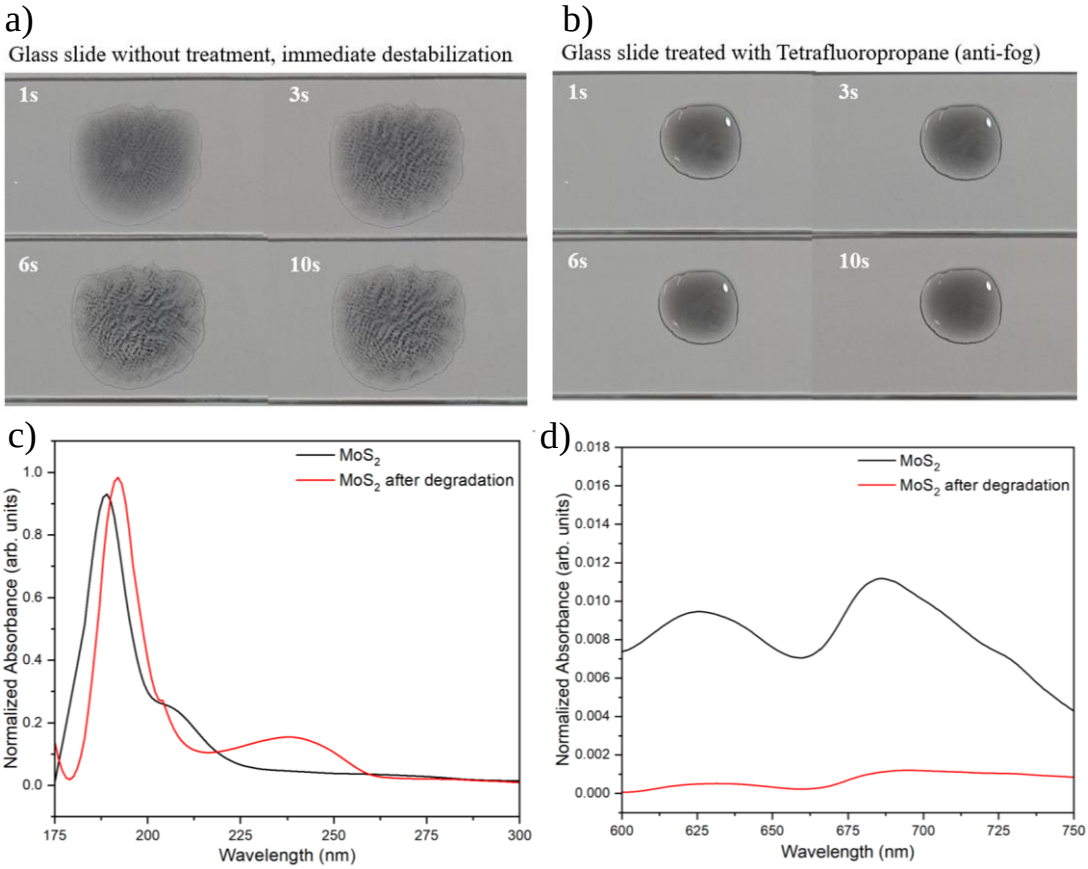

Figure 4-7: (a) Pristine glass slides show agglomeration of the ACN-MoS_2 suspension at 4 time periods (1s, 3s, 6s and 10s). (b) Glass Treatment with Tetrafluoropropane maintains stability of sample. (c) UV absorption spectra of ACN-MoS_2 sample before and after degradation due to contact with untreated glass

slide. (d) Absorption spectrum in the visible, showing that the exciton absorption peaks appear weakened.

In order to ensure which electrochemical process is happening in our sample and the chemical stability of the material, cyclic voltammetry measurements were conducted (Figure 4-8), by our collaborator Dr. Daniel Grasseschi (Federal University of Rio de Janeiro). Cyclic voltammetry is a technique that involves modulating the electric potential between two electrodes, facilitating electron exchange between electrochemically active species and the electrode surface. This method provides insights into various aspects of electrochemical reactions, including the number of electrons involved, the reversibility of redox processes, reaction kinetics, mass transport mechanisms, and the influence of surface morphology, among others.

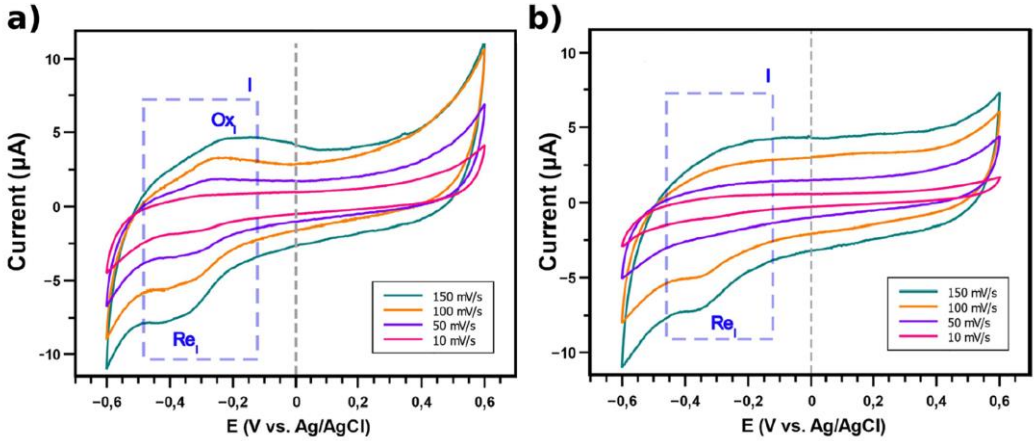

Figure 4-8: Cyclic voltammetry results of two batches (a and b) of ACN-MoS2, both prepared under identical experimental conditions, comparing scan rates of 150, 100, 50, 20, and 10 mV s−1.

For an electrochemical process to occur, a conductive medium is essential to enable electron transfer. In our case, tetra-n-butylammonium chloride, a non-electrochemically active species, was used as the supporting electrolyte in acetonitrile. Two samples' batches, with varying stability processes, were analyzed with the cyclic voltametric technique. Results obtained showed the expected agglomeration under different voltages, further confirming results obtained with the custom-made cuvette and absorption measurements.

From the beginning of my work with redox-exfoliated 2D material characterization a few years ago, I observed significant variations in the visual stability of the batches we received. Some batches presented perfectly uniform suspensions, while others showed noticeable clumps of material settling at the

bottom of the flask. On numerous occasions, we were advised by collaborators to use only the supernatant to ensure uniform suspensions for experimentation. The findings presented in this work not only demonstrate how easily the stability of these samples can be compromised by external factors, such as applied electric fields or untreated surfaces of containers but also offer practical strategies to preserve the stability of these suspensions over longer periods. These insights aim to mitigate the challenges associated with sample preparation and handling, ultimately enhancing reproducibility and reliability in future studies.

5 Material optimization with Multi-Objective Genetic Algorithms

In this chapter, I will discuss the implementation of a machine learning genetic algorithm to optimize the optical properties of nanomaterials.

Most of the work presented here is published as a preprint on SSRN [68] and is under production to be published in the Journal of the Optical Society of America B [10.1364/JOSAB.547482].

5.1. Motivation & background

The active control of light properties—such as amplitude, phase, and polarization—is a well-established technology, most notably implemented in liquid crystal (LC) displays and LC spatial light modulators. However, a fundamental limitation of this electro-optical mechanism lies in the relatively slow response time of Fréedericksz-transitions, governed by $\gamma d^2/K \approx ms$, where γ is the viscosity, d is the cell thickness, and K is the elastic constant of the liquid crystal [69,70].

Recent devices, like the one in Figure 5-1, have demonstrated a novel approach to address this limitation using diluted suspensions of gold nanorods [71] and other plasmonic materials. Unlike anisotropic molecules, gold nanorods exhibit sufficiently large electric susceptibility to strongly couple to external electric fields. This coupling overcomes thermal excitations, enabling direct alignment of individual nanorods without the need for liquid crystal phases. Consequently, gold nanorod suspensions are expected to achieve significantly faster switching times, with response times on the order of $\gamma L^3 / K_B T \approx$ μs, where L is the nanorod length, K_B is the Boltzmann constant, and T is the temperature.

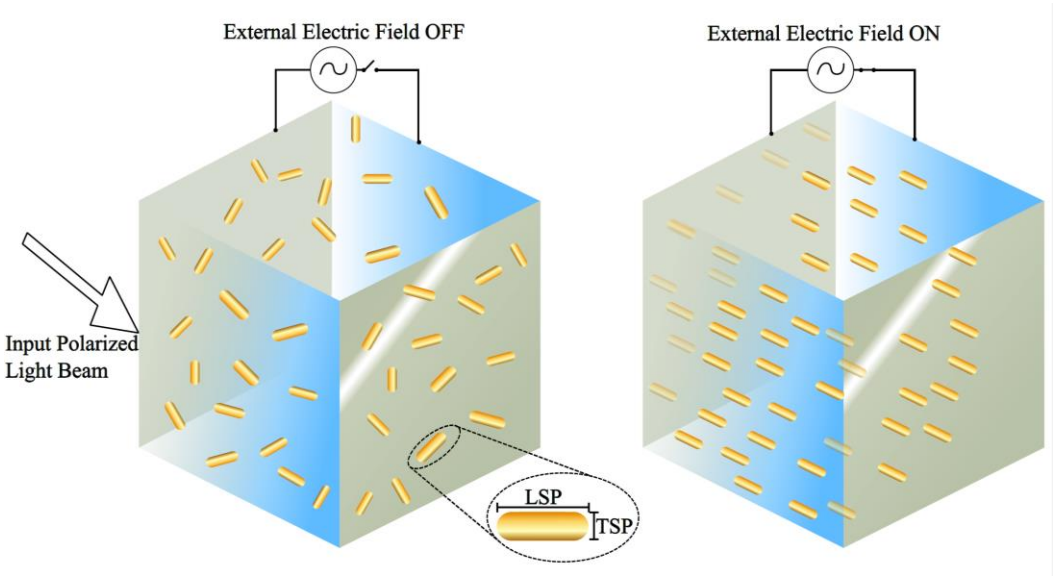

Figure 5-1: Schematic depiction of the dynamic plasmonic pixels. Adapted with permission from reference [72].

This breakthrough provides a promising alternative to traditional LC-based approaches, solving a longstanding challenge in electro-optical device performance by increasing the response time by 3 orders of magnitude.

This work is built upon previous research conducted by our group, where colleagues successfully developed fast micro-second optical switching devices [72] and an optical device with dynamic plasmonic pixels [71], both using gold nanorod suspensions and external electric fields to achieve light modulation.

Although opto-switching times have gotten faster, the absorption efficiency achieved through nanorod alignment remains an area that requires further optimization. Gold nanorods have two distinct absorption peaks, which are related to their longitudinal and transversal cross sections. Figure 5-2 below shows an example of nanorods with different aspect ratios (AR). Materials used for the experiments reported here were synthesized and sent to us by Dr. Kyoungweon Park (Air Force Research Laboratory), dispersed in toluene at 3-5 nM concentration respectively, made according to references [73,74]. The number which identifies each sample in this case was chosen to be the higher wavelength absorption peak, which corresponds to the longitudinal cross section extinction of the nanorod.

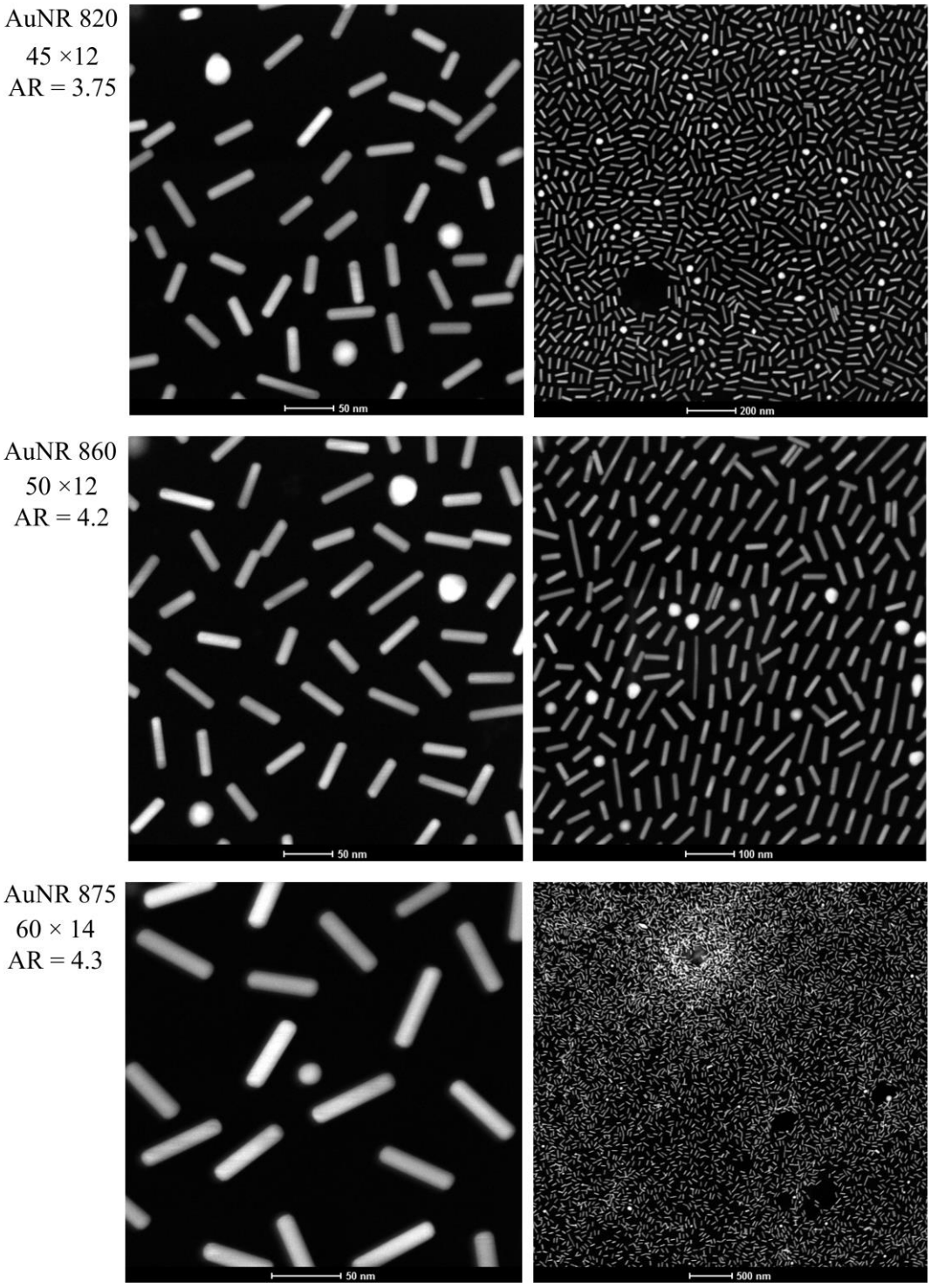

Figure 5-2: Electron microsocopy images of different nanorod samples, portraying different geometrical properties. The numbers (left) depict the average length x radius of the particles and their aspect ratio.

By changing the orientation of the nanorods in respect to incident light, as exemplified in Figure 5-1, it is possible to minimize the intensity of the lower energy (higher wavelength) absorption peak, as can be seen in Figure 5-3 below.

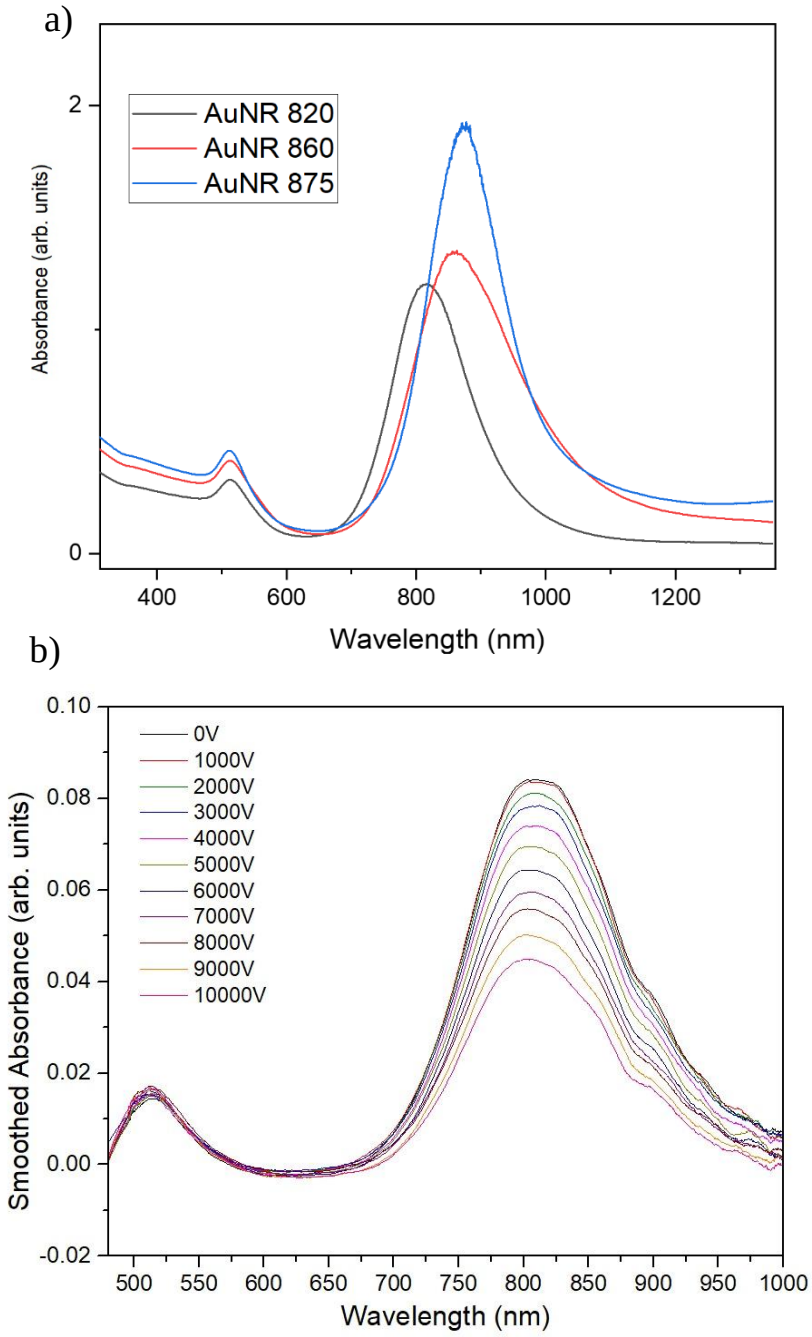

Figure 5-3: (a) Absorption as a function of wavelength for different nanorod configurations and (b) reduction of the absorption with an increase of the external applied voltage.

In this work, which is done in collaboration with José G. B. A. Lima (Federal University of Pernambuco, Informatics Center), I was invited to help choose suitable equations and parameters to feed a Genetic Algorithm (GA, [75]), validate the theoretical findings through my previous experimental research experience and run Finite Element Simulations in COMSOL Multiphysics to determine the extinction cross section of different nanorods configurations based on their geometrical features.

I will start the chapter with an overview of the algorithm chosen and then go straight to results and discussion. If there is interest, I highly recommend reading the published pre-print [68] where we conducted a vast review of the field and recent related work that combines computational methods for material optimization.

5.2. Multi-Objective Genetic Algorithms

When tackling real world problems, it is often necessary to simultaneously address multiple, and sometimes competing, objectives. Traditional optimization methods may struggle to navigate these complex problem spaces effectively. Multi-objective genetic algorithms (MOGAs) have emerged as a powerful and flexible tool to tackle such challenges [76,77]. The optimization process is inspired by nature's process of evolution. It mimics how populations evolve over time to find better solutions to survival challenges.

A distinguishing feature of MOGAs is their ability to handle non-linear and non-convex optimization landscapes, which are common in material design problems. By using processes like selection (picking the best solutions), crossover (combining features of two solutions), and mutation (introducing randomized small changes), MOGAs keep exploring the solution space while refining the results. Unlike single-objective algorithms, MOGAs do not seek a single optimal solution but instead identify a diverse set of Pareto-optimal solutions, providing the user with a spectrum of choices tailored to their specific priorities.

The application of MOGAs in material science has opened new possibilities for innovation. By optimizing structural and functional parameters simultaneously, these algorithms allow for the precise modification of material properties to meet physical properties. For example, in the context of plasmonic nanomaterials such as gold nanorods, geometrical parameters—such as aspect ratio and radius—significantly influence the optical extinction, which is in many cases counter-balanced by an increase in the torque necessary to physically turn the nanorods. MOGAs provide a systematic and efficient way to optimize these parameters, striking a balance between competing objectives. Another obvious advantage of using genetic algorithms that cover large solution spaces is the fact that there is not a clear theoretical indication of which exact aspect ratio produces efficient nanorods

for such applications, which causes previous experimental work [,] to be limited to few configurations.

In the next sections I will describe the application of MOGAs for optimizing the geometry of gold nanorods, with a specific focus on enhancing their optical absorbance. By leveraging the capabilities of MOGAs, this work aims to contribute to the development of plasmonic materials, laying the foundation for optimized materials in sensing, imaging, and optical switching technologies.

5.3. Proposed Method

The methodology for optimizing gold nanorods is outlined in the flowchart shown in Figure 5-4. This process is divided into two main phases. In Phase 1, the input parameters for implementing the MOGA are defined. The Non-dominated Sorting Genetic Algorithm II (NSGA-II) [78,79] was chosen due to its algorithmic complexity of O(MN^2), which is well-suited for this optimization task. Although more advanced algorithms, such as NSGA-III, were considered, their performance for low-dimensional optimization problems (e.g., fewer than ten objective functions) does not surpass that of NSGA-II, as demonstrated by previously published literature [80]. NSGA-II employs a selection operator, combining parent and child populations to promote elitism and diversity. This is achieved through a crowding distance metric that eliminates the need for a sharing parameter, providing a competitive advantage in the spread of solutions compared to its predecessors.

In Phase 2, statistical tests are applied to evaluate the algorithm's convergence and validate the differences between consecutive or distinct generations. These tests help identify chromosomes with the potential to maximize the desired optical properties. These selected chromosomes serve as input parameters for simulations in COMSOL Multiphysics. The flowchart also explicitly defines all resources required for finite element modeling.

While the equations for the objective functions could be theoretically sufficient for optimization, practical constraints and necessary approximations make the integration of numerical methods indispensable. This is my main contribution to present work, as FEM simulations to determine the extinction cross section of nanomaterials are well documented in literature and their results are

extremely precise. The validation of the algorithm's populations through statistical tests, performed by my collaborator José G. B. A. Lima, further ensures the reliability of the results.

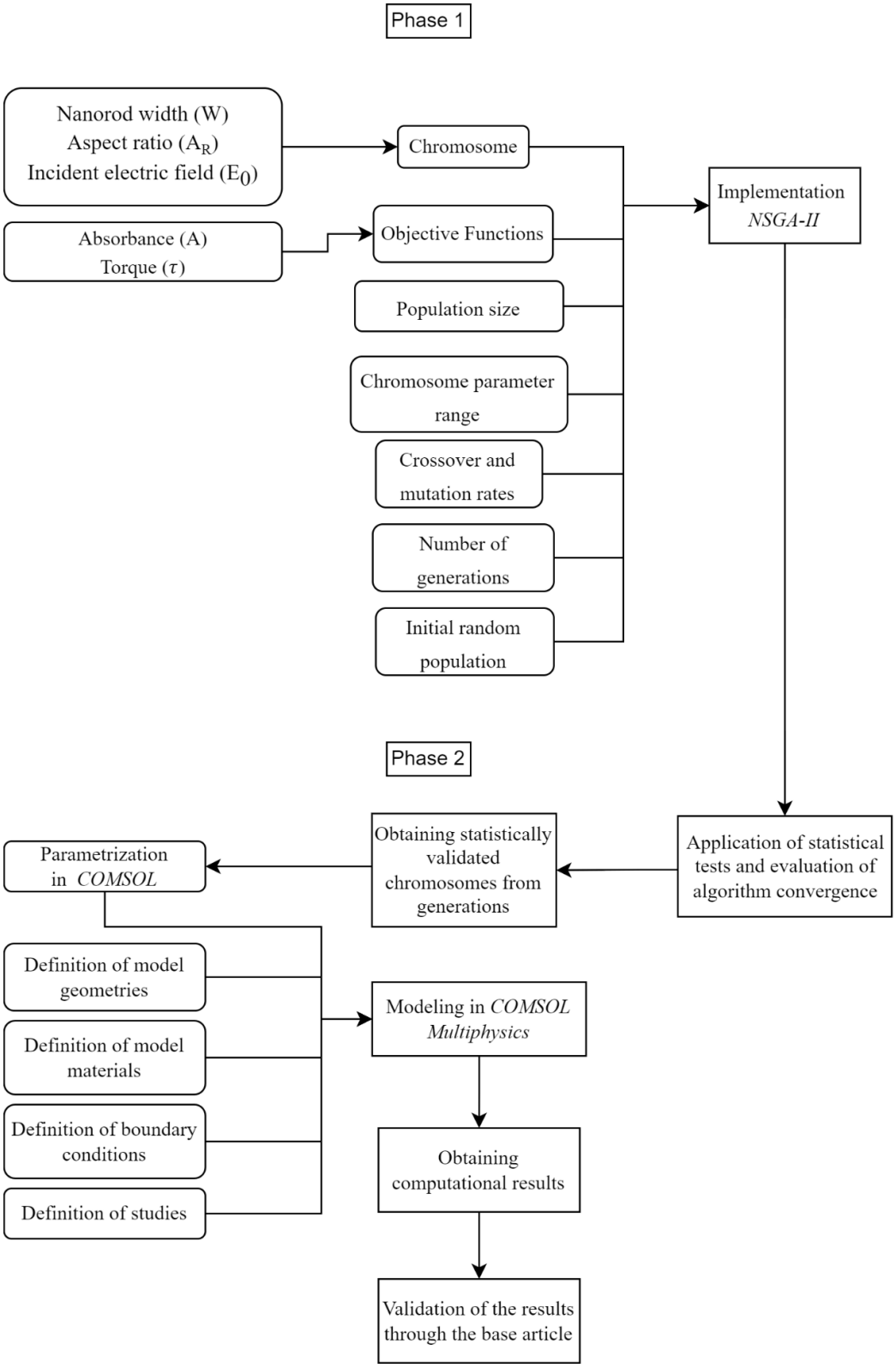

Figure 5-4: Flowchart of implemented methods.

5.4. NSGA-II parameters

Here I will present a summary of the implementation of the MOGA, as well as the objectives chosen to be optimized. I highly recommend reading the review in [81] and experimental work previously done by my colleagues [71,72] as it helps understanding the motivation of present work.

In the context of genetic algorithms, each chromosome in the population represents a set of genes, where each gene corresponds to a specific parameter of the gold nanorods. The value ranges for all genes considered were determined based on the minimum and maximum geometrical dimensions reported in experimental literature related to the synthesis of gold nanorods [73,82]. The genes chosen were the nanorod width (W), defined in the range [3 – 40] nm and the aspect ratio (A_R) set in the range [1.5 – 5].

To generate the extinction cross-section curves, the absorbance as a function of the wavelength plays a crucial role as it quantifies considerable amount of the light that is not transmitted, as has been already discussed in more detail in section 2.1 of this work. This metric is directly influenced by the geometric parameters of nanorod, making it a key parameter for analysis. Here, absorbance was selected as one of the objective functions to be maximized for the multi-objective genetic algorithm.

The absorption of a suspension of gold nanorods can be expressed as

$$A(t) = \frac{f\ L\ \mu(t)}{\ln 10}$$

where L is the optical path length in which light interacts with the sample, f is the volume fraction of nanorods (which can be estimated in the interval [0,1] and $\mu(t)$ is the absorption coefficient [83]. For an ensemble of nanorods we can define the absorption

$$\mu(t) = \int_0^{2\pi} \int_0^{\pi} (\mu_{\parallel}\, cos^2\theta + \mu_{\perp} \sin^2\theta)\, P(\theta, t)\, sin\theta\, d\theta\, d\phi$$

where $P(\theta, t)$ represents the probability distribution of the nanorods orientation, θ is the angle between the electric field and the nanorod long-axis, and ϕ is the azimuthal angle. Parameters $\mu_{\parallel}$ and $\mu_{\perp}$ are the intrinsic absorption coefficients of the material [84]. Assuming the nanoparticles' shape can be approximated as perfect prolate spheroids—a highly reasonable assumption given the precision achieved in nanorod synthesis, as seen in Figure 5.2—their optical properties can be calculated using the dielectric function of gold nanorods, ε, based on the Maxwell-Garnett model, as follows:

$$\mu_{\parallel(\perp)} = \frac{2\,\pi}{\lambda\, n_m}\, Im(\varepsilon) \left| \frac{\varepsilon_m}{\varepsilon_m + L_{\parallel(\perp)}(\varepsilon - \varepsilon_m)} \right|^2$$

Here, n_m represents the refractive index of the medium (in our case, n_m= $n_{toluene}$), ε_m is the dielectric constant of the medium, ε is the dielectric constant of the material ($\varepsilon = \varepsilon_{gold}$) which can be obtained, $Im(\varepsilon)$ denotes the imaginary part of the dielectric constant of the nanoparticle, and finally, $L_{\parallel(\perp)}$ are the depolarization factors, calculated from the eccentricity e of the spheroids [85].

$$L_{\parallel} = \frac{1 - e^2}{e^2}\left(\frac{1}{2e}\ln\frac{1+e}{1-e} - 1\right)$$

$$L_{\perp} = \frac{1 - L_{\parallel}}{2}$$

In this study, we consider two ideal configurations determined by the order parameter S, which serves as a binary indicator of the nanorods' alignment state. When S = 0 the system consists of completely non-aligned nanorods; S = 1 represents a state of perfect alignment with the external electric field [86].

Finally, the absorption coefficient, as defined in the preceding equations, can be expressed in terms of the order parameter:

$$\mu_1 = \frac{1}{3}[(\mu_{\perp} + 2\mu_{\parallel}) + 2(\mu_{\perp} - \mu_{\parallel})\, S]$$

$$\mu_2 = \frac{1}{3}[(\mu_{\perp} + 2\mu_{\parallel}) - (\mu_{\perp} - \mu_{\parallel})\, S]$$

μ_1 corresponds to the case where the light polarization is parallel to the direction of the electric field (nanorods aligned with the light propagation, resulting in minimum absorption), while μ_2 occurs when the polarization is perpendicular (nanorods not aligned, resulting in maximum absorption). In our study, the goal is to maximize absorption to enhance the efficiency of plasmonic light-switching devices. Therefore, we focus on the scenario where the light polarization is perpendicular to the field direction (as illustrated in Figure 5-1). This represents the first objective to be optimized using the algorithm.

In addition to absorbance, the torque exerted on the nanorods under an applied electric field was also evaluated as an objective function. The calculation of the torque is approximated by considering the contribution solely from the induced electric dipole p, expressed as:

$$p = \epsilon\, \Delta\alpha\, E(t)$$

Where ϵ is the electrical permittivity of the medium, $\Delta\alpha$ is the difference between longitudinal and transversal polarizabilities ($\Delta\alpha = \alpha_\perp - \alpha_\parallel$). Considering the approximation for the torque experienced by the nanorod as a function of the electric dipole described above [83,87], the final expression can be written as

$$\tau = \epsilon\, \Delta\alpha\, \mathrm{E}^2$$

The value of $\Delta\alpha = \alpha_\perp - \alpha_\parallel$ can be determined from the relation

$$\alpha_{\perp,\parallel} = \frac{V(\epsilon_p - \epsilon_m)}{\epsilon_m + L_{\perp,\parallel}(\epsilon_p - \epsilon_m)}$$

and the torque, as defined above, is the second objective function to be optimized by the algorithm.

In accordance with the initialization procedure of the NSGA-II algorithm [88], the chromosome parameters (W, A_R) will be randomly assigned within the specified acceptable intervals to generate the initial population.

5.5. Results & Discussion

The implementation of the NSGA-II algorithm was carried out based on the equations outlined in the last section, which define the objective functions. The population size was set to 150 individuals, and the algorithm ran for 200 generations. A selection process was employed to prioritize individuals with higher absorbance values and lower torque, aiming to form the Pareto frontier through the maximization of one objective and minimization of the other. The population size and number of generations were determined through several tests, where the algorithm's hyperparameters, including crossover rate, mutation, and other parameters, were varied. After multiple iterations, the robustness of the solutions obtained with these values was confirmed as we observed convergence of the optimized results around generation 85.

Figure 5-5 shows the Pareto frontier, which links the maximization of absorbance with the minimization of torque experienced by the gold nanorods. The plot reveals the typical asymptotic behavior of the best solutions generated by the NSGA-II algorithm.

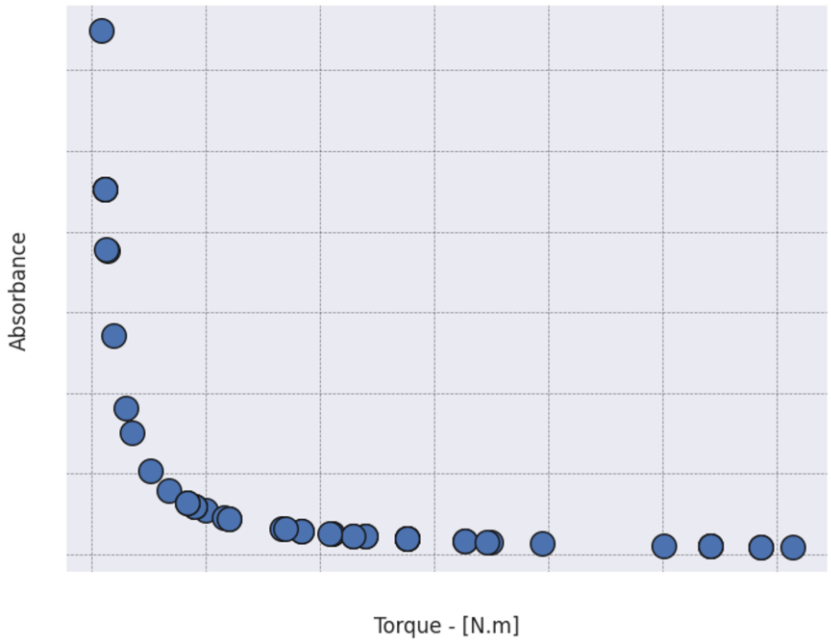

Figure 5-5: Pareto frontier of the convergence population.

5.5.1. Statistical tests and validation of generations

Statistical tests help determine whether the differences observed between the results produced by the algorithm are statistically significant or simply due to random fluctuations. To evaluate the quality of the nanorod configurations and ensure the algorithm is converging properly, we used the Mann-Whitney and Kruskal-Wallis tests. I highly recommend verifying Tables I and II from our published work [68] to assess the complete statistics that were done in collaboration.

The Mann-Whitney test is a non-parametric test used to compare the medians of two independent samples [89]. It doesn't require the samples to follow a normal distribution and is suitable for unnormalized continuous data. If the calculated p-value is less than 0.05, it suggests that the samples have different distributions and that the compared individuals have distinct performances. Conversely, a p-value greater than 0.05 indicates that there is not enough evidence to reject the null hypothesis, implying the samples have similar distributions. The results obtained from this test align with the step function, indicating statistical differences between the initial populations, suggesting that they have different performances. High values of the test statistic imply that individuals from higher-generation populations tend to have better parameter values. After generation 80, the p-value was much greater than the 5% significance level, providing no evidence to reject the null hypothesis. This suggests that the distributions are similar and that the performance of the nanorod solutions in the two populations will be comparable, proving that we have probably achieved convergence to the optimized maximum-absorbance individuals around that generation.

The Kruskal-Wallis test [90,91], on the other hand, is used to compare three or more independent samples and can be applied to assess the convergence quality of the NSGA-II algorithm. Analyzing the values obtained for the last generations, along with a p-value greater than 5%, there is once again no evidence to reject the null hypothesis. These results are consistent with the Mann-Whitney test, suggesting that there are no significant differences between the individuals in populations 80 and 85, thus further confirming the convergence obtained [92].

Based on the results from the applied hypothesis tests, five configurations corresponding to generations 20, 40, 60, 80, and 85 were selected. The values of

the nanorod parameters for these generations are shown in Tables 4 and 5 below. As a result, 25 different gold nanorod geometrical configurations were obtained, which will then be modeled using FEM through COMSOL Multiphysics.

Table 4: Nanorod parameters - generations 20, 40 and 60.

Generation	Configuration	W [nm]	AR
20	1	4.88	14.91
	2	5.71	11.42
	3	6.044	12.12
	4	8.827	13.08
	5	9.38	12.75
40	1	14.95	13.53
	2	16.69	12.66
	3	17.27	11.84
	4	18.46	13.806
	5	19.57	13.53
60	1	20.89	14.82
	2	21.11	13.76
	3	21.6	12.46
	4	20.89	12.46
	5	21.6	13.08

Table 5: Nanorod parameters - generations 80 and 85.

Generation	Configuration	W [nm]	AR
80	1	31.208	13.53
	2	31.208	13.08
	3	32.62	11.84
	4	34.78	12.75
	5	34.78	13.08
85	1	31.208	12.46
	2	31.08	14.91
	3	32.62	11.84
	4	34.78	13.8
	5	39.34	13.08

5.5.2. Finite Element Method results

The 25 configurations of gold nanorods were simulated using the finite element method in COMSOL Multiphysics, and the extinction cross-section (ECS) curves for each configuration were generated [93-95]. Figures 5-6 through 5-7d display the evolution of the ECS for configurations 1 to 5 of each generation. In Figure 5-6, a zoomed-in view of generation 20 is shown, as the values for the

extinction curves are on the order of 10^{-16} m². Configurations 2 to 5 from generation 20 also fall within this range, but to improve legibility, only the results for configuration 1 are chosen to be shown.

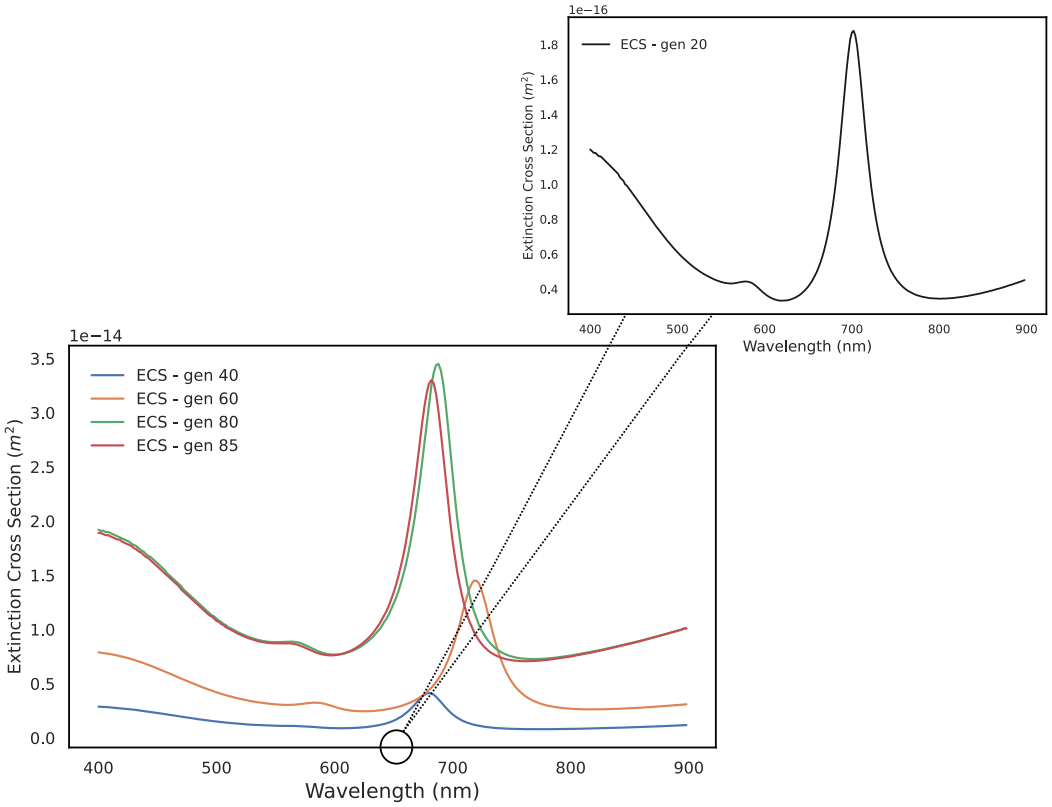

Figure 5-6: ECS as a function of wavelength for multiple generations, confirming the evolving process of configuration 1.

The comparison of results is primarily focused on the order of magnitude of the extinction curves, as the physical phenomena associated with the alignment of the gold nanorods and the simulation of these configurations through finite element modeling are well-established in the literature. The base simulation model in COMSOL Multiphysics, which was used to obtain all configurations, was provided by the corresponding author of the foundational article [] and thoroughly modified to suit our system. The cross-section magnitudes in the referenced article are on the order of 10^{-15} m².

The results presented in next figures demonstrate the evolution of the extinction cross-sections of the gold nanorods. In the early generations (20 and 40), the extinction curves have magnitudes between 10^{-16} m² and 10^{-15} m², reflecting the initial phase of the genetic algorithm. During this phase, the individuals in the first

generations are expected to have suboptimal parameters, as the algorithm is still in the process of finding better solutions across generations.

From generation 60 onward, the order of magnitude for extinction cross-section values ranges between 10^{-15} m² and 10^{-14} m², with configurations yielding higher values for the extinction curves. Generations 80 and 85 consistently produced extinction curves with magnitudes in the range of 10^{-14} m^2, which are very similar to each other. This result further supports the statistical evidence regarding the similarity in the performance of these solutions.

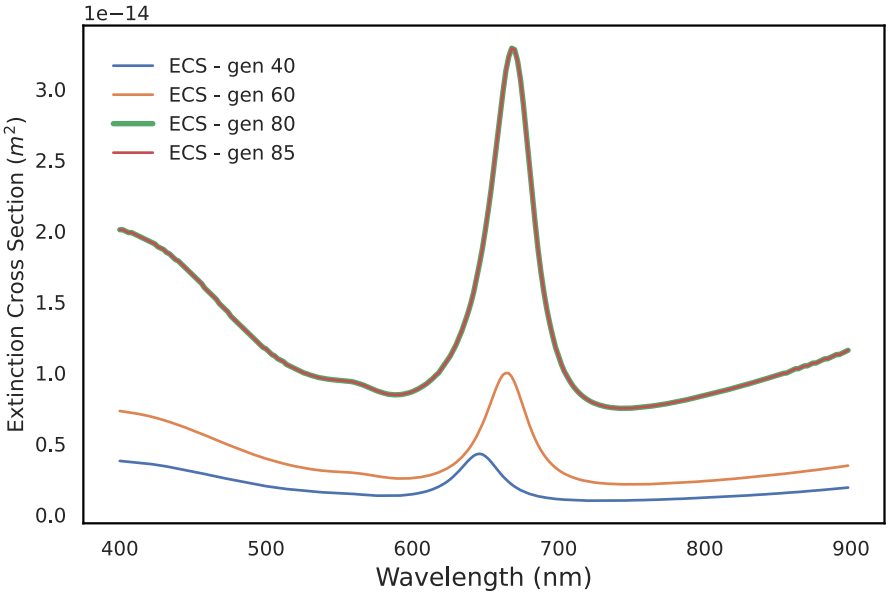

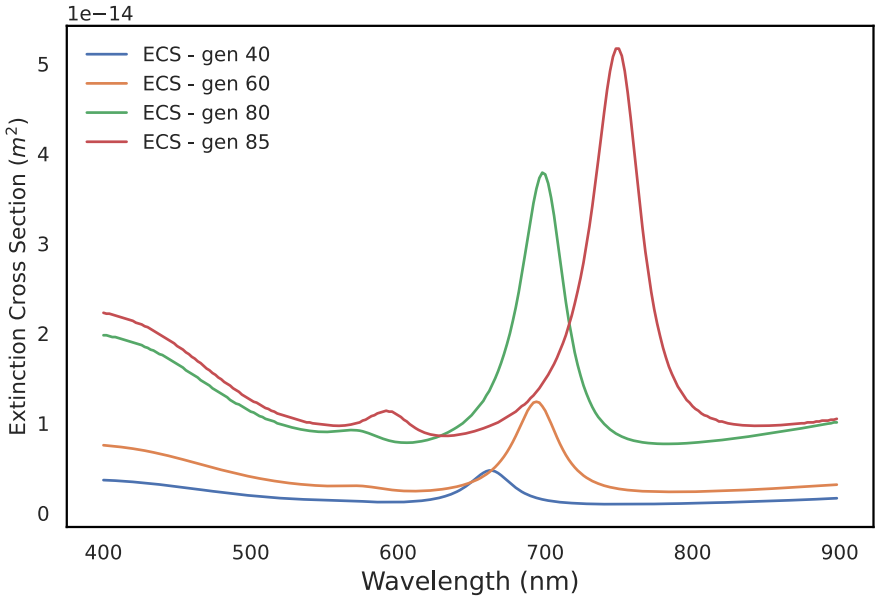

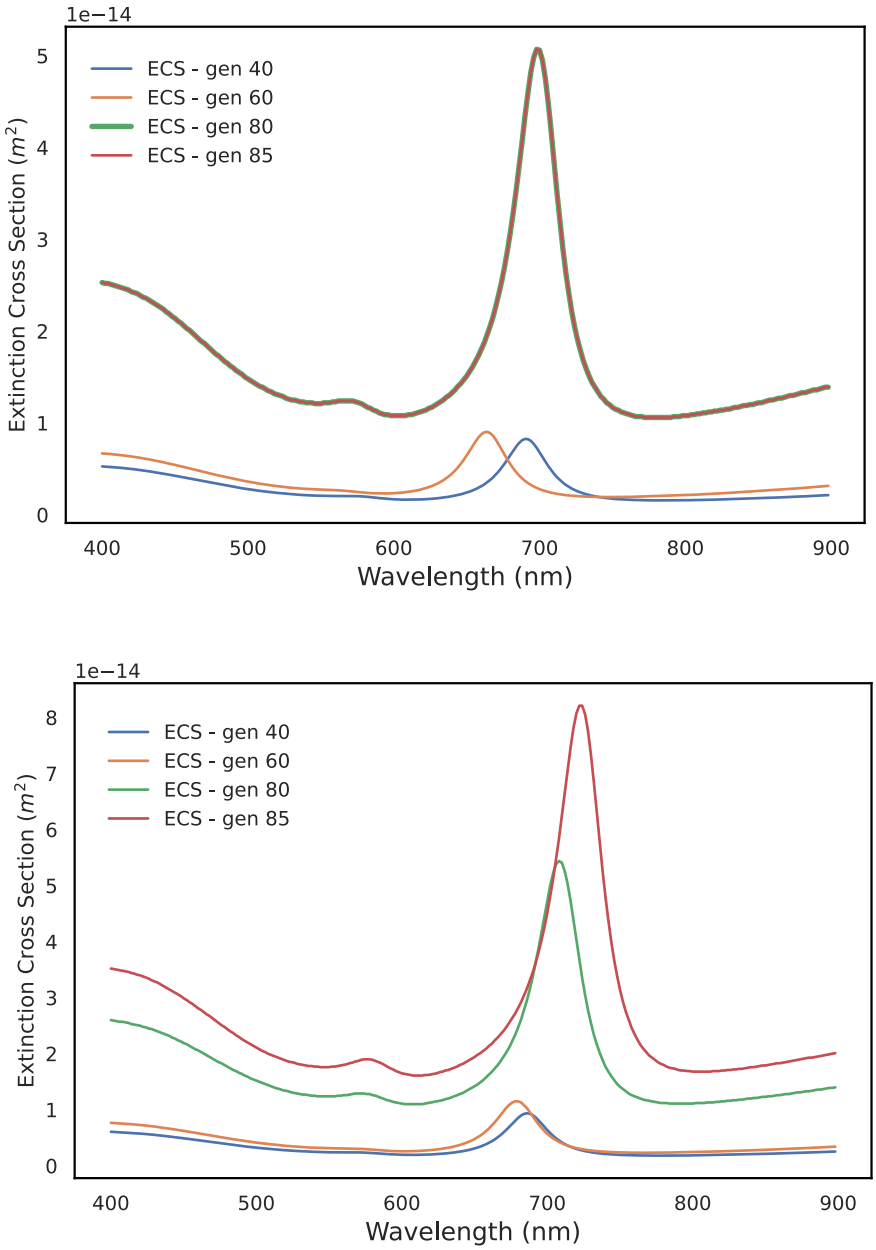

Figure 5-7: ECS as a function of the wavelength for multiple generations, confirming the evolving process of configurations 2-5, respectively.

The observed increase in the baseline of the absorbance plot correlates with an increase in the nanorod width (*W*). This outcome is expected since the optical path for light-material interaction in the non-aligned mode depends on the gold nanorod's width.

In the context of designing and optimizing light-switching devices, as discussed in [71], it is advantageous for the nanorods to exhibit minimal absorption when aligned with the incident light source. In simulations where the nanoparticles

are perfectly aligned with the incident light, the absorption cross-section resembles that of a spherical particle. Consequently, only the first absorption peak is observed in the results obtained by solving the equations for the scattered field. This peak corresponds to the transverse cross-section of the nanorod, while the higher wavelength peak arises from the longitudinal component.

In real experiments, however, not all nanorods are perfectly aligned due to fluctuations in their axis and the external electric field. As a result, some absorption is observed at higher wavelengths, as noted in [71,72]. This discrepancy highlights the difference between idealized simulations and practical experimental conditions.

A comparison of our results with previously published literature highlights those studies usually only present normalized absorbance data, focusing primarily on peak absorbance values, while often overlooking precise extinction coefficients which depend significantly on nanorod sizes and aspect ratios. Notable advancements in nanorod optimization, both experimental and computational, have been reported by colleagues [96], achieving maximum efficiencies with extinction cross sections (ECS) of 7×10^{-14} m² for specific configurations. In contrast, the optimized nanorod populations generated in this study exhibit efficiencies approximately 15% higher, further confirming the effectiveness of the proposed computational evolutionary method.

6 References

[1] GERMANO, M. et al. Flexible random lasers in dye-doped bio-degradable cellulose nanocrystalline needles. **Journal of the Optical Society of America B**, v. 37, n. 1, p. 24–24, 2 dez. 2020.

[2] MACHADO, Y. D. R. et al. Impact of SiO2 nanoparticle morphology on scattering efficiency for random lasers. **Optical Materials**, v. 148, p. 114775, 31 dez. 2024.

[3] BOYD, R. W. **Nonlinear optics**. Amsterdam: Academic Press, 2019.

[4] HUANG, D. et al. Optical coherence tomography. **Science**, v. 254, n. 5035, p. 1178–1181, 22 nov. 1991.

[5] MULVANEY, S. P.; KEATING, C. D. Raman Spectroscopy. **Analytical Chemistry**, v. 72, n. 12, p. 145–158, 10 maio 2000.

[6] SEKERA, Z. Light Scattering in the Atmosphere and the Polarization of Sky Light*. **Journal of the Optical Society of America**, v. 47, n. 6, p. 484, 1 jun. 1957.

[7] DE, V. **Light scattering by small particles**. [s.l.] New York, Ny Dover Ca Press, 2009.

[8] SVELTO, O. **Principles of Lasers**. Boston, MA: Springer US, 2010.

[9] AMBARTSUMYAN, R. V. et al. Non-resonant feedback in lasers. **Progress in quantum electronics/Progress in Quantum Electronics**, v. 1, p. 107–185, 1 jan. 1970.

[10] S, L. V. Generation of Light by a Scattering Medium with Negative Resonance Absorption. **Soviet Journal of Experimental and Theoretical Physics**, v. 26, p. 835, abr. 1968.

[11] LAWANDY, N. M. et al. Laser action in strongly scattering media. **Nature**, v. 368, n. 6470, p. 436–438, 31 mar. 1994.

[12] CAO, H. et al. Photon Statistics of Random Lasers with Resonant Feedback. **Physical Review Letters**, v. 86, n. 20, p. 4524–4527, 14 maio 2001.

[13] ОЛЕГ ЗАЙЦЕВ. Mode statistics in random lasers. **Physical Review A**, v. 74, n. 6, 5 dez. 2006.

[14] BARTHELEMY, P.; BERTOLOTTI, J.; WIERSMA, D. S. A Lévy flight for light. **Nature**, v. 453, n. 7194, p. 495–498, maio 2008.

[15] CID ARAÚJO; GOMES, A.; RAPOSO, E. Lévy Statistics and the Glassy Behavior of Light in Random Fiber Lasers. **Applied Sciences**, v. 7, n. 7, p. 644–644, 22 jun. 2017.

[16] L. ANGELANI et al. Glassy Behavior of Light. **Physical Review Letters**, v. 96, n. 6, 16 fev. 2006.

[17] GOMES, A. S. L. et al. Recent advances and applications of random lasers and random fiber lasers. **Progress in Quantum Electronics**, v. 78, p. 100343, ago. 2021.

[18] YANG, S.; WANG, Y.; SUN, H. Advances and Prospects for Whispering Gallery Mode Microcavities. **Advanced Optical Materials**, v. 3, n. 9, p. 1136–1162, 11 ago. 2015.

[19] SAPIENZA, R. Determining random lasing action. **Nature Reviews Physics**, v. 1, n. 11, p. 690–695, 15 out. 2019.

[20] FERNANDES, S. N. et al. Mind the Microgap in Iridescent Cellulose Nanocrystal Films. v. 29, n. 2, p. 1603560–1603560, 1 jan. 2017.

[21] YANG, L. et al. Effective random laser action in Rhodamine 6G solution with Al nanoparticles. **Applied Optics**, v. 50, n. 13, p. 1816–1816, 19 abr. 2011.

[22] MAGDE, D.; WONG, R.; SEYBOLD, P. G. Fluorescence Quantum Yields and Their Relation to Lifetimes of Rhodamine 6G and Fluorescein in Nine Solvents: Improved Absolute Standards for Quantum Yields. **Photochemistry and Photobiology**, v. 75, n. 4, p. 327, 2002.

[23] MORGANA, S. et al. Fluorescence-based detection: A review of current and emerging techniques to unveil micro/ nanoplastics in environmental samples. **TrAC Trends in Analytical Chemistry**, v. 172, p. 117559–117559, 25 jan. 2024.

[24] **UVA1 phototherapy | DermNet**. Disponível em: <https://dermnetnz.org/topics/uva1-phototherapy>.

[25] **UVB Phototherapy (ultraviolet light treatment) | DermNet**. Disponível em: <https://dermnetnz.org/topics/uvb-phototherapy>.

[26] MORTON, C. A. et al. Guidelines for topical photodynamic therapy: report of a workshop of the British Photodermatology Group. **British Journal of Dermatology**, v. 146, n. 4, p. 552–567, abr. 2002.

[27] NEWMAN, T. B. et al. Numbers Needed to Treat With Phototherapy According to American Academy of Pediatrics Guidelines. **PEDIATRICS**, v. 123, n. 5, p. 1352–1359, 27 abr. 2009.

[28] PEI, S. et al. Light-based therapies in acne treatment. **Indian Dermatology Online Journal**, v. 6, n. 3, p. 145–157, 2015.

[29] SANASSI, L. A. Seasonal affective disorder. **Journal of the American Academy of Physician Assistants**, v. 27, n. 2, p. 18–22, fev. 2014.

[30] MENG, X. et al. Tunable random laser in flexible hydrogel. **Optical Materials**, v. 115, p. 111027, maio 2021.

[31] ALAM, F. et al. 3D Printed Contact Lenses. **ACS biomaterials science & engineering**, v. 7, n. 2, p. 794–803, 8 fev. 2021.

[32] MENG, X. et al. Tunable random laser in flexible hydrogel. **Optical Materials**, v. 115, p. 111027, maio 2021.

[32] YANG, H. et al. Cellulose-Based Scattering Enhancers for Light Management Applications. **ACS Nano**, v. 16, n. 5, p. 7373–7379, 27 abr. 2022.

[33] RAO, K. S. et al. A novel method for synthesis of silica nanoparticles. **Journal of Colloid and Interface Science**, v. 289, n. 1, p. 125–131, set. 2005.

[34] **Crystal Quartz SiO2 Optical Material | Crystran**. Disponível em: <https://www.crystran.com/optical-materials/crystal-quartz-sio2>. Acesso em: 17 jan. 2025.

[35] ZEHENTBAUER, F. M. et al. Fluorescence spectroscopy of Rhodamine 6G: Concentration and solvent effects. **Spectrochimica Acta Part A: Molecular and Biomolecular Spectroscopy**, v. 121, p. 147–151, mar. 2014.

[36] BATHE, K.-J. **Finite Element Procedures.** S.L.: S.N, 2014.

[37] KUMAR, B. et al. Localized modes revealed in random lasers. **Optica**, v. 8, n. 8, p. 1033–1033, 21 jun. 2021.

[38] KLEINMAN, D. A. Theory of Second Harmonic Generation of Light. **Physical Review**, v. 128, n. 4, p. 1761–1775, 15 nov. 1962.

[39] AKHMANOV, S. A.; SUKHORUKOV, A. P.; KHOKHLOV, R. V. SELF-FOCUSING AND DIFFRACTION OF LIGHT IN A NONLINEAR MEDIUM. v. 10, n. 5, p. 609–636, 31 maio 1968.

[40] GANEEV, R. A. Nonlinear refraction and nonlinear absorption of various media. **Journal of Optics A: Pure and Applied Optics**, v. 7, n. 12, p. 717–733, 21 out. 2005.

[41] SOLOMON, K. D. et al. LASIK World Literature Review. **Ophthalmology**, v. 116, n. 4, p. 691–701, abr. 2009.

[42] HENDRICKX, E.; CLAYS, K.; PERSOONS, A. Hyper-Rayleigh Scattering in Isotropic Solution. **Accounts of Chemical Research**, v. 31, n. 10, p. 675–683, 3 set. 1998.

[43] MARLAN ORVIL SCULLY; MUHAMMAD SUHAIL ZUBAIRY. **Quantum optics**. Cambridge: Cambridge University Press, 2008.

[44] CÉCILE JOULAUD et al. Characterization of the nonlinear optical properties of nanocrystals by Hyper Rayleigh Scattering. **Journal of Nanobiotechnology**, v. 11, n. S1, 1 dez. 2013.

[45] CLAYS, K.; ANDRÉ PERSOONS. Hyper-Rayleigh scattering in solution. **Physical Review Letters**, v. 66, n. 23, p. 2980–2983, 10 jun. 1991.

[46] KAROLINE, A.; SAROTTI, A. M.; MARTINS, F. T. Synthon trends according to acid strength and geometry in salts of N-heterocyclic bases. **CrystEngComm**, v. 19, n. 40, p. 5960–5965, 1 jan. 2017.

[47] HAGIMOTO, K.; MITO, A. Determination of the second-order susceptibility of ammonium dihydrogen phosphate and α-quartz at 633 and 1064 nm. **Applied Optics**, v. 34, n. 36, p. 8276, 20 dez. 1995.

[48] BARBOSA-SILVA, R. et al. First Hyperpolarizability of 1,3-Thiazolium-5-Thiolates Mesoionic Compounds. **The Journal of Physical Chemistry C**, v. 123, n. 1, p. 677–683, 20 dez. 2018.

[49] BARBOSA-SILVA, R. et al. Second-order nonlinearity of NaNbO3 nanocrystals with orthorhombic crystalline structure. **Journal of Luminescence**, v. 211, p. 121–126, 8 mar. 2019.

[50] WOODFORD, J. N.; PAULEY, M. A.; WANG, C. H. Solvent Dependence of the First Molecular Hyperpolarizability of *p*-Nitroaniline Revisited. **The Journal of Physical Chemistry A**, v. 101, n. 11, p. 1989–1992, 1 mar. 1997.

[51] KLEIN, J. et al. Limitations of the Tauc Plot Method. **Advanced Functional Materials**, v. 33, n. 47, 3 set. 2023.

[52] VIEZBICKE, B. D. et al. Evaluation of the Tauc method for optical absorption edge determination: ZnO thin films as a model system. **physica status solidi (b)**, v. 252, n. 8, p. 1700–1710, 16 mar. 2015.

[53] CHHOWALLA, M. et al. The chemistry of two-dimensional layered transition metal dichalcogenide nanosheets. **Nature Chemistry**, v. 5, n. 4, p. 263–275, 20 mar. 2013.

[54] MANZELI, S. et al. 2D transition metal dichalcogenides. **Nature Reviews Materials**, v. 2, n. 8, p. 1–15, 13 jun. 2017.

[55] JAWAID, A. et al. Redox Exfoliation of Layered Transition Metal Dichalcogenides. v. 11, n. 1, p. 635–646, 4 jan. 2017.

[56] JAWAID, A. M.; RITTER, A. J.; VAIA, R. A. Mechanism for Redox Exfoliation of Layered Transition Metal Dichalcogenides. **Chemistry of Materials**, v. 32, n. 15, p. 6550–6565, 13 jul. 2020.

[57] DICKINSON, R. G.; PAULING, L. THE CRYSTAL STRUCTURE OF MOLYBDENITE. v. 45, n. 6, p. 1466–1471, 1 jun. 1923.

[58] WILSON, J. A.; YOFFE, A. D. The transition metal dichalcogenides discussion and interpretation of the observed optical, electrical and structural properties. **Advances in Physics**, v. 18, n. 73, p. 193–335, maio 1969.

[59] FRINDT, R. F.; YOFFE, A. D. Physical Properties of Layer Structures: Optical Properties and Photoconductivity of Thin Crystals of Molybdenum Disulphide. **Proceedings of the Royal Society of London. Series A, Mathematical and Physical Sciences**, v. 273, n. 1352, p. 69–83, 1963.

[60] TENNE, R. et al. Polyhedral and cylindrical structures of tungsten disulphide. **Nature**, v. 360, n. 6403, p. 444–446, dez. 1992.

[61] YASUDA, E. et al. **Carbon Alloys**. [s.l.] Elsevier, 2003.

[62] GEIM, A. K.; NOVOSELOV, K. S. The rise of graphene. **Nature Materials**, v. 6, n. 3, p. 183–191, mar. 2007.

[63] MAK, K. F. et al. Atomically ThinMoS2: A New Direct-Gap Semiconductor. **Physical Review Letters**, v. 105, n. 13, 24 set. 2010.

[64] LONG, D.-L.; TSUNASHIMA, R.; CRONIN, L. Polyoxometalates: Building Blocks for Functional Nanoscale Systems. **Angewandte Chemie International Edition**, v. 49, n. 10, p. 1736–1758, 1 mar. 2010.

[65] YAO, Y. et al. High-Concentration Aqueous Dispersions of MoS2. **Advanced Functional Materials**, v. 23, n. 28, p. 3577–3583, 27 fev. 2013.

[66] DOUVAS, A. M. et al. Sol–gel synthesized, low-temperature processed, reduced molybdenum peroxides for organic optoelectronics applications. **Journal of Materials Chemistry C**, v. 2, n. 31, p. 6290–6290, 26 maio 2014.

[67] QUAN, J. et al. Phonon renormalization in reconstructed MoS2 moiré superlattices. **Nature Materials**, v. 20, n. 8, p. 1100–1105, 1 ago. 2021.

[68] LIMA, A. et al. Optimization of gold nanorods' optical properties via Multi-Objective Genetic Algorithms. 1 jan. 2024.

[69] PIERRE-GILLES DE GENNES; PROST, J. **The physics of liquid crystals**. Oxford: Clarendon Press, 2013.

[70] ZHANG, Y. et al. Metal Nanoparticle Dispersion, Alignment, and Assembly in Nematic Liquid Crystals for Applications in Switchable Plasmonic Color Filters and E-Polarizers. **ACS Nano**, v. 9, n. 3, p. 3097–3108, 4 mar. 2015.

[71] FONTANA, J. et al. Electric field induced orientational order of gold nanorods in dilute organic suspensions. **Applied Physics Letters**, v. 108, n. 8, 22 fev. 2016.

[72] ETCHEVERRY, S. et al. Microsecond switching of plasmonic nanorods in an all-fiber optofluidic component. **Optica**, v. 4, n. 8, p. 864, 26 jul. 2017.

[73] PARK, K.; KOERNER, H.; VAIA, R. A. Depletion-Induced Shape and Size Selection of Gold Nanoparticles. **Nano Letters**, v. 10, n. 4, p. 1433–1439, 29 mar. 2010.

[74] NEPAL, D. et al. Large Scale Solution Assembly of Quantum Dot–Gold Nanorod Architectures with Plasmon Enhanced Fluorescence. **ACS Nano**, v. 7, n. 10, p. 9064–9074, 10 set. 2013.

[75] MIRJALILI, S. Genetic Algorithm. **Studies in Computational Intelligence**, v. 780, p. 43–55, 27 jun. 2018.

[76] KONAK, A.; COIT, D. W.; SMITH, A. E. Multi-objective optimization using genetic algorithms: A tutorial. **Reliability Engineering & System Safety**, v. 91, n. 9, p. 992–1007, set. 2006.

[77] RAGHU SENGUPTA; APARNA GUPTA; JOYDEEP DUTTA. **Decision Sciences Theory and Practice**. [s.l.] Taylor & Francis Group, Broken Sound Parkway Nw, Suite 300, Boca Raton, Fl 7- Crc Press, 6000.

[78] DEB, K. et al. A fast and elitist multiobjective genetic algorithm: NSGA-II. **IEEE Transactions on Evolutionary Computation**, v. 6, n. 2, p. 182–197, abr. 2002.

[79] YUSOFF, Y.; NGADIMAN, M. S.; ZAIN, A. M. Overview of NSGA-II for Optimizing Machining Process Parameters. **Procedia Engineering**, v. 15, p. 3978–3983, 2011.

[80] HISAO ISHIBUCHI et al. Performance comparison of NSGA-II and NSGA-III on various many-objective test problems. 1 jul. 2016.

[81] KATOCH, S.; CHAUHAN, S. S.; KUMAR, V. A review on genetic algorithm: past, present, and future. **Multimedia Tools and Applications**, v. 80, n. 5, 31 out. 2020.

[82] PARK, K. et al. Engineering the Optical Properties of Gold Nanorods: Independent Tuning of Surface Plasmon Energy, Extinction Coefficient, and Scattering Cross Section. v. 118, n. 11, p. 5918–5926, 7 mar. 2014.

[83] RUDA, H. E.; SHIK, A. Nanorod dynamics in ac electric fields. **Nanotechnology**, v. 21, n. 23, p. 235502, 17 maio 2010.

[84] MOHAMMADIMASOUDI, M.; HENS, Z.; NEYTS, K. Full alignment of dispersed colloidal nanorods by alternating electric fields. **RSC Advances**, v. 6, n. 61, p. 55736–55744, 2016.

[85] BORAH, R. et al. Plasmon resonance of gold and silver nanoparticle arrays in the Kretschmann (attenuated total reflectance) vs. direct incidence configuration. **Scientific Reports**, v. 12, n. 1, p. 15738, 21 set. 2022.

[86] MADER, M. et al. Quantitative Determination of the Complex Polarizability of Individual Nanoparticles by Scanning Cavity Microscopy. **ACS Photonics**, v. 9, n. 2, p. 466–473, 28 jan. 2022.

[87] LIAW, J.-W.; LO, W.-J.; KUO, M.-K. Wavelength-dependent longitudinal polarizability of gold nanorod on optical torques. **Optics Express**, v. 22, n. 9, p. 10858–10858, 29 abr. 2014.

[88] VERMA, S.; PANT, M.; SNASEL, V. A Comprehensive Review on NSGA-II for Multi-Objective Combinatorial Optimization Problems. **IEEE Access**, v. 9, p. 57757–57791, 2021.

[89] MACFARLAND, T. W.; YATES, J. M. Mann–Whitney U test. **Introduction to Nonparametric Statistics for the Biological Sciences Using R**, p. 103–132, 2016.

[90] OSTERTAGOVÁ, E.; OSTERTAG, O.; KOVÁČ, J. **Methodology and Application of the Kruskal-Wallis Test**. Disponível em: <https://www.scientific.net/AMM.611.115>.

[91] MCKIGHT, P. E.; NAJAB, J. Kruskal-Wallis Test. **The Corsini Encyclopedia of Psychology**, 30 jan. 2010.

[92] ZHOU, S. et al. On the Convergence of Stochastic Multi-Objective Gradient Manipulation and Beyond. **Advances in Neural Information Processing Systems**, v. 35, p. 38103–38115, 6 dez. 2022.

[93] TANG, J. et al. Calculation extinction cross sections and molar attenuation coefficient of small gold nanoparticles and experimental observation of their UV–vis spectral

properties. **Spectrochimica Acta Part A: Molecular and Biomolecular Spectroscopy**, v. 191, p. 513–520, 15 fev. 2018.

[94] KHLEBTSOV, N. G. Determination of Size and Concentration of Gold Nanoparticles from Extinction Spectra. **Analytical Chemistry**, v. 80, n. 17, p. 6620–6625, set. 2008.

[95] PELLAS, V. et al. Gold Nanorods for LSPR Biosensing: Synthesis, Coating by Silica, and Bioanalytical Applications. **Biosensors**, v. 10, n. 10, p. 146, 17 out. 2020.

[96] PARK, K. et al. Engineering the Optical Properties of Gold Nanorods: Independent Tuning of Surface Plasmon Energy, Extinction Coefficient, and Scattering Cross Section. v. 118, n. 11, p. 5918–5926, 7 mar. 2014.

[97] Machado, Y. et al. Electric Field-Induced Instability of Redox-Exfoliated Layered Transition Metal Dichalcogenides. **The Journal of Physical Chemistry C**, v.129, n.5, p.2582-2589, 23 jan. 2025.

[98] GERMANO, G. et al. Nanocellulose-based random laser. **Optica.org**, p. ck_p_35, 23 jun. 2019.

[99] YAN et al. Quartzite Nanoparticles as Scatterers for Random Laser Systems. **Latin America Optics and Photonics (LAOP) Conference 2022**, v. 368, p. W1B.3–W1B.3, 1 jan. 2022.

A

Comparative tables with previously published work.

A.1

Survey of Cellulose-Based Random Lasers

Scatterer; Gain Medium	Solvent	λ_{exc} (nm); τ_{exc}	λ_{em} (nm)	$\Delta\lambda_{em}$ (nm)	E_{th}
CNC + Rh6G	EG	532; 6 ns	575	10	0.35 mJ 0.075 mJ[b]
HPC + CNC; Rh6G	Flexible thick film	532; 6 ns	575	10	0.30 mJ
AC + PEO; Rh6G	DiCM; meth	532; 6 ns	570	8	97 μJ
TW; Rh6G	—	532; 4 ns	—	5-6	0.7 mJ
HPC + AuNP; Rh6G	Water	532; 30 ps	553	—	4 mJ/cm^2
Flexible (BC) membrane + Si or AgNPs; Rh6G	Solid	532, 6 ns	565	4–10	~ 0.70–2.5 mJ[c]
Paper–Based + TiO_2; RhB	EG, solid	532, 6 ns	587–593	30	~ 0.01–0.1 mJ[d]
HPC + Kiton Red 620	Water	532, 7 ns	639	5	25 mJ, 41.5°C[e]

[a]HPC, hydroxypropyl cellulose; CNC, cellulose nanocrystaline; AC, acetil cellulose; PEO, polyethylene oxide; EG, ethylene glycol; DiCM, dichloromethane; Meth, methanol; BC, bacterial cellulose; TW, transparent wood; λ_{exc}, excitation wavelength; τ_{exc}, laser excitation pulse width; $\Delta\lambda_{em}$, FWHM; E_{th}, energy threshold.
[b]Value from log-log graph.
[c]Depending on NP concentrations.
[d]Depending on paper circuitry.
[e]Temperature depending threshold.

A.2

Survey of Random Lasers with similar oxide-based scatterers.

Scatter	Scatterer Phase/morphology	$RI_{scatter}$	Solvent	$RI_{solvent}$	Gain Medium	Concentration Scatters	Treshold Energy	FWHM
Quartzite (SiO_2)	Crystalline	1.54	EG	1.42	Rh6G 1 mM	0.1–10 mg/mL[a]	0.25 mJ 0.568 mJ/cm^2[a]	6.9 nm
SiO_2	Amorphous nanoparticles	1.47	EG	1.42	Rh6G 1 mM	0.1–10 mg/mL[a]	0.55 mJ 1.24 mJ/cm^2[a]	10.8 nm
Au@SiO_2	Cubic particles with amorphous SiO_2 Shell	–	Polystyrene	1.58	Alq3 + DCJTB	–	6.7–31.1 μJ/cm^2[a]	1.1–12.8 nm[a]
SiO_2	Amorphous spherical nanoparticle	1.47	Ethanol	1.36	Rh640 0.1 mM	10^{12}–3 ·10^{13} particles/mL[a]	20–100 mJ/cm^2[a]	7.5 nm–17.5 nm[a]
SiO_2	Amorphous Particles	1.16	Solid sample	1.16	Rh6G 6.6 mM	Doped particles	24 μJ/pulse RL Pulse FWHM 100ps	–
SiO_2	Amorphous Porous Monolith	–	Solid sample	–	Rh6G 0.1 mM	–	9.7μJ/pulse	4 nm
TiO_2	Crystalline (Anatase), Amorphous nanoparticles	2.61	PMMA	1.49	Rh6G 0.001 mM–1 mM	10^{-3} mol/L	15 mJ	9 nm
TiO_2	Crystalline Aggregates, (Needle, Rod, Spindle, Rice, Bowtie, Butterfly morphology)	2.50–2.70[a]	Adell K40 Polymer	1.50	Rh6G 5.0 mM	5–20 % volume fraction of particles[a]	–	3.5–5.5 nm[a]
TiO_2	Crystalline (rutile) spherical nanoparticle	2.61	Methanol	1.32	Rh6G 1 mM	3.54–30.0 mg/mL[a]	12.48 mJ/cm^2	5–11 nm[a]
TiO_2	Nanowire (amorphous phase)	2.61	Poly(N-vinylcarvazole)	1.68	Rh6G –	–	0.44 mJ	<0.8 nm
ZnO	Amorphous spherical nanoparticles	2.00	–	–	ZnO nanoparticle thin film	5.6 g/cm^3	763 kW/cm^2	0.3 nm
TiO_2 @ Silica	Amorphous Particles with amorphous SiO_2 Shell	–	Ethanol	1.36	Rh6G 0.1 mM	5.6 · 10^{10} particles/mL	15 mJ/cm^2	5 nm
TiO_2 @ Silica	Amorphous Particles with amorphous SiO_2 Shell	2.61	Ethanol	1.36	Rh6G 1 mM	5.6 · 10^{10} particles/mL	2.28 mJ	~5 nm
TiO_2 @ Silica	Amorphous Particles with amorphous SiO_2 Shell	2.61	Ethanol	1.36	Rh6G 0.1 mM	1.4 · 10^{12} particles/mL	1.2 mJ/cm^2	~7 nm
SiO_2	Amorphous Spherical Nanoparticle	1.47	PVA	1.48	Rh6G-doped PVA thin film	–	1.59 mJ/cm^2 -2.72 mJ/cm^2	4.7 nm
ZnO	Crystalline (Wurtzite) Nanosheet	–	EG	1.42	Rh6G 1.05 mM	0.06 M – 0.12 M	7.07 MW/cm^2 - 8.18 MW/cm^2[a]	5 nm–7 nm[a]
TiO_2	Crystalline (Rutile and Anatase), Aggregated nanospheres	–	Methanol Hexanol	1.32 1.41	RhB/Coumarin 102 10^{-2} M – 10^{-6} M	2.5 mg	–	8 nm–9 nm[a]
Ag	Triangular silver nanoparticles	0.05	PVA	1.48	Rh6G 1 mM	–	9.3 μJ/mm^2	~8 nm

[a] Depending on sample.